Characterization and Control of Two-Phase Flow in Microchannels

(PEM Fuel Cell Channels and Manifolds)

Research for Design Annual Report

July 2002 to October 2003

Jeffrey S. Allen, NCMR
Sang Young Son, NCMR
Prof. Kenneth D. Kihm, Texas A&M University

1 Executive Summary

The NASA Glenn Research Center (GRC) and the NASA Johnson Space Center (JSC) have identified water management as a critical issue for the development of PEM fuel cells for use in both high-gravity (launch and reentry accelerations) and low-gravity (near-Earth orbit) environments. This issue involves removing liquid water from a complex manifold of passages and then separating that water (liquid and vapor) from the gas flow. Currently, the methodologies for designing a PEM fuel cell with effective water management under variable gravitational conditions are not available. NASA desires to have the necessary design tools so as to develop an efficient gravitationally-insensitive PEM fuel cell.

To that end, a research program intended to provide the knowledge base necessary to design a gravitationally-insensitive PEM fuel cell was proposed. The research program was divided into three distinct phases; microchannel experiments, computational studies, and transient low-gravity experiments on the NASA Reduced Gravity Aircraft (KC-135). Because of limited funding and the uniqueness of NCMR's Research for Design (R4D) program, the originally proposed project was descoped to a pilot project limited to the microchannel experiments with some computational effort.

During the last year significant progress has been made in determining the key scaling factors for two-phase flow in capillaries which are applicable to PEM fuel cells. The choice of length scales and velocity scales in dimensionless groups used to characterize two-phase flow is critical to correctly delineating phase distribution. Traditionally, scaling for these types of flows have considered that the interaction between gas and liquid phases to be primarily inertial in nature. The role of liquid film stability where the phase interaction is a combination of viscous and capillary effects is shown to be a more appropriate scaling for low-Bond number, low-Suratman number two-phase flows. Microscopic visualization at high resolution (megapixel), low frame rate ($\leq$ 30 frames per second) and low resolution (640$\times$480), high frame rate (1000 frames per second) have been used to identify the flow regime under various gas-liquid mass ratios, channel geometries and surface energies. The effect of geometry and contact angle on the phase distribution and the pressure drop are dramatic. In addition to the microchannel experiments, three unique optical diagnostic techniques for measuring thermo-fluid transport in microchannels have been proven. These techniques were developed under contract with Texas A&M University.

During the next year of this project, the single channel experiments will be concluded and we will move to multiple parallel microchannel experiments within which the effect of density wave oscillations on phase interaction will be investigated. In addition, we will, despite limited funding, attempt to integrate the newly developed optical techniques into the microchannel experiments so as to compliment the current microscopic visualization. Finally, computational efforts will begin which will validate specific submodels against the microchannel experiment data.

Contents

2 Overview of Project

Two-phase flow plays a major role in a number of technologies critical to manned and unmanned space missions; including fuel cells, phase and particle separators, thermal management systems, and bioreators. Many of these technologies exhibit a common morphology of complex flow paths, multiple channels, and manifolds. Terrestrial applications such as MEMS scale and lab-on-chip technologies also incorporate similar complex flow paths. Of particular interest in this study is the flow of gas and water vapor through microchannel gas flow passages of proton-exchange membrane (PEM) fuel cells.

The NASA Glenn Research Center (GRC) and the NASA Johnson Space Center (JSC) have identified water management as a critical issue for the development of PEM fuel cells for use in both high-gravity (launch and reentry accelerations) and low-gravity (near-Earth orbit) environments. This issue involves removing liquid water from a complex manifold of passages and then separating that water (liquid and vapor) from the gas flow. Currently, the methodologies for designing a PEM fuel cell with effective water management under variable gravitational conditions are not available. NASA desires to have the necessary design tools so as to develop an efficient gravitationally-insensitive PEM fuel cell.

To that end, we have developed a research program intended to provide the knowledge base necessary to design a gravitationally-insensitive PEM fuel cell. This research program is divided into three distinct phases; microchannel experiments, computational studies, and transient low-gravity experiments on the NASA Reduced Gravity Aircraft (KC-135).

2.1 Introduction to PEM Fuel Cells

A PEM[1] fuel cell operates by catalytically stripping a hydrogen atom of its electrons and then passing the protons (hydrogen ions) across a polymeric membrane. The membrane acts as a barrier to the reactants. The membrane also acts as a barrier to the electrons which pass from the anode to the cathode via an external circuit from which may power some electrical device. The oxygen, the electrons, and the protons are catalytically recombined into liquid water at the cathode. Figure 1 illustrates the basic operation of a PEM fuel cell. The heart of a PEM fuel cell is the Membrane Electrode Assembly (MEA). The design of the MEA varies with manufacturer, but generally the MEA consists of a catalyst-laden gas-diffusion anode, a proton-conducting membrane, and a catalyst-laden gas-diffusion cathode. The MEA is sandwiched between to two plates which have gas flow channels machined into the faces. The gas flow channels serve as a supporting structure for the MEA, as an electrical conductivity path, and as a means to direct gas exchange with the anode and the cathode. In order for the proton transport to occur, the membrane must be hydrated. Though water is being produced, many PEM fuel cell designs use a humidified oxygen stream on the cathode side (and sometimes the hydrogen side) in order to prevent the dryout of the PEM membrane near the entrance region of the gas flow passages.

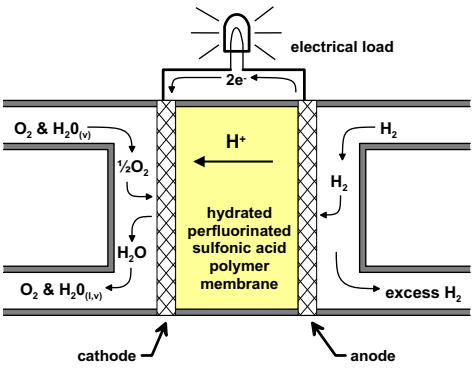

Figure 1. PEM Fuel Cell Operation

Figure 2 illustrates the decrease in cell potential as the cell current density increases. The ideal potential of the oxygen-hydrogen reaction is approximately 1.2 V when the product is liquid water. However, this potential is reduced as soon as the reaction begins to occur. Initially, there is a polarization, or over potential, due to rate limited kinetics of the half-reactions. This is known as the "activation polarization". The kinetics of the cathode, or the O_2 reduction, are 100 times slower than the H_2 oxidation at the anode. As the current density of the fuel cell increases, polarization due to ohmic resistances begins to reduce the cell potential. The ohmic resistances are due to electrical resistance in the power circuit as well as resistance to proton motion through the electrolyte. At high current densities, the production of liquid water may exceed the

[1]PEM is short for Proton Exchange Membrane or Polymer Electrolyte Membrane. Polymer Electrolyte Fuel Cell (PEFC) is also a commonly used description.

capacity of the gas streams to move the water out of the fuel cell stack. The cell is flooding either in the porous electrode or in the gas flow channels. At this condition, the cell potential drops dramatically in a condition known as concentration polarization.

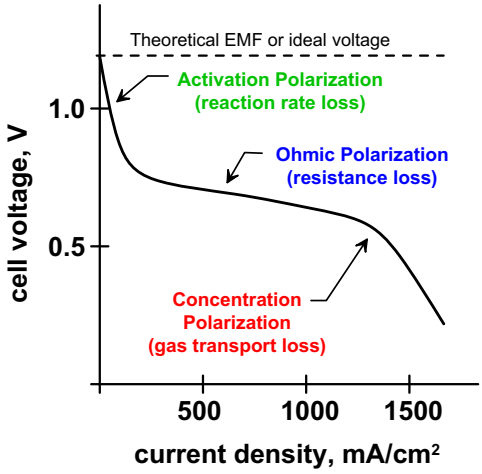

Figure 2. Fuel cell polarization curve.

The production of water at the cathode must be balanced by removal of water from the cell. As the oxygen gas stream becomes saturated, the removal of water from the gas diffusion layer via evaporation diminishes and water may accumulate in the porous cathode; thereby blocking the transport of oxygen to the membrane - a condition known as "flooding". Figure 3 illustrates how water in the cathode may affect the diffusion of oxygen to the membrane. A balance between keeping the membrane too dry and too wet must be maintained for efficient and reliable operation.

If the water accumulation becomes too great, then the gas flow channel may become completely blocked by water; a condition known as "liquid holdup" (illustrated in Figure 4). The problem of liquid holdup is particularly acute in a low-Bond number environment where capillary effects can destabilize a liquid film which may "pinch off" the flow passage with a liquid bolus.

In addition to liquid management inside the membrane channels, there is a need to understand two-phase flow behavior after exiting the cell flow channel. Several individual cells are combined in a series, or stack, in order to obtain the desired voltage so the oxygen and fuel is provided to the individual cells of the stack through a manifold. It is critical to the performance of the fuel cell stack that the flow distribution be as uniform as possible into the stack and that water is effectively removed from all cells. Efficient operation requires that the remaining oxygen and hydrogen be reused and this requires separation of the water from the two gas flow streams. Phase separation in low gravity is not intuitive. Moreover, NASA requires phase separation in both a low-gravity environment and a hyper-gravity environment.

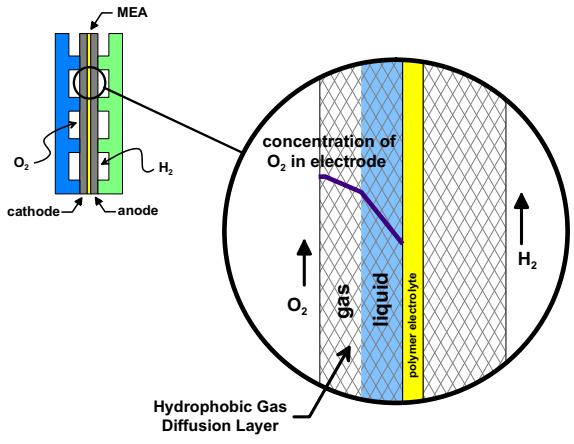

Figure 3. Water management in the cathode gas diffusion layer. Note the decrease in O_2 concentration in the liquid film occupying the porous electrode.

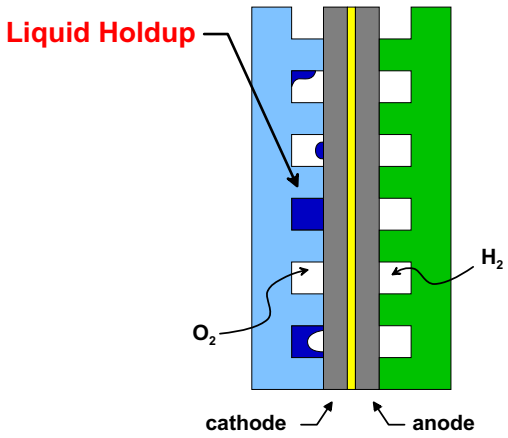

Figure 4. Cross section of PEM fuel cell element illustrating liquid blockage of gas flow channel.

2.2 Scope and Objectives of Research

The objective of providing design tools for the development of a gravitationally-independent PEM fuel cell for use by NASA can only be accomplished by understanding two-phase flow in complex passages where capillary forces are significant. Two-phase flow is dependent upon many factors including void fraction, relative velocities of each phase, geometry, fluid-fluid interface dynamics, fluid-solid interface dynamics, inertia effects, viscous effects, capillary effects, etc. The focus of the proposed study is on four of these factors which have been identified as most critical to the stability of two-phase flow and which directly impact the design of the gas flow passages and manifolds. These are **inertia effects**, **geometric effects**, **surface effects**, and **flow conditions**.

The **inertia effects** will be investigated by comparing the flow characteristics in microchannels under normal gravity, and in macrochannels in a low-gravity environment. The flow in microchannels will be viscous dominated, whereas the macrochannels flow will be affected by both viscous and inertia effects. In essence, the low-gravity environment will be used to 'switch-on' the effect of inertia on the two-phase flow. To study the **geometric effects**, the aspect ratio and length/diameter ratio of the channels (micro and macro) will be varied to match that found in typical PEM fuel cell designs. Several complex flow configurations, such as "L", "T", "Y", and manifolds will be tested. The **surface effects** on two-phase flow will be studied by investigating flow with variable surface wettability. The surface wettability determines whether or not a continuous film exists throughout the channel. Liquid film rupture may be a key factor in the onset of liquid holdup. Currently, PEM fuel cells have a "non-wetting" electrode in contact with a "wetting" gas flow passage; though anecdotal evidence suggests that the static contact angle is relatively large for both surfaces. This type of configuration is also found in other applications ranging from lab-on-chip and micro-electro-mechanical systems (MEMS) on the small scale to phase-change heat transfer systems on the large scale. Finally, the **flow conditions** will be studied by varying the flow rates and the gas-liquid fractions over the range expected in PEM fuel cells.

The scientific objectives are to gain insight and understanding of low-Bond number[2] (Bo) two-phase flow in complex passages and manifolds and to use the knowledge gained to advance PEM fuel cell technologies for space applications. Specific science objectives are:

1. Determine the nature of low-Bond number, two-phase flow in complex flow paths when inertia may be neglected;
2. Determine the effect of wetting configuration on liquid film evolution and flow rates in capillary-dominated, two-phase flow in manifolds; and
3. Develop predictive tools for liquid management and liquid-gas separation in low-gravity, two-phase systems.

The technology objectives are to provide design tools sufficient to develop a gravitationally insensitive PEM fuel cell for use in space applications.

2.3 Technical Approach

These scientific objectives will be met through two distinct experimental efforts and a complimentary computational effort. The experimental efforts are divided into microchannel experiments conducted in ground-based laboratories and macrochannel experiments conducted on the KC-135 Reduced Gravity Aircraft. Both types of experiments will investigate isothermal gas-liquid flows in low Bond number environments. The microchannel experiments will allow for long duration investigations of two-phase flow evolution. The macrochannel experiments will be strongly influenced by inertia effects and require a low-gravity environment to maintain a small Bond number. The normal gravity microchannel experiments represent one end

[2]The Bond number, $\mathrm{Bo} = \Delta\rho g r^2/\sigma$, is a ratio of gravitational effects to surface tension effects on a liquid surface; $\Delta\rho$ is the density difference across the surface, g is the gravitational acceleration, r is the characteristic length scale and σ is the surface tension. When the Bond number is small, surface tension effects dominate. A small Bo may be achieved by reducing the gravitational acceleration or by reducing the characteristic length scale as is found in capillary tubes.

of the flow regime, while the low-gravity macrochannel experiments represent the other end. Experiment parameters to be varied, in both normal and low-gravity tests, are the wetting configuration, the geometric configuration, the aspect ratio, the length/diameter ratio, and the flow rates & gas-liquid ratio.

The microchannel experimental technique (shown in Figure 5) will be to displace liquid from the flow channels using an inert gas. This will produce long gas bubbles in the liquid-filled channels. A liquid film will be deposited on the walls of the channel and the evolution of the liquid film may be observed. The liquid film may be stationary or have an imposed flow during the gas imbibition. The test section will be interchangeable and several geometric configurations will be tested; including elbows, tees, headers, and wyes. The test sections will be constructed so that the wettability of any of the four channel walls can be varied; thereby creating a closed channel where one or two walls are wet differently than the remaining walls. Liquid-gas separation using capillary effects will also be tested at both low and high gas flow rates.

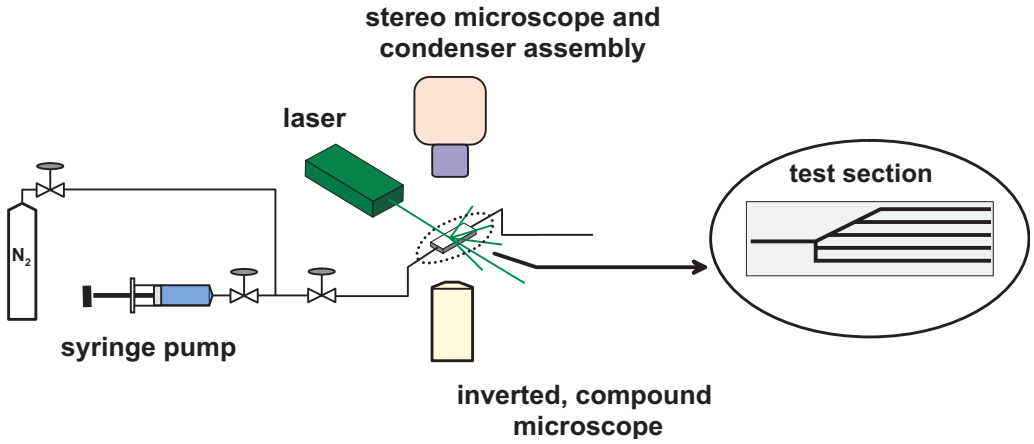

Figure 5. Setup for microchannel experiments.

The macrochannel experiments will investigate flow through three different test sections on NASA's KC-135 Reduced Gravity Aircraft. The three test sections, which correspond to the microchannel experiments, are a straight channel, a 90° bend, and a manifold. The test sections will be varied in aspect ratio and length/diameter ratio and only uniformly wetting conditions will be investigated. The straight channel and 90° bend test sections will be scaled to the microchannel experiments. The manifold test section will be scaled to the flow conditions found in manifolds which feed the humidified gas into the fuel cell flow passages. In addition, unsteady two-phase flow through various reducers, expanders and other standard fittings will be studied in order to provide designers with immediate information on two-phase flow behavior.

Insight into the complex behavior of the two phase flow inside micro-channels and manifolds can best be achieved through hand-in-hand mathematical/numerical modeling and experiments. Therefore, an integral part of this research effort will be devoted to the development of a numerical model for the process. The problem is complicated, however, because of the need to accurately track the movement of the interface between the two phases as the liquid displaces the gas/void and as the injected voids/bubble/gas displaces the liquid volume. Since the interface between the two phases undergoes severe displacement and deformation in the course of a transient simulation the most efficient way to simulate the process is to track the interface on a fixed computational grid.

2.4 Anticipated Results

At the conclusion of this research, we should have the ability to predict liquid holdup and flow bifurcation/separation in complex channels for non-inertial, low Bond number two-phase flows in a variety of wetting conditions. This information can be used to develop predictive tools for designing low-gravity two-phase technologies. Specific design tools include:

1. phase separation and mixing strategies,
2. scaling analysis for determining water removal as a function of flow rate, geometry, and gas-liquid ratio, and
3. a video library of transient two-phase flow through various geometries.

Figure 6 illustrates the relationship between the scientific objectives and the design objectives, or deliverables. These deliverables should help build a "low-gravity, two-phase flow intuition" among designers of space-based PEM fuel cells as well as other advanced space technologies.

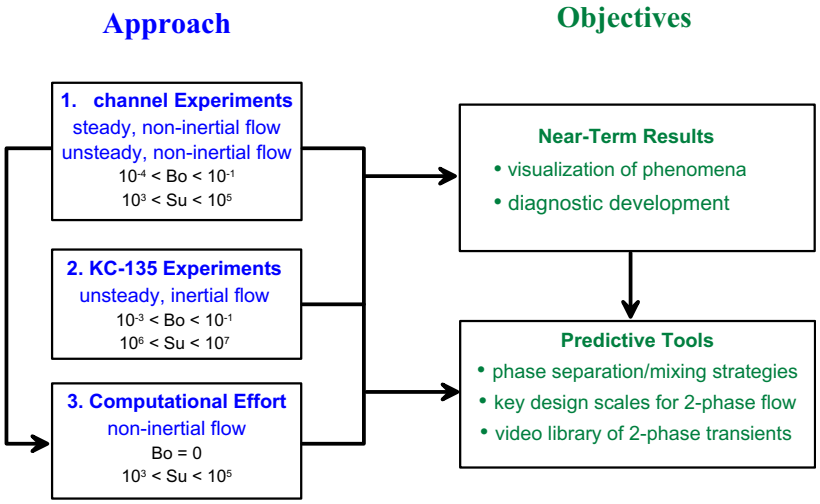

Figure 6. Relationship between research phases and the desired objectives. The Bond number, Bo, is a dimensionless relationship between gravitational and capillary forces on interface shape. The Suratman number, Su, is a dimensionless relationship between inertia, viscous, and capillary forces.

The original timeline for the proposed R4D effort is shown in Figure 7. The minimum expected time to deliver effective design tools was anticipated to be three and one-half years.

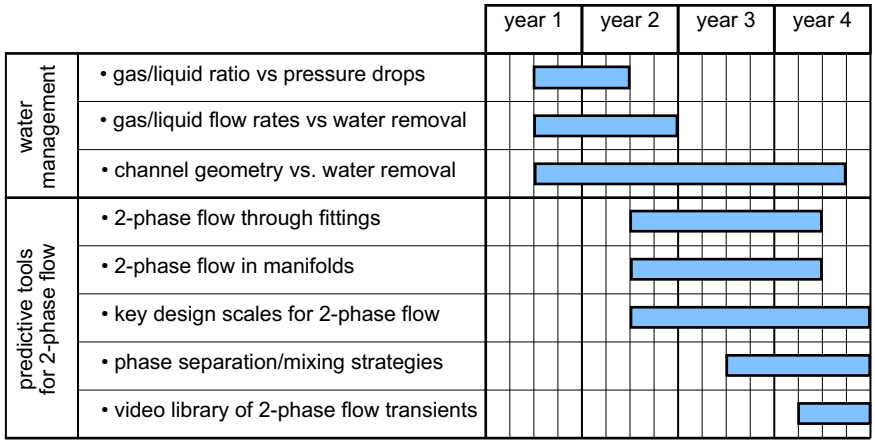

Figure 7. Original timeline for characterization and control of two-phase flow in microchannels.

2.5 Descope of Original Proposal for Pilot Project

Due to funding constraints and the uniqueness of NCMR's Research for Design (R4D) initiative, this project was begun as a "pilot project" at approximately half the proposed budget in order to establish the value and utility of the R4D concept with NASA. The original scope of the project as documented in the preceding sections was reduced to fit time constraints and budget constraints. The primary descope involves the macrochannel experiments on the KC-135. A minimum of $50,000 of additional funding per year would have been required to complete this portion of the original objectives. Other sources of funding have been sought but, to date, not secured. The rescoped objectives of the pilot project effort are to obtain the Near-Term Results as shown in Figure 6 as well as develop the key design scales for two-phase flow. Summarizing these objectives:

- **microscopic visualization of phase distribution coupled to pressure measurements**
- **development of diagnostic techniques appropriate to microfluidics**
- **determination of key design scales for low Bond number two-phase flow**

During the course of the last year, it has become apparent that the water management problems associated with PEM fuel cells is not isolated to NASA directed technology development. The water management problem within the fuel cell stack is the same for terrestrial-based fuel cells and space-based fuel cells. There is a growing interest in this research work by commercial fuel cell developers; particularly within the transportation industry. Since NASA is contracting the fuel cell development work and not doing in-house research on stack design, the true customers for this research are the commercial fuel cell developers. Therefore, the scope and direction of this research is being redefined so as to utilize the existing knowledge within the commercial fuel cell development community as well as to respond to the water management issues of most concern to the industry. The result being that two new objectives have been added:

- **interact and learn from commercial fuel cell developers concerning water management issues**
- **dissemination of results and design information generated by the R4D project to the commercial fuel cell community**

The unique NASA component for water management in PEM fuel cells may be isolated to the water-gas separation external to the fuel cell stack and a new program, distinct from this Research for Design (R4D) effort, has been established with the Fuel Cell Projects ~ Renewable Energy Systems group (org. code 5420) at the NASA Glenn Research Center. Currently, this group is funding NCMR to prepare a whitepaper on existing active and passive low-gravity phase separation technologies.

3 Microchannel Experiment Progress at NASA Glenn

The microchannel experiments investigate low-Bo and low-Su number two-phase flow. This is the most important parameter range for water management in the gas flow channels of PEM fuel cells, but it is not the appropriate parameter range for two-phase flow in the fuel cell stack manifolds. Nevertheless, significant progress toward the objective of providing design tools for water management in PEM fuel cells has been made during the last year.

The key scaling factors for two-phase flow in capillaries which are applicable to PEM fuel cells has been determined. The choice of length scales and velocity scales in dimensionless groups used to characterize two-phase flow is critical to correctly delineating phase distribution. Traditionally, scaling for these types of flows have considered that the interaction between gas and liquid phases to be primarily inertial in nature. The role of liquid film stability where the phase interaction is a combination of viscous and capillary effects is shown to be a more appropriate scaling for low-Bo, low-Su number two-phase flows. Microscopic visualization at high resolution (megapixel), low frame rate ($\leq$ 30 frames per second) and low resolution (500×500), high frame rate (1000 frames per second) have been used to identify the flow regime under various gas-liquid mass ratios, channel geometries and surface energies. The effect of geometry and contact angle on the phase distribution and the pressure drop are dramatic.

3.1 Dimensionless Numbers with Scaling Factors

The phase distribution, or flow regime, can be characterized using dimensionless parameters with flow variables including fluid density (ρ), viscosity (μ), surface tension (σ), a characteristic velocity (U), a characteristic length (L), and gravity (g). For microchannel flow, two flow regimes are generally observed; annular and plug. The annular flow regime describes a system where the liquid phase is predominantly located on the walls of the channel or tube with a gas core flow. The plug regime describes a system where the gas and liquid phases are separated into small volumes which span the characteristic length of the channel. Balancing inertial effects, gravitational acceleration and viscous effects against capillarity provides a number of relevant dimensionless parameters two-phase microchannel flow.

The Bond number, $\mathrm{Bo} = \rho g L^2/\sigma$, is a ratio of gravitational effects to surface tension effects on a liquid surface. When the Bond number is small, surface tension effects dominate. A small Bo may be achieved by reducing the gravitational acceleration or by reducing the characteristic length scale as is found in capillary tubes. We define a microchannel as having a characteristic length such that the $\mathrm{Bo} < 1$ in normal gravity.

The Bond number characterizes the relative effect of gravity and capillarity on a static system. Several additional dimensionless parameters are used to characterize dynamic interactions. For a small Bo system, the relative influence between capillarity and viscosity is best captured through the Capillary number, $\mathrm{Ca} = \mu_l U/\sigma$; where μ_l is the liquid viscosity. When the $\mathrm{Bo} \ll 1$ and $\mathrm{Ca} > 0.1$, then significant distortion of a liquid-gas surface may occur due to viscous stresses.

The Reynolds number, $\mathrm{Re} = \rho U L/\mu$, is a standard measure of the relative influence of inertia and viscous effects on flow. The characteristic length and velocity are usually chosen based upon a hydraulic diameter and a mean flow rate. However, in a microchannel system, as defined by the Bo, the hydraulic diameter and the mean flow rate do not sufficiently capture the interaction between the gas and liquid phases.

The Weber number, $\mathrm{We} = \rho U^2 L/\sigma$, is a measure of the inertial effects to capillarity. For a small Bo system, a liquid surface may break up due to inertia if the $\mathrm{We} > 1$. The proper choice of characteristic length and velocity in a micro-scale system is not the same as with macro-scale system. In particular, the hydraulic diameter and mean flow rate are usually poor choices for characteristic scales when the Bo is small.

The Suratman number, $\mathrm{Su} = \rho\sigma L/\mu^2$, is a measure of surface tension forces compared to inertia forces when the velocity scales as a balance between surface tension and viscous drag. Su is equivalent to the square of the Reynolds number divided by the Weber number. Alternatively, the Su number is the Reynolds number with the characteristic velocity equal to the capillary velocity (σ/μ) as represented in the Capillary number. The Su provides a good measure of the degree of damping in a two-phase, low Bo system.

Low-Bo, low-Su two-phase flow is in the viscous regime ($10^{-4} < \mathrm{Bo} < 10^{-1}$, $10^3 < \mathrm{Su} < 10^5$) and has been extensively studied; particularly in the areas related to oil recovery. It has long been recognized that an annular liquid film is unstable to long wavelength instabilities. [1, 8, 9, 5, 13, 3, 6, 7] For annular films without an imposed axial flow and no surface shear, it has been observed that the liquid will accumulate into lobes and, if the volume of liquid is sufficient, into lenticular lenses, or liquid plugs, which "pinch-off" the core flow. The formation of a lenticular lens from the liquid in the annular film is also referred to as "snap-off" or "liquid hold-up". Whether the adjacent lobes/lenses are connected to one another by a liquid film depends upon the static contact angle between the liquid and the tube and upon van der Waals forces [17]. Everett and Haynes [5], in a study of condensation in capillary tubes, examined the surface energy of constant curvature interfaces. They report that as the liquid film forms a lobe of critical volume, the surface energy can be minimized by reorienting the liquid lobe into a lenticular lens. Though the quasi-equilibrium analysis does not give information on the rate of reorientation, the energy jump can be significant which indicates a rapid process. Thus, the stability of the liquid film can significantly influence the inertia of the system through the morphological change from thin film to plug.

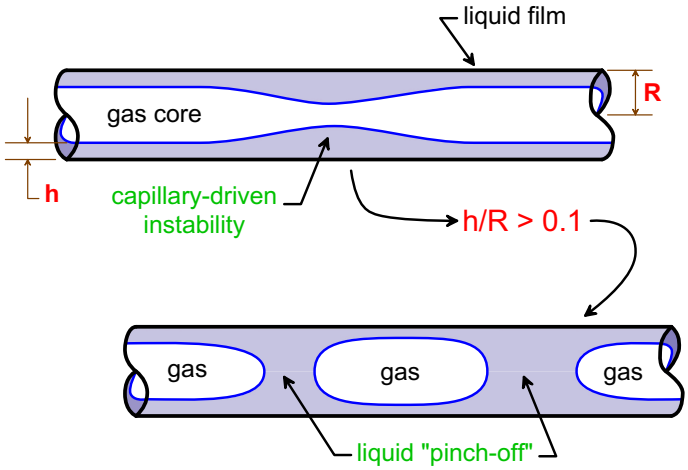

Figure 8. Illustration of capillary-driven instability of liquid film which can result in "liquid holdup".

Figure 8 illustrates the lobe formation and eventual pinchoff of the gas flow by the liquid film. The pinchoff results from a capillary-driven instability; commonly referred to as a Rayleigh instability. Goren [8], using a linear stability analysis, determined the wavelength which gives rise to the fastest growth of a perturbation for various film thicknesses and Suratman numbers. Hammond [9] extended Goren's linear analysis and examined the nonlinear growth rates using the thin film approximation $h/R \ll 1$, where h is the film thickness and R is the tube radius. Hammond determined that the characteristic time for interface flow on an annular film is $t_\lambda \sim \mu R^4/\sigma h^3$ and the disturbance wavelength resulting in the fastest growth was found to be $2^{3/2}\pi R$. Typically, t_λ is on the order of a millisecond for gas-liquid flow in a microchannel. Gauglitz and Radke [6] modified the nonlinear analysis of Hammond by using the small slope assumption in place of the thin film assumption. The critical film thickness to lens formation was found to be $0.12R$ and the experimentally determined critical film thickness was found to be $0.09R$. Aul and Olbricht [4] studied lobe formation in flowing liquid films at low Reynolds numbers and found that the wavelength of the most unstable disturbance is independent of the Reynolds number for $\mathrm{Re} < 100$. This indicates that inertia of the gas core is not affecting the stability of the liquid film. Subsequently, the traditional two-phase flow scaling will not capture the transition from annular flow regime to plug flow regime.

These low-Bo studies have shown both experimentally and theoretically, that two-phase flow in straight channels can rapidly undergo liquid-gas configurations changes; slug-bubbly transitions in high-Su flow and liquid lobe/lens formation (pinch-off) in low-Su flow. The liquid-gas configuration changes have been extensively studied for low-Su flows and, thus, provide a solid starting point for examining high-Su flows which have not been studied from a fundamental fluid physics viewpoint.

The effect of geometric configuration on low-Bo two-phase has been studied to a greater degree for low-Su flows (viscous) than for high-Su flows (inertial). In low-Bo, low-Su (viscous) flows, film breakup occurs as a bubble passes through an orifice or constriction in liquid filled capillary tubes; a process often referred to as 'pinch-off'. In the studies of Gauglitz and Radke [7] and Arriola et al. [3] the location of the pinch-off was found to be a function of the geometry and the flow conditions in both cylindrical and square capillaries. Ransohoff et al. [16] considered the effect of liquid flow in corners on the pinch-off of a gas bubble in constricted capillaries with a square cross section. They report that snap-off can only occur when the tube constriction is of a critical diameter which is in directly opposed to the study by Aul and Olbricht [4] where snap-off was experimentally observed in square capillaries without any constriction.

The majority of the effort in the low-Bo, high-Su (inertial) two-phase flow research has been in determining flow transition in straight, circular tubes. Very little research has been conducted in non-circular channels and even less in manifold type of flow paths. In a preliminary analytical study, Young, Best, and Kurwitz [18] modeled microgravity, two-phase flow in manifolds by equilibrating pressure drops across each leg of the flow path. They used an empirical model for the gas-liquid separation at a channel junction which was formulated for intersections of cylindrical tubes. The physics of gas-liquid separation was not addressed and it is not known how the flow will behave for non-circular channels. Allen and Hallinan [2] found that a condensed liquid film in a smooth tubing bend would 'pinch-off' the vapor core. The bend geometry provided an impetus for a capillary induced instability even though the two-phase flow was in the high-Su regime.

In these fundamental studies, the importance of the dynamics and stability of liquid films on the behavior of two-phase flow is established over and over again. It is critical to include the physics of the liquid films in scale modeling in order to properly characterize two-phase flow in microchannels.

3.2 Unique Test Section Design

Figure 9 illustrates the experimental setup for the measurements of the pressure drop and the microscale flow visualization. The system consists of the visualization setup, the water and the nitrogen gas supplying lines, and the differential pressure measurement setup. The mass flow rate of the single phase flows (water and nitrogen) is inversely calculated using the laminar flow theory with the measured pressure drops through the single round tube (ID = 330 μm, L = 12.5 cm), which is implemented in-between the supplying line. A high spatial resolution scientific CCD camera (1200 $\times$ 1000 pixels, 12 bit depth, and 22 fps) captures the flow images. In addition, an high speed CCD camera (500 $\times$ 500 pixels, 8 bit, and up to 60,000 fps) was used for certain test conditions. The visualization data are synchronized with the measured pressure drops of two single phase flows and one two-phase flow.

The two phases (water and nitrogen) meet at the entrance region and naturally generate converging-nozzle-type entrance flow as illustrated in Figure 10 and imaged in Figure 11. The uniquely designed and controlled

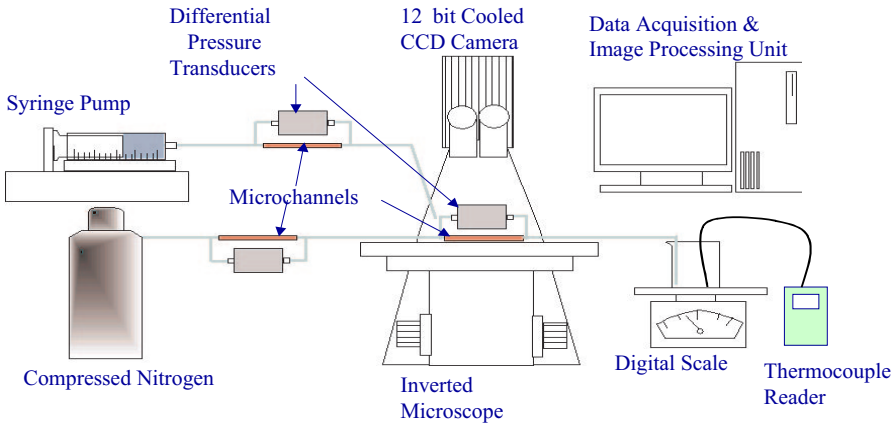

Figure 9. Schematic of actual microchannel experiment setup.

entrance flow gives the several advantages in two-phase microchannel flow study. The two-phase flow regimes including slug, slug-to-annular (transient), and annular flow can be synthetically generated by manipulating the supplying single-phase fluid pressure. The naturally generated converging-nozzle-type flow also minimizes the entrance effect on the flow in the downstream of the microchannel.

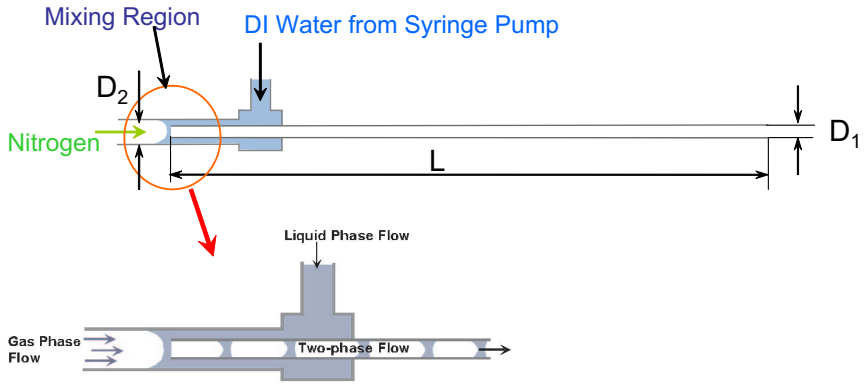

Figure 10. Two-phase mixing region of microchannel experiments.

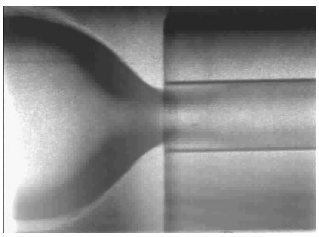

Figure 11. Converging-nozzle-type entrance flow defined by liquid meniscus.

3.3 Methodology for analyzing experiment data

The pressure drop data are analyzed and processed using the analysis flow chart (Figure 12). In order to precisely determine the mass flow rate of nitrogen and water, two differential pressure transducers measure the pressure drop of each single phase flow through a microchannel, which has the same dimension with the microchannel for the two-phase flow measurement. Simultaneously with the single phase pressure measurements, another differential pressure transducer measures two-phase flow pressure drop. The flow regime of the two-phase flow is confirmed with the visualization of the flow patterns, recorded by the high resolution CCD camera. As described before, the conventional laminar theory using the friction factor (f = 64 for single phase flow in the round tube) convert the pressure drop data to mass flow rate. It is well known that the conventional laminar theory of single phase flow in the duct is valid in the order of 100 μm hydraulic diameter duct flow [14]. The characteristic parameters including characteristic length and velocity are decided depending on the confirmed flow regimes. For the plug or plug-to-annular flow, the characteristic length and velocity are the tube hydraulic diameter and velocity regarding two-phase volumetric flow rate, respectively. However, for the annular flow, the characteristic length is the film thickness, which are estimated using the void fraction of two-phase flow and the characteristic velocity is the liquid film or gas core flow velocities considering the estimated liquid film thickness and the mass flow rate of each phase. Finally, the dimensionless group is constructed for the specific experimental conditions and the confirmed flow regime.

3.4 Microchannel Experiment Results

The microchannel experiments were conducted under a variety of gas and liquid flow rates. In addition, two different geometries and two different surface conditions were tested. The two geometries were square and circular cross-sections. The two surface conditions were coated and uncoated. The uncoated condition is the clean glass surface which has a contact angle less than 20°. The coated condition is created by coating the glass surface with a fluorochemical polymer (FC-723, 3M Corp.) which results in a contact angle of approximately 70°. The change in contact angle results in dramatic differences in the flow conditions and pressure profile in the square channel. This is discussed in greater detail in §3.4.4. The results of the microchannel experiments are divided into phenomena visualization, power spectrum analysis of back-light

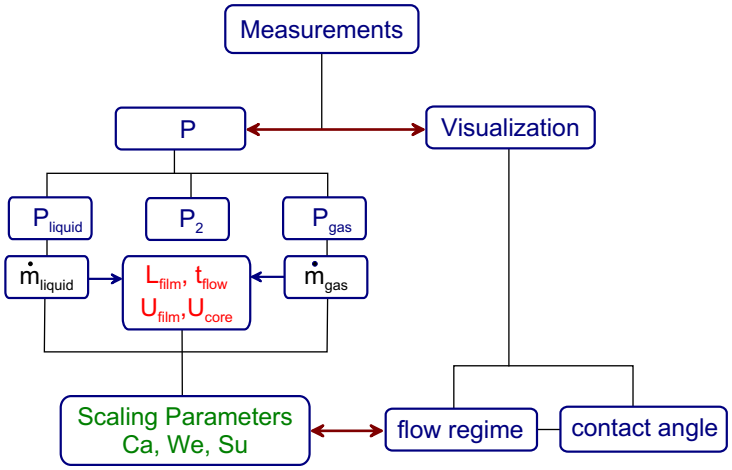

Figure 12. Microchannel experiment data analysis.

intensity variations derived from visualization, effect of choice of length and velocity scales on delineating the flow phenomena, and the effect of contact angle and geometry on the flow condition and pressure drop of two-phase flow through a microchannel.

3.4.1 Flow Regime Visualization

The phase distribution (flow regime) of gas-liquid flows in low-Bo circular channels tends to be either Plug Flow or Core-Annular Flow. Both of these conditions are illustrated in Figure 13 for N_2 and water flowing in a 350 μm diameter glass capillary.

Plug Flow, shown in the right-most column of sequential images, is characterized by a volume of liquid which completely fills the cross-section of the channel for some limited length. The liquid "plugs" the channel relative to the flow of gas. In Figure 13, the annular liquid film between liquid plugs exhibits the capillary instability as discussed in §3.1. The interfacial shear on the surface of the annular liquid film is negligible due to the restriction of gas flow imposed by the liquid plugs.

Core-Annular Flow, shown in the left column of sequential images, is characterized by a liquid film on the interior wall of the channel with a core of gas flowing through the center portion of the channel. For this condition, the shear on the surface of the annular liquid film may be severe. The sequence of images in Figure 13 illustrates the formation of a liquid unduloid due to a combination of capillary and shear effects. The unduloid traverses the capillary at a velocity approximately two orders of magnitude slower than the mean gas velocity.

3.4.2 Power Spectrum Analysis Experiments

A power spectrum analysis was conducted on the transient back-scattered light intensity signal of two-phase flow in a microchannel. The test fluids were nitrogen and 100 cSt silicone oil and the two flow regimes analyzed were annular and slug flow. A high resolution camera (1200 x 1000 pixels) captured the scattered light intensity at 30 frames per second. The light intensity varies with the thickness of the liquid film and, thus, can be used to detect wave propagation on the annular liquid film. The formation of a liquid slug from the annular film may also be detected.

Figure 14 shows a sequence of images which illustrate the back-scattered intensity shift as a wave propagates along the annular liquid film. Figure 15 illustrates the power spectral of two-phase flow in a microchannel as a function of time. The power spectral density does not show a clear dependency of scattered light intensity on frequency in the time domain. The highest correlation is about 1.8 Hz. The correlation covers too large of a frequency range to determine wave speeds.

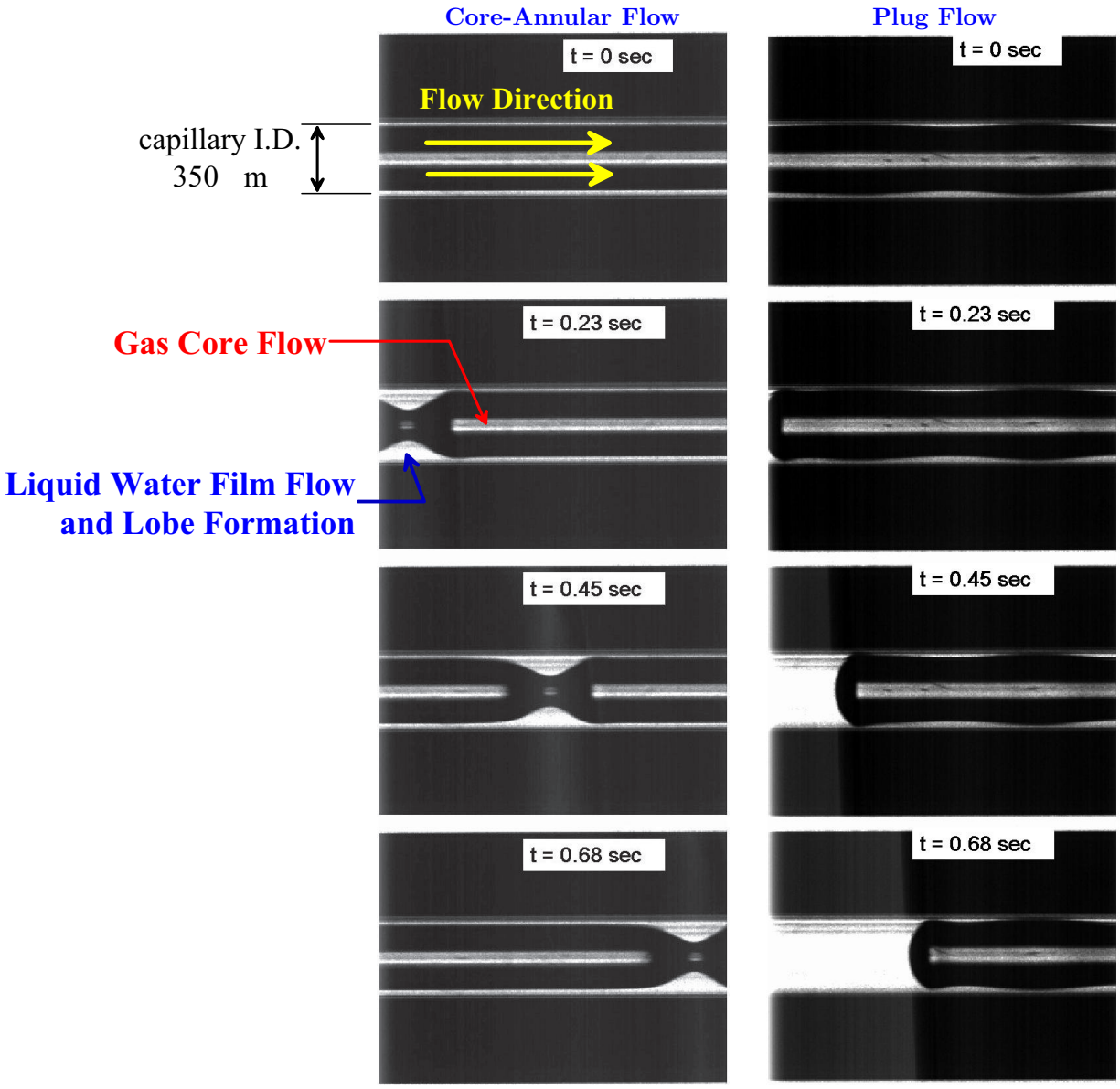

Figure 13. Illustration of Plug Flow and Core-Annular Flow in a 350 μm with N_2 and liquid water.

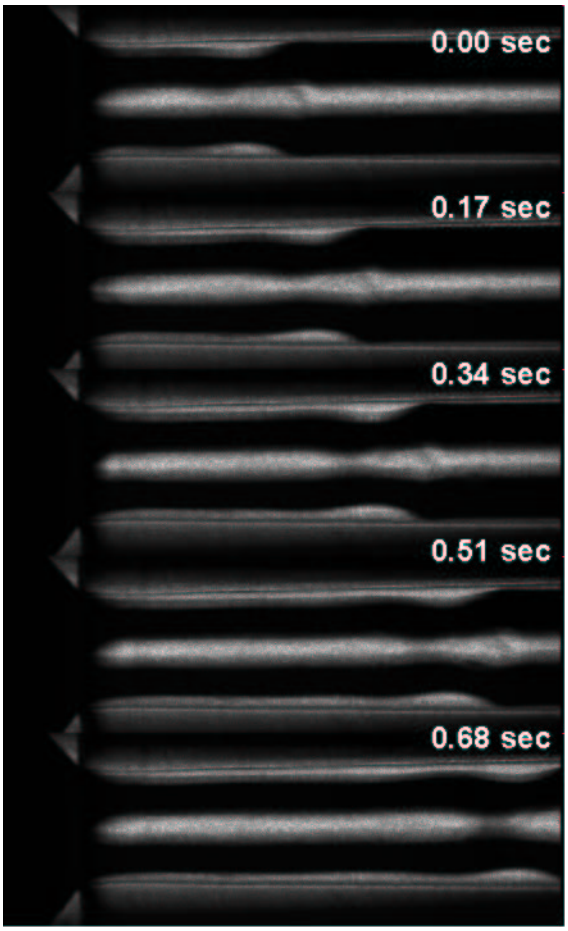

Figure 14. Sequence of images illustrating variation in back-scatter intensity as a wave propagates along the annular liquid film in a microchannel.

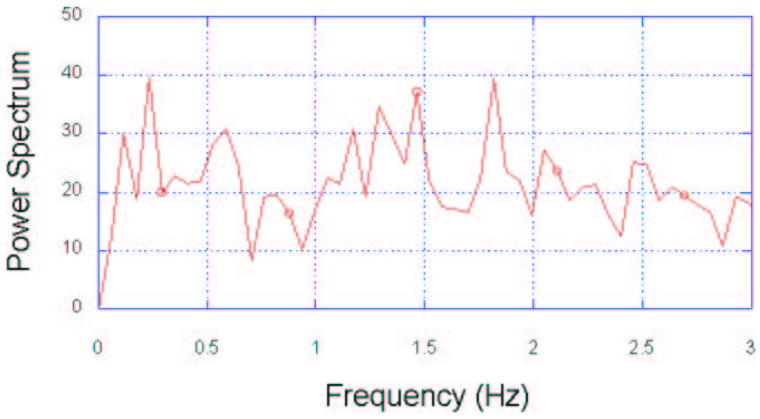

Figure 15. Power spectrum of light intensity reflected from the liquid film of an annular flow; $\mathrm{Re}_{gas}/\mathrm{Re}_{liq} = 432$, N_2 and 100 cSt silicon oil.

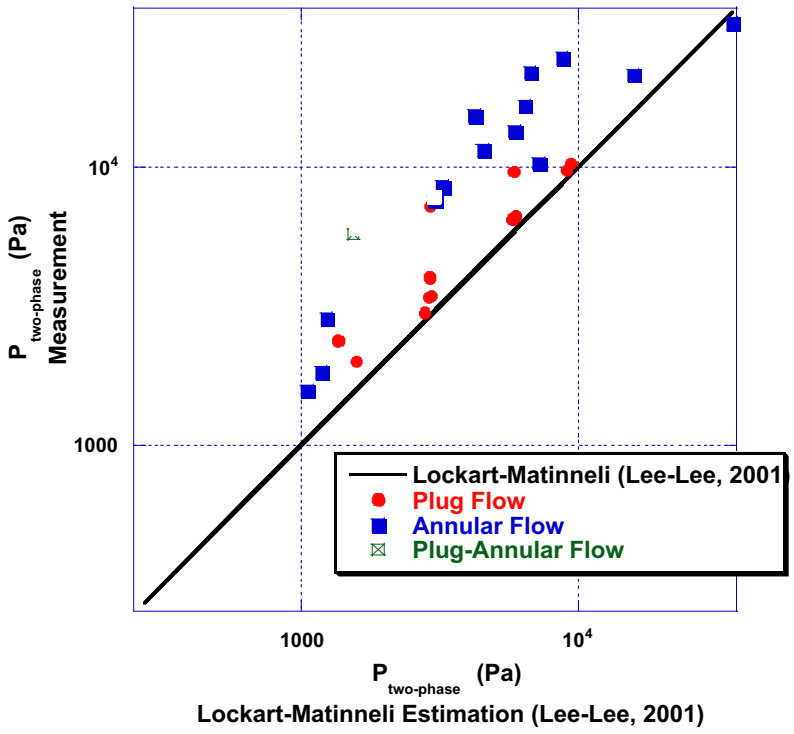

Figure 16. Comparison of the measured two-phase flow pressure drop with the estimation by the modified conventional Lockart-Martinelli correlation.

3.4.3 Proper Scaling of Two-Phase Flow in Capillaries

Lockart-Martinelli (L-M) type correlation has been developed in order to predict the two-phase flow pressure drop since the 1940's. Lee and Lee [12] modified the classical L-M correlation using their two-phase pressure drop data in a micro square channel. Lee-Lee's L-M correlation emphasized an increased surface tension effect on the pressure drop in the microchannel. The experimental data of the current study is compared with the estimated values from Lee-Lee's correlation in Figure 16. For the plug flow, L-M correlation reasonably predicted the two-phase Pressure drop within -30%. In other flow regimes (Annular and Plug-to-Annular flow), the measured data differed by more than +50% from the L-M correlation predicted values. The deviation difference in the different flow regime may come from the surface tension effect on the flow. The Annular or Plug-to-Annular flow has less significant surface energy effect than the Plug flow because of the capillary pressure which may be applied in the plug flow.

Figure 17 compares Suratman number variations in the different length scales. The left plot and the right plot in Figure 17 use the microchannel hydraulic diameter and the liquid film thickness, respectfully, as the characteristic length for the Suratman number. There is no clear delineation of flow regime with changing Su number when the characteristic dimension is the hydraulic diameter (left plot). In contrast, using the liquid film thickness as the characteristic length provides for clear separation of the flow regimes with the Su number. Figure 17 illustrates the importance of the dynamics of the thin liquid film in a low Bond number two-phase flow.

In a similar fashion, Figure 18 illustrates the effective delineation of flow regime with Capillary number (Ca) when the thin film dynamics are incorporated. The left plot in Figure 18 scales the Ca number using the

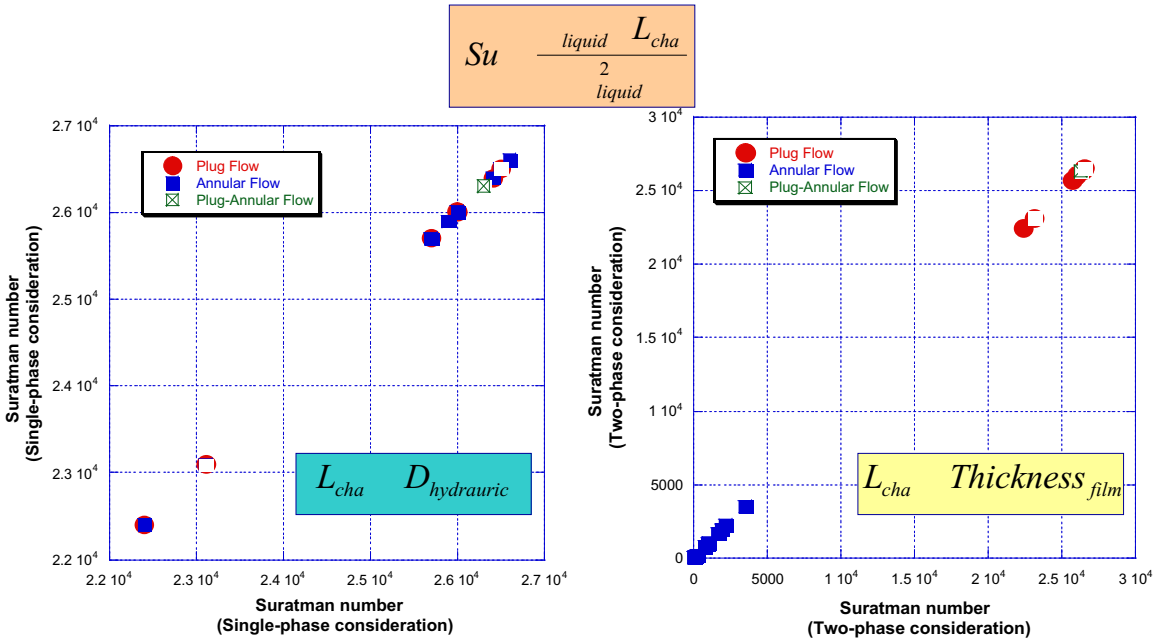

Figure 17. Effect of choice for characteristic length scale on the delineation of two-phase flow regime using the Suratman number. The left plot scales the characteristic length with the hydraulic diameter of a 330 μm diameter round capillary. The right plot scales the characteristic length based on the thickness of the liquid film.

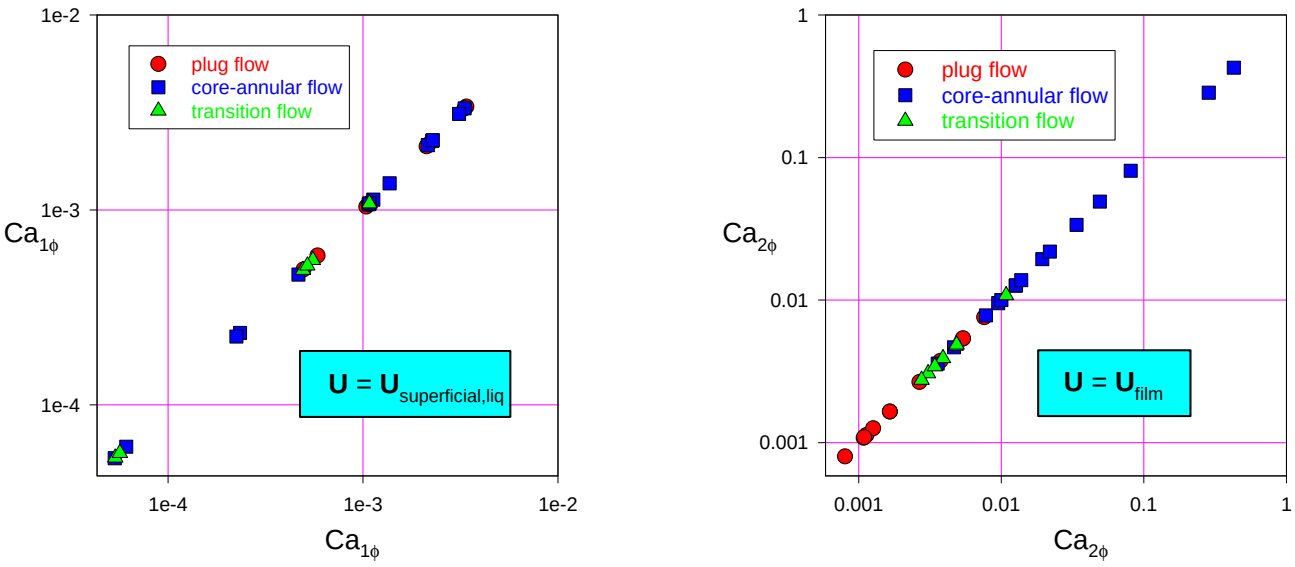

Figure 18. Effect of choice of characteristic velocity scale on the delineation of two-phase flow regime using the Capillary number. The left plot scales the characteristic velocity as the superficial velocity of two-phase flow in a 330 μm round tube. The right plot scales the characteristic velocity with the liquid film velocity.

traditional superficial velocity. No separation of flow regime with Ca is seen. However, using the velocity of the liquid film for the Ca number provides clear delineation of flow regime. Again, illustrating the importance of thin film dynamics on the behavior of low Bo number two-phase flow.

Two-phase flow patterns in microchannels are experimentally characterized using the single- and two-phase pressure drops and flow visualization. The measured two-phase pressure drop shows more than 30% deviation from the estimated values using the modified conventional Lockhart-Martinelli correlation which is primarily based upon an inertial exchange between the gas and liquid phases. Using the hydraulic diameter as a length scale in annular flow for the dimensionless numbers does not accurately identify the flow regime transition. At microfluidic scales, the behavior of liquid films plays a critical role in flow regime transition. *Incorporation of thin film dynamics is essential to correctly scaling the physical phenomena associated with gas-liquid flows having a strong capillary component.*

3.4.4 Effect of Geometry and Contact Angle on Pressure Drop

The current set of microchannel experiments included variations in (i) gas and liquid flow rates, (ii) geometry, or channel cross section, and (iii) surface energy, or static contact angle (θ). Two cross sections were tested; 330 μm circular and 500 μm square. Two contact angles were tested; less than 20° for uncoated glass capillaries and $\sim$ 70° for coated glass capillaries. The coating is a fluorochemical polymer (FC-723, 3M Corp.) which forms a monolayer of a teflon-like polymer on the interior surface of the glass capillary.

Figure 19 illustrates the pressure drop through the two-phase test section. The test section for this data is an uncoated ($\theta < 20°$) 12.7 cm long, 330 μm diameter circular glass capillary. The liquid phase is water and the gas phase is nitrogen. The striking feature of Figure 19 is the disruption of flow and the subsequent linear increase in pressure differential across the test section. The two inset images show the flow morphology (flow is left to right) for the two types of pressure drop behavior. Although the two-phase flow is categorized as plug flow for both morphologies, the behavior of the flow is strikingly different.

The lower inset image is of plug flow in a classic Taylor bubble arrangement where a continuous liquid film connects the liquid plugs. The mean ΔP is approximately 6000 Pa and the volumetric flow rate is very high. The image shown of the Taylor bubble flow could only be captured using a high speed video camera at 1000 Hz with 128 μsec exposure. The upper inset image shows that the annular liquid film has ruptured and drained into the liquid plugs. The pressure drop across the test section increases linearly with time to nearly an order of magnitude greater than the mean ΔP of the Taylor bubble flow. The increase in pressure is the result of contact line motion which is absent for the Taylor bubble flow. The peak value of pressure drop ($\approx$ 32,500 Pa for Figure 19) can be correlated to the number of contact lines, or liquid plugs, within the test section. The transition between Taylor bubble flow over a continuous liquid film and flow over a dry surface is incredibly fast. The mechanism for the film rupture, which appears to occur between all of the liquid plugs simultaneously, is still in question. As the isolated liquid plugs accelerate, the advancing and receding contact angles of the slug begin to diverge from the static contact angle. The difference between the advancing and receding contact angles may be seen in the upper inset image. The pressure drop continues to increase linearly as the liquid slugs accelerate until the Capillary number is high enough that the receding contact angle approaches 180° and a sufficient liquid film is deposited such that each trailing plug of liquid becomes connected to the plug in front. At this point, the pressure drop suddenly and dramatically decreases and the flow reverts back to the Taylor bubble morphology. The process from isolated plug flow (dry wall between plugs) to Taylor bubble plug flow (wet wall between plugs) is cyclic as shown in Figure 20.

The upper trace in Figure 20 is the volumetric flow rate of the liquid phase as measured by the differential pressure transducer on the liquid line (see Figure 9 for details). The lower trace is the pressure differential across the two-phase test section. The cyclic nature of the liquid film rupture and liquid plug acceleration is apparent. The volumetric flow rate of the liquid phase is generally inversely proportional to the pressure drop across the two-phase test section. There is a time lag in the volumetric flow rate to that of the two-phase pressure drop for sudden changes in pressure. The time lag is associated with the compression and decompression of the gas phase between the liquid plugs.

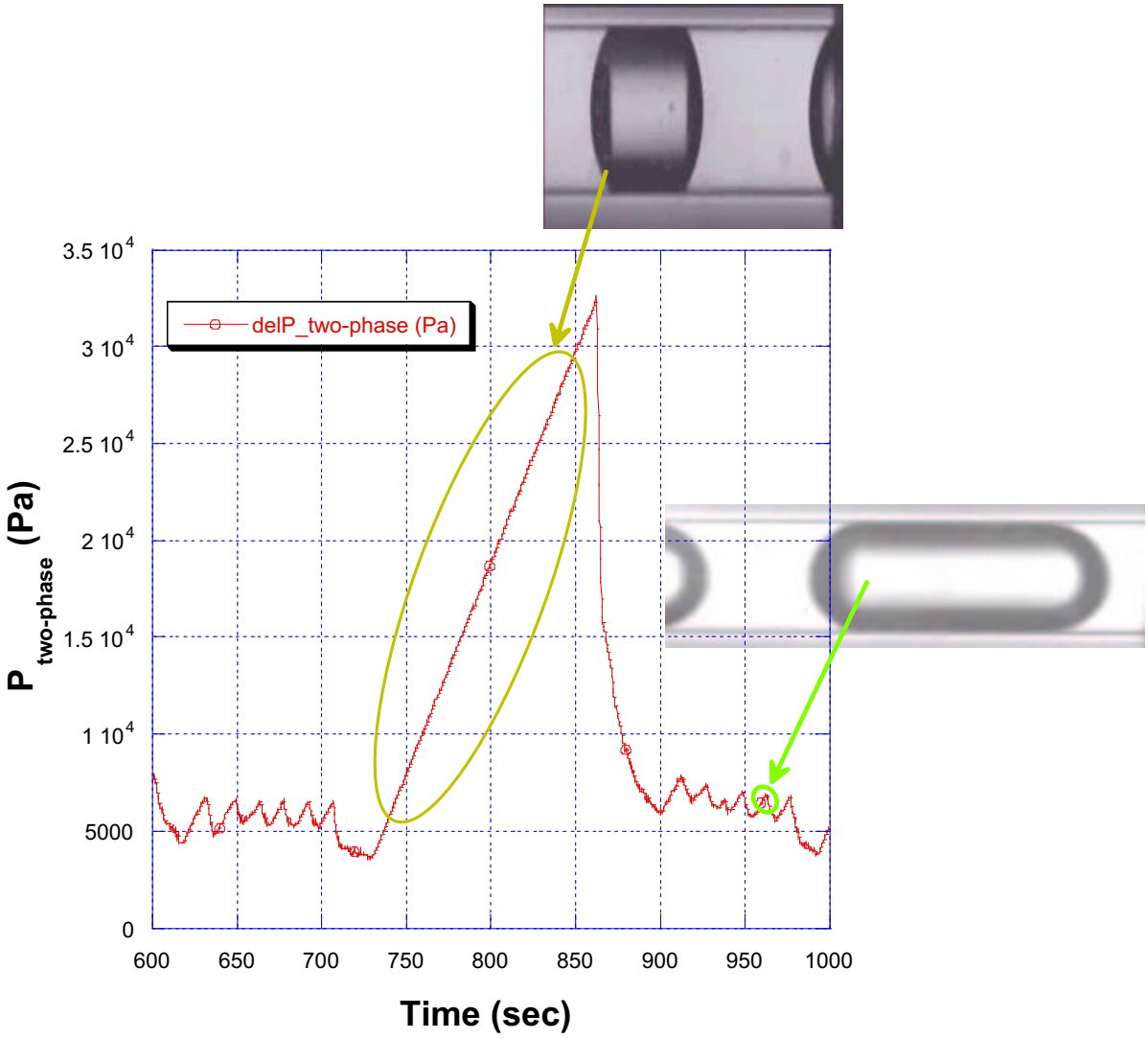

Figure 19. Variations in test section pressure drop with change in morphology of plug flow in an uncoated ($\theta < 20°$) 12.7 cm long, 330 μm diameter circular channel using water and N_2 as the test fluids. The rupture of the annular liquid film connecting the liquid plugs results in a dramatic increase in pressure drop due to the energy dissipation associated with the moving contact lines.

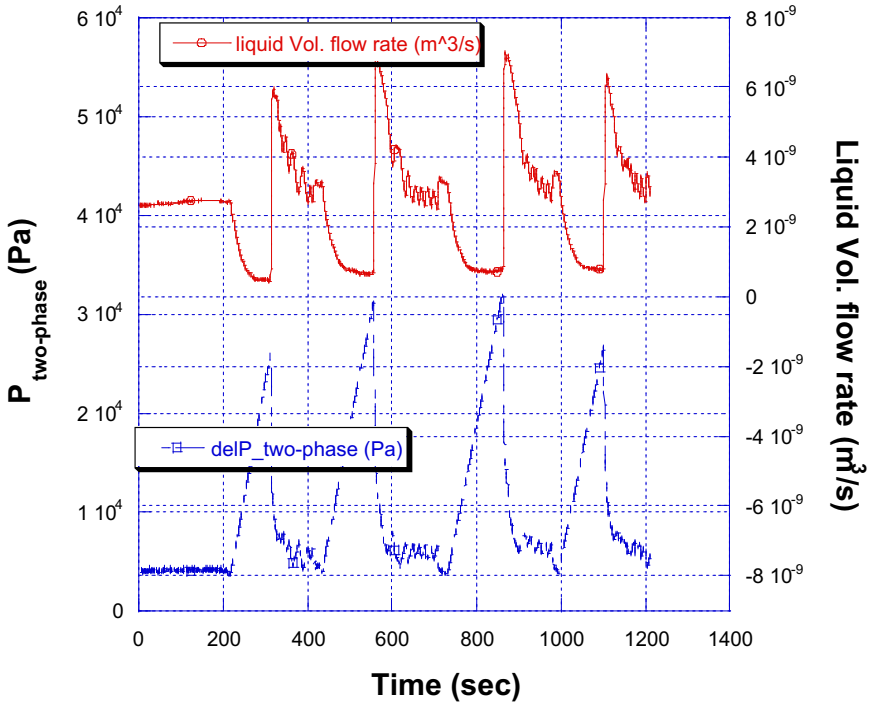

Figure 20. Volumetric flow rate of liquid phase and two-phase pressure drop of plug flow in a 12.7 cm long, 330 μm diameter uncoated ($\theta < 20°$) circular glass capillary. Liquid phase is water and gas phase is nitrogen.

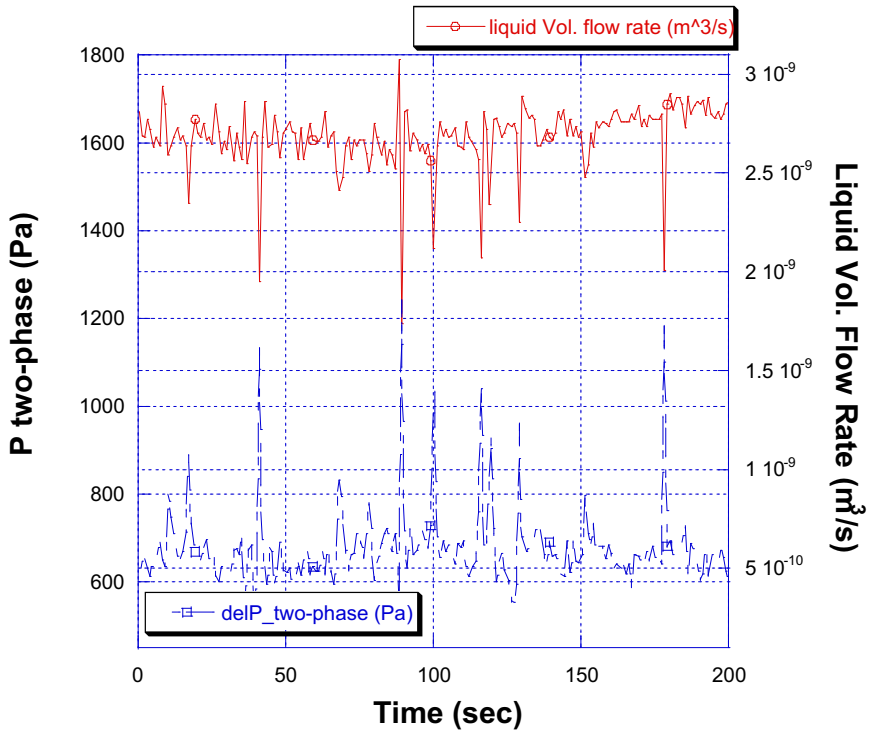

Figure 21. Volumetric flow rate of liquid phase and two-phase pressure drop of plug flow in a 10.1 cm long, 500 μm ($\theta < 20°$) uncoated square glass capillary. Liquid phase is water and gas phase is nitrogen.

The peak pressure drop during the isolated plug flow may be correlated to the number of plugs in the test section which, in turn, is related to the number of advancing and receding contact lines. The moving contact lines dissipate much more energy than does the inertia and viscous dissipation of the liquid plug motion thus the tremendous increase in pressure drop.

Figure 21 illustrates the liquid flow rate and two-phase pressure drop for a 10.1 cm long, 500 μm square uncoated ($\theta < 20°$) glass microchannel under similar conditions to Figure 20. However, the mean two-phase pressure drop is much lower than for the round channel tests. Although pressure drop spikes are present in Figure 21, the magnitude of these spikes is relatively small. Also, the volumetric flow rate of the liquid phase is inversely proportional to the pressure drop for all time indicating that there is no morphology change of the plug flow as was evident in the round channel tests. In other words, there is no film rupture and no contact line motion for the plug flow in the uncoated square channel tests. This lack of film rupture is likely due to the propensity of the liquid to occupy the corners of the square microchannel due to the static contact angle, θ, being less than the Concus-Finn condition.

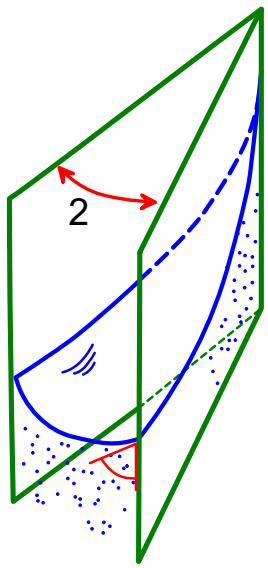

Figure 22. Wicking of liquid in a corner due to capillarity.

The Concus-Finn condition sets the criteria for when liquid will wick into or out of a corner via capillary pressure. Figure 22 illustrates the corner wicking with the pertinent parameters. Equation 1 defines the Concus-Finn condition where 2α is the corner angle and θ_{CF} is the critical contact angle. For reference, a square cross-section has an $\alpha = 45°$.

$$\theta_{CF} \equiv \frac{\pi}{2} - \alpha \tag{1}$$

$$\theta < \theta_{CF} \quad \Rightarrow \quad \text{corner wicking}$$

$$\theta > \theta_{CF} \quad \Rightarrow \quad \text{corner dewetting}$$

When θ is less than the Concus-Finn condition ($\theta < \pi/2 - \alpha$), then the liquid phase may wick into a corner under the action of capillary forces. When θ is greater than the Concus-Finn condition ($\theta > \pi/2 - \alpha$), then the liquid phase will wick out of the corner via capillarity. For the square microchannels, $\theta_{CF} = 45°$. Thus, for the uncoated test sections where $\theta < 20° < \theta_{CF}$, the Concus-Finn criteria is met and liquid flows into the corners of the microchannel via capillary pressure. The coated test sections have a contact angle of $\theta \sim 70° > \theta_{CF}$ and the liquid flows out of the corners via capillary pressure. Both wicking into and out of the corners for the respective coated and uncoated channels have been observed during the square microchannel experiments.

The effect of contact angle on the two-phase pressure drop in a microchannel is shown in Figure 23. Four traces of pressure differential versus time are shown. The flow conditions for each of the four tests are given in Table 1. For the uncoated square test sections ($\theta < 20°$, tests 724-E4 & 708-E3), the two-phase pressure drop for plug flow condition is slightly higher than for the annular flow condition even though the liquid flow rates are the comparable. Although there is a slight increase in the two-phase pressure drop for test 708-E3 versus that of 724-E4, there is no signature in the pressure measurement of test 708-E3 which indicates that plugs of liquid are present. In fact, the plug flow condition was not observed until a high speed video camera was coupled to the microscope. The images taken at 1000 frames per second at 128 μsecond exposure clearly show plugs of liquid moving at extremely high velocities through the microchannel. The slight increase in pressure drop between these two flow conditions is due to the acceleration of the liquid slugs to the velocity of the gas phase. For the coated square test sections, however, the pressure signature between plug flow and core-annular flow is significant. Test number 725-E4 has a low mean differential pressure trace which is relatively smooth and is indicative of core-annular flow. In contrast, the plug flow condition for the coated square test section (test no. 725-E6) has a wildly fluctuating pressure differential which is associated with the formation and breakup of liquid plugs and the subsequent motion of multiple contact angles.

From the microchannel experiments conducted during the last year, there is evidence that the phase distribution, or flow regime, is a strong function of not only the liquid and vapor flow rates, but also the geometry (square/circular) and the contact angle. *The static contact angle has a significant effect on the behavior of two-phase flow in low-Bond number channels with corners. Currently, the contact angle is not considered during the design of flow fields for PEM fuel cells.*

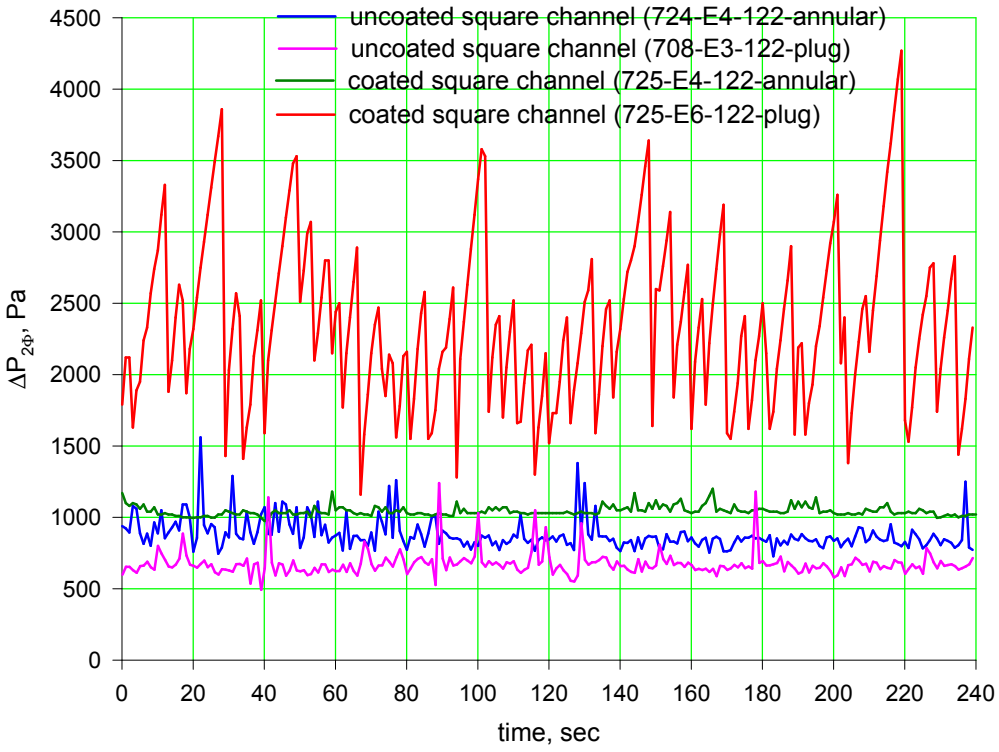

Figure 23. Pressure drop through a 10.1 cm long, 500 μm square microchannel for core-annular and plug flow regimes with varying contact angle. The uncoated tests had a contact angle of less than 20° which is less than the Concus-Finn Condition; therefore, liquid wicks into the corners of the channel. The coated tests had a contact angle of approximately 70° which is greater than the Concus-Finn Condition; therefore, liquid wicks out of the corners.

Table 1. Test conditions for the pressure differential time traces shown in Figure 23.

			flow rate [10^9 m^3/sec]		2ϕ
test no.	θ	flow condition	water	nitrogen	$\mathrm{Re}_g/\mathrm{Re}_l$
724-E4	$< 20°$	Core-Annular	3.0	0.0208	16.4
708-E3	$< 20°$	Plug-Transition	2.69	0.697	0.0653
725-E4	$\sim 70°$	Core-Annular	2.99	0.0155	12.3
725-E6	$\sim 70°$	Plug	5.84	9.37	0.0593

3.5 Non-Intrusive Pressure Measurement for Microfluidics

A backscattering interferometer based upon the work of Professor Darryl Bornhop is being developed and tested at NCMR/NASA Glenn for potential use in making non-intrusive pressure measurements of single-phase flow in microchannels. Figure 24 illustrates the technique and typical fringe profile. A continuous wave laser (HeNe) with a beam diameter greater than that of the channel width is reflected off of the channel and onto a CCD array. The difference in the path lengths of the front and rear reflections is dependent upon the index of refraction of the liquid. The result is a interferometric fringe pattern which changes shape or "shifts" with temperature and pressure.

The intensity peak defined by a slice of a single fringe is scaled using a bi-cell technique so as to detect morphological changes in the intensity pattern. The bi-cell ratio is repeated for each intensity peak in the image and then each ratio is normalized to the respective peak of a fringe pattern generated under no flow. Figure 24 illustrates the results of a relatively high flow condition of water in a 500 μm square glass capillary when the flow rate is cycled on and off. The normalized bi-cell response of a single peak clearly indicates that the technique is detecting flow. Subsequent tests have proven that the technique also detects variation in flows; i.e. a flow rate detector. Future work will endeavor to quantify the signal so that this technique may be used to measure flow and/or pressure.

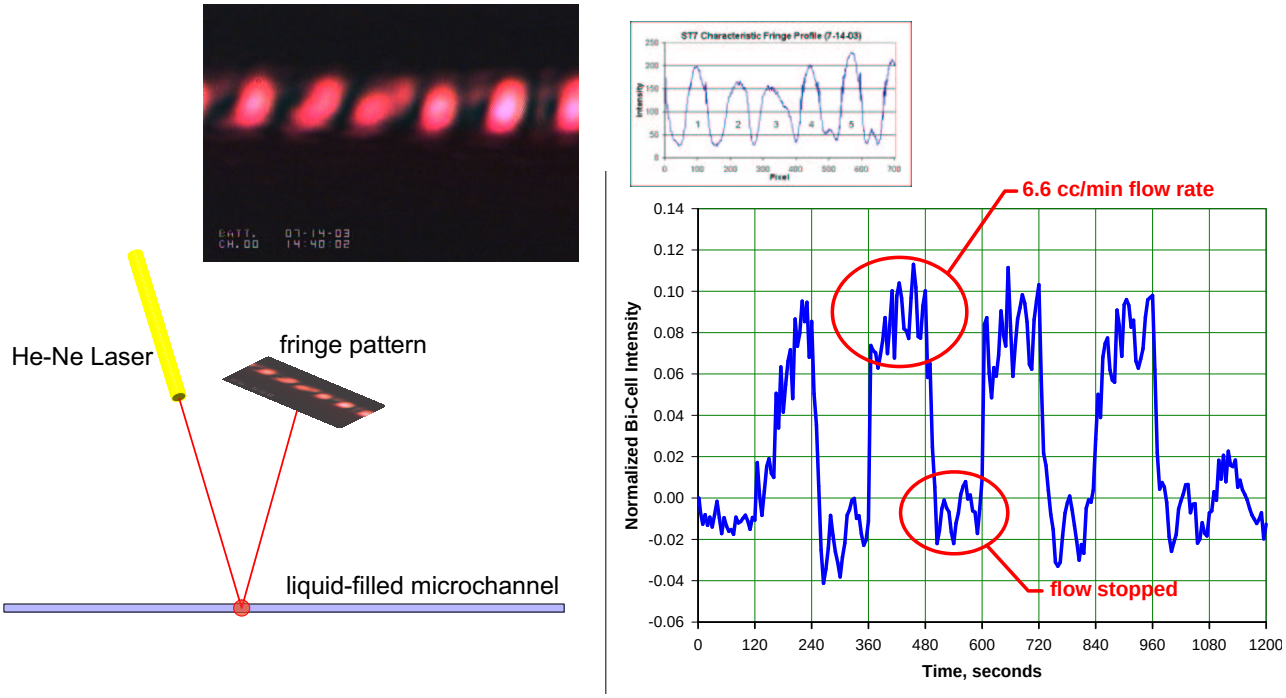

Figure 24. Backscattering interferometer based on the work by Prof. Darryl Bornhop being evaluated for non-intrusive pressure measurments in microchannels. The experimental setup uses a 500 μm square channel filled with water; flow rate cycled between 6.2 and 0 cc/min on approximately 2 minute intervals.

4 Development of Microchannel Diagnostics at Texas A&M

This section describes the development and testing of unique optical diagnostic techniques for use in microfluidic experimentation. These techniques have been developed at Texas A&M University by Professor Kenneth Kihm and his graduate students under the Research for Design contract through TEES. Unfortunately, the cancellation of the TEES contract has resulted in a cessation of this work for NCMR.

4.1 Microscale Two-Color Laser Induced Fluorescence

Two-Color Laser Induced Fluorescence (LIF) has been modified in order to make field measurements of temperature in microchannels. Currently, the technique is applicable only for single-phase flows. This technique fills a gap in microfluidic experiments where temperature measurements have been limited to measurements of the substrate from which the channels are fabricated. The substrate temperature measurements are typically an integrated over an area many times larger than the dimensions of the channel and, therefore, are a gross measure of fluid temperature. The 2-Color LIF technique provides actual fluid temperatures at resolutions much finer than the dimensions of the channel. The technique is described in the journal article by Kim et al. [11] which is included as an attachment in §8.1.

The microscale 2-color LIF technique was to be further developed by Professor Kihm so that field measurements of liquid film temperatures in microchannels could be obtained. The cancellation of the TEES contract has resulted in cessation of this development for NCMR.

4.2 Optical Sectioning in Microchannels via Confocal Microscopy

Microscopic visualization of the transport phenomena associated with gas-liquid flow in a microchannel presents significant challenges due to the lens-effect resulting from the curvature of the gas-liquid interface translating through the microchannel. A novel method utilizing a state-of-the-art high-speed Confocal Laser Scanning Microscope (CLSM) has been shown to successfully map the detailed flow field around the bubble as well as provide optically-sectioned images of the interface shape. Thus, both the internal liquid flow and the gas-liquid interface shape are simultaneously captured in a microchannel. The technique is described in the conference proceeding paper by Park et al. [15] which is included as an attachment in §8.2.

Experiments have been conducted to investigate the effect of channel geometry (three different microchannels with square cross-sections, 1.0-mm, 500-μm and 100-μm), and flow conditions (Capillary numbers ranging from 0 to 0.23) on the transition in bubble shape. These experiments show a morphological change in the shape of the gas volume occurs at a Capillary number of Ca $\simeq$ 0.1.

4.3 μ-PIV using Confocal Laser Scanning Microscopy (CLSM)

The CLSM technique described above for optically-sectioning two-phase microchannel flow was modified in order to conduct μ-PIV measurements. A systematic comparison of -PIV using Confocal Laser Scanning Microscopy (CLSM) with a regular epi-fluorescent μ-PIV, under identical flow conditions and identical supplementary optical conditions, such as image magnification, field illumination, and fluorescence filtering was carried out. Detailed flow measurements were conducted for two basic flows: (1) micro-Poiseuille flows in capillary pores of 100-μm and 500 μm diameters, and (2) rotating micro-Couette flows confined in a 180-μm layer. The μ-PIV CLSM technique provides a significant improvement over epi-fluorescent μ-PIV in accuracy and resolution of flow fields in microchannels. The technique is described in the R4D Bi-Annual Report submitted to NCMR by Professor Kihm [10] which is included as an attachment in §8.3.

5 Citations

References

[1] M. Abbasov, Z. M. Zorin, and N. V. Churaev. Displacement of immiscible liquids in fine quartz capillaries. displacement under the influence of a pressure differential. *Kolloidnyi Zh.*, 51(4):634–639, 1989.

[2] Jeffrey S. Allen and K. P. Hallinan. Liquid blockage of vapor transport lines in low bond number systems due to capillary-driven flows in condensed annular films. *International Journal of Heat and Mass Transfer*, 44: 3931–3940, 2001.

[3] A. Arriola, G. P. Willhite, and D. W. Green. Trapping of oil drops in a noncircular pore throat and mobilization upon contact with a surfactant. *Society of Petroleum Engineers J.*, pages 99–114, 1983.

[4] R. W. Aul and W. L. Olbricht. Stability of a thin annular film in pressure-driven, low-reynolds-number flow through a capillary. *J. Fluid Mechanics*, 215:585–599, 1990.

[5] D. H. Everett and J. M. Haynes. Model studies of capillary condensation; 1. cylindrical pore model with zero contact angle. *J. Colloid and Interface Science*, 38(1):125–137, 1972.

[6] P. A. Gauglitz and C. J. Radke. An extended evolution equation for liquid film breakup in cylindrical capillaries. *Chemical Engineering Science*, 43(7):1457–1465, 1988.

[7] P.A. Gauglitz and C.J. Radke. The dynamics of liquid film breakup in constricted cylindrical capillaries. *Journal of Colloid and Interface Science*, 134(1):14–40, 1990.

[8] S. L. Goren. The instability of an annular thread of fluid. *J. Fluid Mechanics*, 12:309–319, 1962.

[9] P. S. Hammond. Nonlinear adjustment of a thin annular film of viscous fluid surrounding a thread of another within a circular cylindrical pipe. *J. Fluid Mechanics*, 137:363–384, 1983.

[10] K. D. Kihm. Bi-annual report for characterization and control of two-phase flow in a microchannel. Technical report, Texas A&M University, July 3, 2003 2003.

[11] H. J. Kim, K. D. Kihm, and Jeffrey S. Allen. Examination of ratiometric laser induced fluorescence thermometry for microscale spatial measurement resolution. *International Journal of Heat and Mass Transfer*, 46, 2003.

[12] H. J. Lee and S. Y. Lee. Pressure drop correlations for two-phase flow with horizontal rectangular channels with small heights. *International Journal of Multiphase Flow*, 27:783–796, 2001.

[13] L. A. Newhouse and C. Pozrikidis. The capillary instability of annular layers and liquid threads. *J. Fluid Mechanics*, 242:193–209, 1992.

[14] H. J. Park, S. Y. Son, M. C. Choi, G. Lim, I. Song, and J. J. Pak. Temperature-dependent property effects on laminar flow characteristics in a rectangular microchannel (mems-23865). In *ASME International Mechanical Engineering Conference and Exhibition (IMECE)*, New York, NY, 2001. ASME.

[15] J. S. Park, K. D. Kihm, and Jeffrey S. Allen. Three-dimensional microfluidic measurements using optical sectioning by confocal microscsopy - flow around a bubble trapped in a microchannel. In *ASME International Mechanical Engineering Congress and Exposition (IMECE)*, New Orleans, Louisiana, 2002. IMECE2002-32790.

[16] T. C. Ransohoff, P. A. Gauglitz, and C. J. Radke. Snap-off of gas bubbles in smoothly constricted noncircular capillaries. *AIChE J.*, 33(5):753–765, 1987.

[17] Mark M. Weislogel and John B. McQuillen. Hydrodyamic dryout in two-phase flows: Observations of low bond number systems. In *1998 Space Technology and Applications International Forum (STAIF-98)*, volume AIP Conference Proceedings 420, pages 413–421, Alburqurque, New Mexico, 1998.

[18] Young, F. Best, and Kurwitz. Modeling of two-phase flow in manifolds under microgravity conditions. In *SpaceTechnology and Applications International Forum (STAIF99)*, Albuqurque, New Mexico, 1999. APS.

6 Current Status of Project

During the last year significant progress has been made in determining the key scaling factors for two-phase flow in capillaries which are applicable to PEM fuel cells. Primarily, we have demonstrated the importance of thin liquid film dynamics on the phase distribution (flow regime) and pressure drop. Currently, the design of fuel cell flow fields, analytically or computationally, do not take into account the stability of liquid films in the microchannels. The effect of geometry and contact angle on the phase distribution and the pressure drop have also been demonstrated to be dramatic. In particular, the Concus-Finn condition in non-circular geometries is critical to the behavior of the two-phase flow in low Bond number channels. The community of commercial fuel cell developers has recognized the importance of this work; evident in the number of invited lectures we have been requested to give as well as the continued contact by fuel cell companies(GM, Ballard, Plug Power, Hydrogenics, Nissan).

In addition to the microchannel experiments, three unique optical diagnostic techniques for measuring thermo-fluid transport in microchannels have been proven. These techniques, developed under contract with Texas A&M University, when implemented in microfluidic experiments will provide information necessary to understand the physics of the process; as opposed to phenomenological observation.

6.1 Near-Term Plans

The near-term plans for this project are focused on the next phase of microchannel experiments and submodel validation for computational codes. In particular, the objectives for the next year are:

- the single channel experiments will be concluded and the results compiled for publishing in a peer reviewed archival journal; the emphasis of the publication will be on the effect of contact angle and geometry on the phase distribution and pressure drop.
- a photogallery presentation for the Heat Transfer Division of ASME will be prepared. The photogallery will illuminate the relationship between phase distribution and static contact angle in non-circular geometries.
- we will transition from single microchannel experiments to multiple parallel microchannel experiments within which the effect of density wave oscillations on phase interaction will be investigated. The PDMS Microfabrication Lab recently established in building 5, room CW5B will be used to fabricate the microchannels.
- despite limited funding, we will attempt to integrate the unique optical techniques developed by Professor Kihm into the microchannel experiments so as to compliment the current microscopic visualization. The data provided from use of these novel diagnostic techniques will also assist in the validation of computational models which then may be used for design of fuel cell components.
- computational efforts will begin which will validate specific submodels against the microchannel experiment data. In particular, the phase morphology transitions, i.e. liquid holdup, will be computationally modeled.
- begin formalizing design criteria for the fuel cell flow fields to mitigate the effect of liquid holdup and cell flooding. This design tool will be based on the experiment data gathered from the microchannel experiments. The forum for publishing these guidelines has not been determined yet.

6.2 Concerns

The funding for the next year of this project is insufficient to continue TEES contract which has resulted in the early termination of the work at Texas A&M by Professor Kihm. The termination of this contract will impact our ability to transfer the diagnostic techniques developed at Texas A&M to NCMR and NASA Glenn. These techniques have been developed for use in experiments investigating water management in

fuel cells, but the value of these techniques extends far beyond this project into areas of biological and microsystem research which NCMR and NASA Glenn have been emphasizing as new thrust areas. We will continue to look for additional sources of funding through collaborative research projects with industry and through proposal solicitations, but the next seven months are critical to the completion of this work.

7 Cummulative R4D Related Publications/Presentations/Reports

1. R4D Proposal, "Characterization and Control of Two-Phase Flow in Microchannels", April, 2000.
2. R4D Annual Report, April, 2001
3. R4D Progress Review, July, 2001
4. "Quarterly Report (09/01/01 - 11/15/01) Characterization and Control of Two-Phase Flow in a Microchannel", submitted by Professor K. D. Kihm, Texas A&M University.
5. "Gas/Vapor Bubble Mobility in Liquid-Filled Capillary Tubes and Microchannels", J. S. Allen, invited lecture presented at the LabAutomation 2002 Conference, Palm Springs, CA, January 26-31, 2002.
6. "Quarterly Report (11/16/01 - 02/28/02) Characterization and Control of Two-Phase Flow in a Microchannel", submitted by Professor K. D. Kihm, Texas A&M University.
7. "Quarterly Report (03/01/02 - 05/31/02) Characterization and Control of Two-Phase Flow in a Microchannel", submittted by Professor K. D. Kihm, Texas A&M University.
8. R4D Annual Report - August 2002
9. "Drowning in a Teaspoon of Water – The Effect of Two-Phase Capillary Flow on the Operation of PEM Fuel Cells on Earth and in Space", J. S. Allen, presented July 26, 2002 at the NASA Faculty Fellowship Program seminar series.
10. "Capillary Phenomena in Low Temperature Fuel Cells on Earth and in Space", J. S. Allen, invited lecture, Michigan Technological University Graduate Student Seminar Series, October 24, 2002.
11. "Three-Dimensional Microfluidic Measurements Using Optical Sectioning By Confocal Microscopy - Flow Around a Bubble Trapped in a Micro-Channel", J. S. Park, K. D. Kihm, and J. S.Allen, 2002 ASME International Mechanical Engineering Conference and Exhibition, paper no. IMECE 2002-32790, New York, NY, November 17–22, 2002.
12. "Low Bond Number Two-Phase Flow Regime Transition from Slug to Annular Wavy Flow in a Microchannel", S.Y. Son, J. S. Allen, and K. D. Kihm, presented at the 2002 ASME International Mechanical Engineering Conference and Exhibition, New York, NY, November 17–22, 2002.
13. "Capillary Phenomena in PEM Fuel Cells", J. S. Allen, S.Y. Son, and M. Kassemi, presented at the General Motors Global Alternative Propulsion Center, Honeoye Falls, NY, December 13, 2002.
14. "Capillary Phenomena in Low Temperature Fuel Cells on Earth and in Space", J. S. Allen, invited lecture, Case Western Reserve University, Mechanical Engineering Seminar Series, February 28, 2003.
15. "Capillary-Driven Flow in Liquid Filaments Connecting Orthogonal Channels", J. S. Allen and S.Y. Son, invited lecture, Computational Fuel Cell Dynamics Workshop, Banff International Research Station, Banff, Canada, April 19–25, 2003.
16. "Observation of Low Bond Number Two-Phase Flow Regime Transition From Slug to Annular Wavy Flow in a Microchannel", S.Y. Son and J. S. Allen, paper no. ICMM2003-1057, First International Conference on Microchannels and Minichannels, April 24-25, 2003, Rochester, New York.
17. "Low Bond Number Two-phase Flow Regime Transition in a Microchannel", S.Y. Son and J. S. Allen, presented at the First International Conference on Microchannels and Minichannels, April 24–25, 2003, Rochester, New York.
18. "Water Management in PEM Fuel Cells", J. S. Allen, invited lecture, Mercer University, Physics Department Seminar Series, April 28, 2003.

19. "Using Lab-On-A-Chip to Model Capillary-Driven Flow in Complex, Manifolding Passages of PEM Fuel Cells", J. S. Allen, invited lecture at the NASA Intra-Agency Workshop, June 26-27, 2003, NASA Marshall Space Flight Center, Huntsville, Alabama.

20. "Bi-Annual Report (1/1/2003 - 6/30/2003) - Characterization and Control of Two-Phase Flow in a Microchannel", submitted by Professor Kihm on July 3, 2003.

21. "The Challenge of Using a Microfluidics Test Bed for Microgravity Technology Development of Fuel Cells and Life Support Systems for NASA", J. S. Allen, invited panelist, Panel Session on Challenges on Microscale Studies and Visualization, 2003 ASME Summer Heat Transfer Conference, July 21, 2003.

22. "Capillary Phenomena in Fuel Cells", J. S. Allen and S.Y. Son, 2003 Gordon Conference on Fuel Cells, July 21 - August 1, 2003, Roger Williams University, Bristol, Rhode Island. *This is listed here to indicate a transfer of information generated by the R4D research to the fuel cell community.*

23. "Examination of ratiometric laser induced fluorescence thermometry for microscale spatial measurement resolution", H. J. Kim, K. D. Kihm, J. S. Allen, *Int. J. Heat Mass Trans.*, **46**, pp. 3967-3974, 2003.

24. "Optically-Sectioned Micro PIV Measurements Using CLSM", J. S. Park, C. K. Choi, K. D. Kihm, and J. S. Allen, *J. Heat Transfer Photogallery*, **125**, p. 542.

25. "Low Bond Number Two-Phase Flow Regime Transition From Slug to Annular Wavy Flow in a Microchannel', S.Y. Son and J. S. Allen, *J. Heat Transfer Photogallery*, **125**, p. 544.

26. "Scale Modeling of Two-Phase Flow in Microchannels", J. S. Allen and S.Y. Son, Fourth International Symposium on Scale Modeling (ISSM-IV), September 17-19, 2003, Cleveland, Ohio.

27. "Capillary-Driven Flow in Liquid Filaments Connecting Orthogonal Channels", J. S. Allen, invited speaker at The 2003 Colloquium Series, October 23, 2003, School of Aeronautics and Astronautics, Purdue University, West Lafayette, Indiana.

8 Attachments

8.1 Microscale Two-Color Laser Induced Fluorescence (LIF)

Examination of ratiometric laser induced fluorescence thermometry for microscale spatial measurement resolution

H.J. Kim[a], K.D. Kihm[b], J.S. Allen[c]

International Journal of Heat and Mass Transfer **46** (2003) 3967–3974

[a] Division of Mechanical and Industrial Engineering, Ajou University, Suwon 442-749, South Korea
[b] Department of Mechanical Engineering, Texas A&M University, College Station, TX 77843-3123, USA
[c] The National Center for Microgravity Research, NASA Glenn Research Center, Cleveland, OH 44135, USA

Abstract

Ratiometric laser induced fluorescence (LIF) thermometry technique has been quantitatively examined for its capability for a microscale feld-of-view. The goal of the study is to quantitatively examine the measurement accuracy of the ratiometric LIF technique at sub-millimeter and micron scales for its potential use as a microscale temperature mapping tool. Measurements have been made for the steady temperature fields established by thermal buoyancy inside 1-mm wide closed test cell with low Grashof-Prandtl numbers ($86 < \mathrm{Gr}_w\mathrm{Pr} < 301$), and the detailed measured data have been compared with the well-known predictions. The smallest measurement resolution could be achieved being equivalent to the CCD pixel size of 4.7 μm in the present experiment, but with large data uncertainties. The measurement uncertainties show persistent improvement to better than 1 °C when measurement resolution is equivalent to 76 μm.

Available online at www.sciencedirect.com
SCIENCE DIRECT®
PERGAMON
International Journal of Heat and Mass Transfer 46 (2003) 3967–3974
International Journal of HEAT and MASS TRANSFER
www.elsevier.com/locate/ijhmt

Examination of ratiometric laser induced fluorescence thermometry for microscale spatial measurement resolution

H.J. Kim [a], K.D. Kihm [b,*], J.S. Allen [c]

[a] Division of Mechanical and Industrial Engineering, Ajou University, Suwon 442-749, South Korea
[b] Department of Mechanical Engineering, Texas A&M University, College Station, TX 77843-3123, USA
[c] The National Center for Microgravity Research, NASA Glenn Research Center, Cleveland, OH 44135, USA

Received 22 November 2002; received in revised form 2 May 2003

Abstract

Ratiometric laser induced fluorescence (LIF) thermometry technique has been quantitatively examined for its capability for a microscale field-of-view. The goal of the study is to quantitatively examine the measurement accuracy of the ratiometric LIF technique at sub-millimeter and micron scales for its potential use as a microscale temperature mapping tool. Measurements have been made for the steady temperature fields established by thermal buoyancy inside 1-mm wide closed test cell with low Grashof–Prandtl numbers ($86 < Gr_wPr < 301$), and the detailed measured data have been compared with the well-known predictions. The smallest measurement resolution could be achieved being equivalent to the CCD pixel size of 4.7 μm in the present experiment, but with large data uncertainties. The measurement uncertainties show persistent improvement to better than ±1 °C when measurement resolution is equivalent to 76 μm.

1. Introduction

Among the available means of temperature measurement probes, there is no question regarding the extensiveness and rigorousness of thermocouple (TC) probes for a wide range of heat transfer applications. A carefully calibrated TC probe is capable of measuring temperatures with better than ±0.1 K precision [1]. Two primary limitations of TC probes, however, are their relatively large spatial resolution, on the order of a few hundred microns in the conventional sense, and their physical intrusiveness in the flow. These limitations diminish the possibility of using TC probes for microscale heat transfer applications. In addition, their point measurement nature makes full-field temperature mapping very cumbersome as a large number of probes must be placed and monitored simultaneously.

Thermochromic liquid crystal (TLC) probes [2,3] are based on the temperature dependence of their optical properties in a predictable and repeatable manner. When TLC is illuminated, TLC selectively reflects light at a visible wavelength characterized by the local temperature. This relationship of color to temperature has allowed researchers to quantitatively map temperature distribution [4,5]. A difficulty in using TLC is that one has to calibrate each point of test field to compensate for the influence of the illuminating light variation [6]. The color bias occurring from the wall reflection and scattering is another obstacle in applying the TLC technique to full-field mapping. The relatively larger sizes of microencapsulated TLC beads, typically on the order of 10 μm or larger, are considered too large for microscale measurement resolution.

The laser induced fluorescence (LIF) technique [7,8] uses fluorescence dye molecules as seeding particles and the use of temperature sensitive fluorescent dyes showed LIF as a feasible temperature mapping technique [9–11]. The fluorescence intensity is proportional to the illuminating light intensity, dye concentration and optical

* Corresponding author. Tel.: +1-979-845-2143; fax: +1-979-862-2418.
E-mail address: ken-kihm@tamu.edu (K.D. Kihm).

0017-9310/03/$ - see front matter © 2003 Elsevier Ltd. All rights reserved.
doi:10.1016/S0017-9310(03)00243-6

constant of the dye called quantum efficiency [12]. Therefore, if the illumination light is perfectly uniform and the dye concentration remains constant, the fluorescence intensity may be considered, in principle, to depend only on temperature. However, in practice, it is very difficult to ensure a homogeneous incident light intensity distribution, if not impossible, since the laser sheet intensity progressively decreases due to the absorption/scattering by dye molecules as it progresses in the test medium even under an ideal optical configuration. Furthermore, the optical limitation and uncertainty of the CCD camera response can hardly guarantee persistent intensity levels from test to test.

One way to correct for the spatial nonuniformity would be to carry out point-by-point corrections for measured LIF images using a large set of reference images taken at several different temperatures, so that the dependency of LIF quenching can be appropriately accounted for, the local temperature as well as for the spatial nonuniformities of the background illumination. However, this requires that the imaging field configurations be precisely identical for both calibration and measurement, which in turn requires the use of the same setup for both calibration and measurement. This makes the LIF technique using a single dye very cumbersome in that a new calibration will be needed for every different experimental configuration.

A more reliable and noble way to bypass these issues is to normalize the fluorescence intensity of the temperature dependence dye with a temperature independent dye. This ratiometric LIF, as it has come to be known originated from the field of biology, is also called dual emission LIF [13] and two-color LIF [14,15]. Coppeta and Rogers [13] comprehensively describes the technique and showed experimental results to demonstrate the feasibility, for not only temperature but also pH as well, for the case of a moderate scale test field of 100-mm thermal plume. Sakakibara and Adrian [14,15], which came out about the same time, showed a calibration uncertainties of ±1.5 K over a 25 K temperature range and applied this technique to measure a three-dimensional thermal convection field above a heated horizontal surface of 40-mm square in dimension.

The present work uses a similar ratiometric LIF technique to quantitatively examine the measurement accuracy, in conjunction with its spatial resolution, for feasibility as a microscale temperature field-mapping tool. A 1.0-mm wide cuvette is heated differentially on opposite vertical sides so as to generate a natural convection thermal field, with relatively low Grashof–Prandtl number, $Gr_wPr < 300$, and the resulting steady temperature field has been measured by the ratiometric LIF technique. The measurement accuracy is assessed by comparing the measured temperature field with computational predictions, which can be considered accurate for the near-conduction regime of low Gr_wPr, and the measurement uncertainties are determined for different spatial resolutions ranging from 4.2 to 76 μm.

2. Experimental setup

The present system uses Rhodamine-B (absorption peak at 554 nm and emission peak at 575 nm) as a temperature sensitive dye, as high as 2% intensity change per K, and Rhodamine-110 (absorption peak at 496 nm and emission peak at 520 nm) as a temperature insensitive dye, as low as 0.13%/K. Both fluorescent dyes are pumped by the "blue" Ar-ion CW laser light band-peaked at 488 nm.

In the absence of the pH-dependence of both dyes, the intensity ratio of the two fluorescence emissions is given as

$$\frac{I_{\mathrm{rhb}}}{I_{\mathrm{rh110}}} = \frac{I_{0\mathrm{rhb}}\varepsilon_{\mathrm{rhb}}[c]_{\mathrm{rhb}}Q_{\mathrm{rhb}}}{I_{0\mathrm{rh110}}\varepsilon_{\mathrm{rh110}}[c]_{\mathrm{rh110}}Q_{\mathrm{rh110}}} \tag{1}$$

where the ratio of the absorption spectral intensity, $I_{0\mathrm{rhb}}/I_{0\mathrm{rh110}}$, is invariant when a single illumination source is used for both dyes, and the molar absorptivity ε is nearly independent of temperature [12]. For a fixed concentration ratio of the two dyes, $[c]_{\mathrm{rhb}}/[c]_{\mathrm{rh110}}$, the fluorescence intensity ratio, $I_{\mathrm{rhb}}/I_{\mathrm{rh110}}$, will only depend on the quantum efficiency ratio, $Q_{\mathrm{rhb}}/Q_{\mathrm{rh110}}$, which may be correlated to temperature. A careful calibration is needed to determine a functional correlation between the fluorescent intensity ratio ($I_{\mathrm{rhb}}/I_{\mathrm{rh110}}$) and temperature of test medium containing small concentrations of both fluorescent dyes.

The use of two-cameras [14,15], with a dichroic beam splitter, can simultaneously detect both emissions from the two fluorescent dyes. However, the pixel-by-pixel correspondence between the two camera images must be ensured by a reference-imaging object such as a grid plate [16]. Furthermore, the use of the beam splitter will alter the spectral characteristics of the transmitted and reflected wavelengths because of the wavelength-dependent dispersion of the inclined incoming rays at 45° incident angle onto the beam splitter [17]. Thus, the intensity ratio at a given temperature becomes spatially dependent within the image plane, and this requires a cumbersome point-by-point calibration for the entire field-of-view over a range of temperatures.

The single-camera system (Fig. 1) sequentially detects each fluorescence signal by alternating the two band-pass filters, a long-pass filter ($\lambda_T > 560$ nm) for Rh-B detection and a narrow band-pass filter (505 nm $< \lambda_T <$ 515 nm) for Rh-110 detection. Since the camera detects para-normal incident rays the spectral dispersion problem is minimized and the need for point-by-point calibration is not necessary. Also, the single-camera system requires less attention to image coincidence and is relatively insensitive to external vibrations. The primary

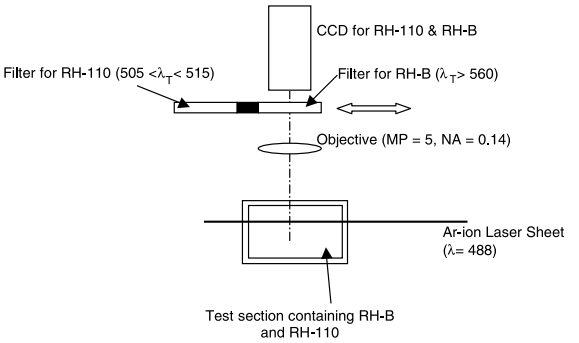

Fig. 1. Schematic illustration of the modified ratiometric LIF thermometry system.

limitation of the simplified system is resulted from the sequential image recording, and the single-camera system is unable to handle unsteady thermal problems. The single-camera ratiometric LIF system, however, is believed to be more reliable and convenient than the dual camera setup for investigating steady thermal problems.

3. Calibration experiments

A calibration experiment was conducted using an isothermal cuvette immersed in a constant temperature chamber in order to determine the correlation between the fluorescence intensity ratio and temperature. The 15-cm cubic constant temperature chamber is made of 6.3-mm thick insulated plexiglass and the chamber is connected to a thermobath to complete a closed loop circulation of constant temperature fluid (water). The calibration cuvette of 10-mm square cross-section and 50-mm long was filled with purified water containing 6-mg/l concentration of Rh-B and 1-mg/l concentration of Rh-110. The cuvette was placed within the constant temperature chamber and chamber temperature was monitored using a K-type thermocouple probe. It took approximately 20 min until temperature of thermocouple reached to set temperature within ±0.5 °C. Fluorescence was induced using a laser sheet passing through the top of the cuvette and the fluorescence intensity signals were detected through a 3.5-cm square optical window located in the front wall of the constant temperature chamber.

An interline transfer monochromatic CCD camera (maximum 640×480 pixels resolution, approximately 9.0 μm pixel size, Sony XC-73) with a Mitutoyo 5× objective lens (NA = 0.14) having an extended working distance of approximately 37 mm was used to record images of an approximately 3.0 mm × 2.0 mm. Note that due to the chemical and photochemical decomposition, the emission intensity of fluorescence dye degrades during repeated excitation and emission transitions [18]. The lowered fluorescence emission levels of degraded dyes made LIF images difficult to record. What we have found for the best to achieve accuracy and repeatability is to use fresh mixtures not older than two or three days.

Fig. 2 plots fluorescence intensity for the two dyes (Rh-B and Rh-110) against a temperature range of 16–40 °C, where different symbols represent individual data sets taken at three different times during the calibration period ensuring the acceptable repeatability. Each data point represents the average intensity of the central 1.5-mm × 1.0-mm field-of-view (320 by 240 pixels), in order to exclude the potentially degraded image of the off-axis region, and averaged for ten (10) recorded images. The discrepancy between the three calibration data sets are less than 5%. Though the entire calibration test section should remain ideally at a uniform temperature, the aforementioned nonideal optical and thermal factors may result in slight spatial nonuniformity in the fluorescence intensity. These nonideal factors include nonuniformity in the background illumination, which cannot be completely abated, inherent fluorescence intensity variations due to thermal drift of dye molecules caused by small temperature gradients in the cuvette, and by imperfections and unsteady noise in the CCD pixels.

Assuming a normal distribution of the measured temperature data scattered around the expected value (m), the calibration uncertainty levels are estimated based on a 95%-confidence level standard deviation ($\pm 2\sigma$). Table 1 shows the calibration uncertainties depending on the interrogation cell sizes, with the maximum uncertainty shown for the pixel-by-pixel variation (4.7-μm by 4.2-μm spatial resolution) and zero uncertainty when averaged for the whole calibration field-of-view (1.5-mm by 1.0-mm spatial resolution). Each uncertainty value represents the average across the tested

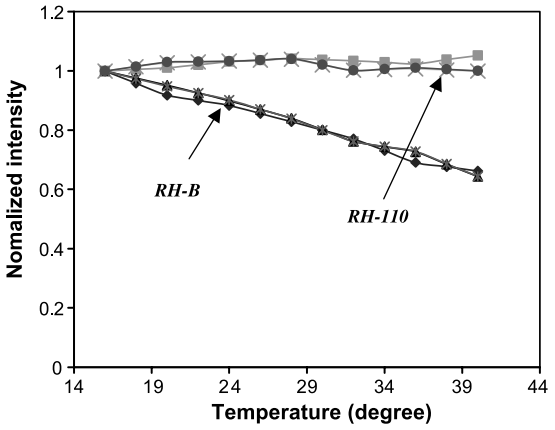

Fig. 2. Comparison of fluorescence intensities of RH-B and RH-110, normalized by the corresponding intensities at 14 °C, for calibration data for the two-color ratiometric thermometry.

Table 1
Dependence of the calibration uncertainties with 95% confidence level on the interrogating cell size

Interrogation cell (pixels)	Spatial resolution (μm)	Intensity ratio uncertainties	Temperature uncertainties (°C)
1 by 1	4.7×4.2	±0.143	±5.635
10 by 10	47×42	±0.056	±2.964
32 by 24	150×100	±0.043	±1.967
64 by 48	300×200	±0.033	±1.496
128 by 96	600×400	±0.022	±1.006
256 by 192	1200×800	±0.009	±0.412
320 by 240	1500×1000	±0	±0

temperature range from 16 to 40 °C, and ten images at each temperature. The measured temperature uncertainties exhibit an adverse dependence on the interrogating cell size, showing dramatic decrease with increasing interrogation cell size. For example, the calibration uncertainty decreases from ±1.967 °C for 150-μm by 100-μm interrogation cell to ±0.412 °C for 1200-μm by 800-μm interrogation cell.

Brownian diffusive motion may become a considerable factor when sub-micron particles are used for a tracer since the particle diffusivity rapidly increases with decreasing particle diameter. The molecular weight of Rh-B and Rh-110 are heavier than the surrogating water molecules by an order of magnitude or more [19]. Water molecule size is known to be about 0.14 nm and Rhodamine particle sizes are estimated to be an order of a few nanometers [20]. Therefore, these ''particles'' are expected to rather disperse as small particles than dissolve as molecules such as for alcohol–water mixture. In addition, the Rhodamine dyes are likely to form a large cluster due to their highly probable coagulation in water unless special care is exercised to eliminate coagulation. It is believed that the Brownian motion can describe the dispersion of Rh-B and Rh-110 ''compound'' dye molecules to an extent.

The root-mean-square (r.m.s.) particle displacement by the Brownian motion during an elapsed time interval Δt is given as $\bar{x} \approx \sqrt{2D \cdot \Delta t}$ [21], and the diffusivity is given as [22],

$$D = \frac{kT}{3\pi\mu d_{\mathrm{p}}} \approx 4.29 \times 10^{-10}\ \mathrm{m^2/s} \tag{2}$$

where $d_{\mathrm{p}} \approx 1.0$ nm for individual fluorescent compound dye molecules (in reality, coagulated dye molecules can form a cluster as large as 50 nm as evidenced by transmission electron microscopy (TEM) at Texas A&M Electron Microscopy Center), the absolute viscosity of water $\mu = 1.0 \times 10^{-3}$ N s/m^2 at 20 °C, and the Boltzmann's constant $k = 1.38 \times 10^{-23}$ J/K. For the recording period of $\Delta t = 0.05$ s (corresponding to the maximum recording time for 20 fps, and Δt can be substantially shorter when an electronic shutter controls the exposure time), the Brownina displacement is approximately 4.6 μm. In other words, the Brownian diffusion may render the spatial resolution with ±4.6-μm uncertainties.

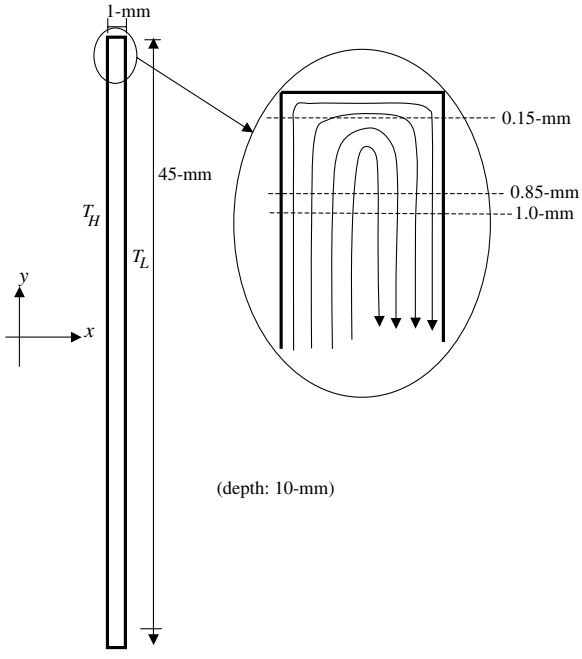

Fig. 3. Test cuvette consisting of heated (T_{H}), cooled (T_{L}), and adiabatic top and bottom walls.

4. Results and discussion

The test cuvette (Fig. 3) has dimensions of 1-mm wide (w), 10-mm deep (d), and 45-mm high (h). Each of the two sidewalls (10-mm deep and 45-mm high) is maintained at a different temperature by conduction from an attached copper jacket through which water circulates to and from a controlled thermobath. The temperature differential between the two sidewalls establishes a steady, thermally-driven buoyant flow, as schematically shown in the inset illustration of Fig. 3. The top and bottom surfaces of the cuvette are insulated to provide an adiabatic condition. A thermocouple probe embedded near the middle of each sidewall, at 0.1-mm depth from the contacting surface, monitors the surface temperature persistence.

The experimental results are compared with numerical predictions to locally and quantitatively examine the measurement accuracy and spatial resolution. The pertinent laminar natural convection flow inside a closed rectangular boundary is predicted using a standard computational technique. The conventional finite volume method [23,24] is used to solve the two-dimensional and steady-state mass, momentum and energy equations for temperature and velocity fields for the identical boundary conditions as used in the experiments. The following assumptions are made for the mathematical formulation used for modeling:

1. The working fluid is Newtonian, with a constant viscosity, and incompressible.
2. All thermophysical properties are assumed remaining constant at 300 K.
3. No-slip boundary conditions are applied to the channel wall.
4. The Boussinesq approximation for the momentum transport is used to accommodate the buoyant effect due to the thermal convection density variation.

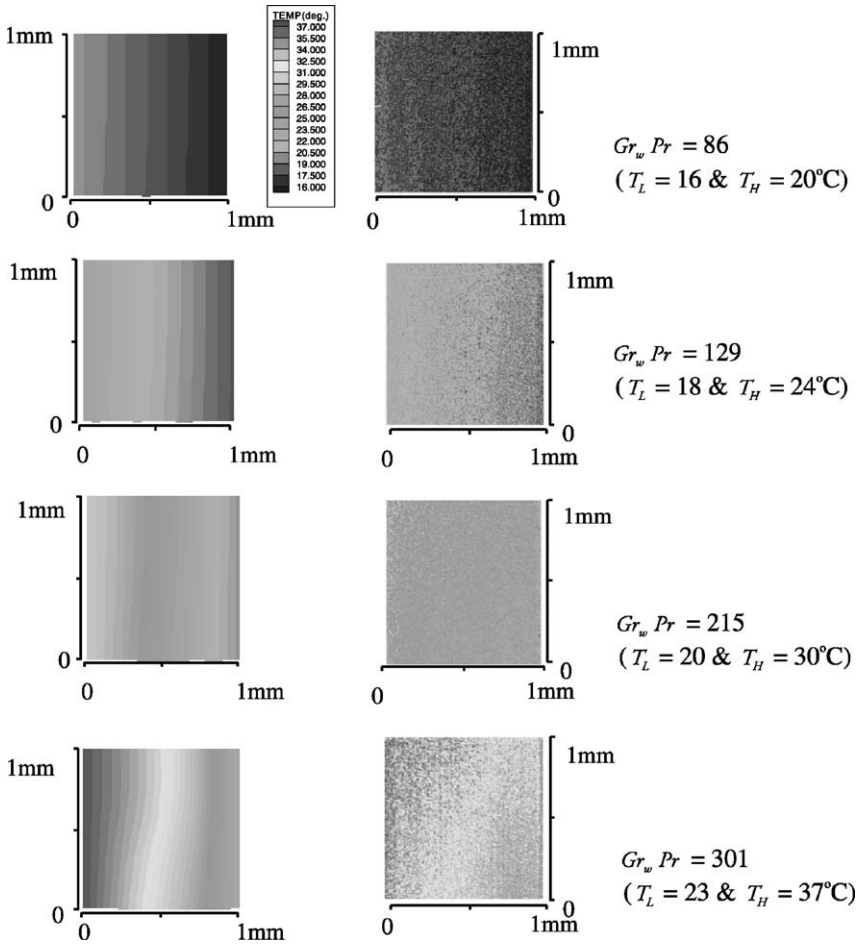

Fig. 4. Calculated (the left column) and measured (the right column) temperature contours for the top 1.0-mm by 1.0-mm region.

The dependent variables of T, p, u, and v are iteratively calculated from the elliptical momentum and energy equations. The uniform grid dimension is set to 17 across the 1-mm channel width and 540 for the 45-mm height, and thus, the computational grid size is set to approximately 58.8 μm by 83.3 μm. Although not shown, smaller grid sizes do not alter the resulting solutions.

Fig. 4 shows comparison between the calculated (the left column) and the measured (the right column) temperature distributions for the top 1.0-mm by 1.0-mm square region of the test cuevette. Four different wall temperature differentials, 16–20, 18–24, 20–30 and 23–37 °C, are considered with their corresponding Grashof–Prandtl number, $Gr_wPr \equiv \frac{g\beta\Delta Tw^3}{\nu^2}\cdot\frac{\nu}{\alpha} = 86$, 129, 215, and 301, respectively (at 300 K, the expansion coefficient, $\beta = 2.76\times10^{-4}$ K^{-1}, the kinematic viscosity of water, $\nu = 8.567\times10^{-7}$ m^2/s, the thermal diffusivity, $\alpha = 1.470\times10^{-7}$ m^2/s, and the channel width, $w = 1.0$ mm). The measured and calculated temperature contours

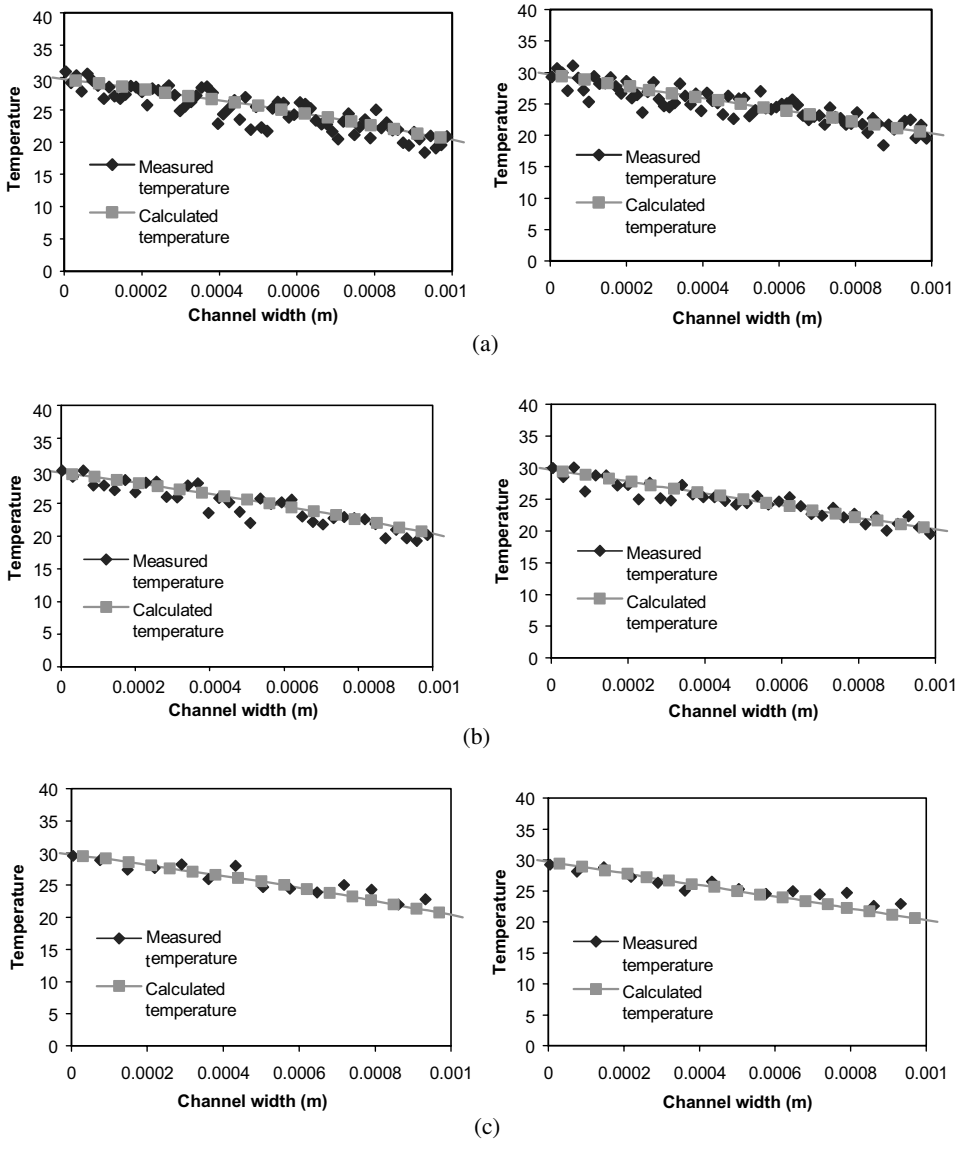

Fig. 5. Temperature profiles for the case of $Gr_wPr = 215$ ($T_L = 20$ °C and $T_H = 30$ °C): (a) spatial resolution: 19 μm (H) by 19 μm (V), (b) spatial resolution: 38 μm (H) by 38 μm (V), (c) spatial resolution: 76 μm (H) by 76 μm (V).

Table 2
Root-mean-square (r.m.s.) fluctuations of the measured temperature data from the predicted values for different spatial resolutions (Ref. to Fig. 5: $Gr_wPr = 215$; $T_L = 20$ °C and $T_H = 30$ °C)

Spatial resolution (μm × μm)	0.15 mm below the top	0.85 mm below the top
19 × 19	2.377 °C	2.306 °C
38 × 38	1.574 °C	1.566 °C
76 × 76	0.999 °C	0.924 °C

show fairly good agreement each other in that the temperature contours gradually deviate from the vertically stratified distributions with increasing Gr_wPr.

At such low Grashof–Prandtl numbers, there exists little free-convection current and the heat transfer occurs mainly by conduction across the fluid layer [25]. The horizontal variation in temperature should remain largely linear when the flow remains in the conduction regime of $Gr_wPr < 10^3$ as long as $h/w > 10$. Fig. 5 shows local and more quantitative comparisons between the measured and calculated temperature profiles at 0.15 mm (the left column), and 0.85 mm (the right column) below the top, for a representative case of $Gr_wPr = 215$. To examine the measurement uncertainties as a function of the spatial measurement resolution, the original pixel-by-pixel data are combined to 4×4, 8×8, and 16×16-pixeled interrogation cells, corresponding to the spatial resolution of 19 μm (H) by 19 μm (V), 38 μm by 38 μm, and 76 μm by 76 μm, respectively. Note that the spatial resolution for numerical calculations is remained as 58.8 μm (H) by 83.3 μm (V) for all the cases.

The data fluctuations should decrease with increasing number of the spatial samplings and the uncertainties are proportional to $1/\sqrt{N}$, for the case of multiple (N) samplings with N approaching to infinity. The root-mean-square (r.m.s.) fluctuations of the measured temperature data, from the calculated predictions, show persistent reduction from over 2 °C to below 1 °C, with measurement resolution changing from 19 μm square to 76 μm square (Table 2).

5. Conclusive remarks

A ratiometric (two-color) LIF technique has been examined primarily for its measurement uncertainties depending on the spatial resolution in order to explore the use for microscale full-field temperature mapping:

(1) The standard deviation of the temperature calibration, with 95% confidence level, range from ±1.967 °C for the 150 μm × 100 μm calibration field-of-view size, to 0.412 °C for 1200 × 800 μm view.
(2) For the tested 1.0-mm heated closed cuevette, the r.m.s. fluctuations of the measured temperature from the computational predictions show persistent decrease from 2.3 °C for 19 μm spatial measurement resolution to 0.92 °C for 76 μm resolution.

Acknowledgements

This material is based on the work supported by the National Center for Microgravity Research (NCMR). Dr. H.J. Kim wishes his gratitude for partial support arranged by Prof. J.S. Yoo of the National Research Laboratory (NRL) Program of Ajou University, established by the Ministry of Science and Technology, Korea. Any opinions, findings, and conclusions or recommendations expressed in this publication are those of the authors and do not necessarily reflect the view of the NCMR or the NRL.

References

[1] E.R.G. Eckert, R.J. Goldstein, Measurements in Heat Transfer, McGraw-Hill, New York, 1970.
[2] D. Dabiri, M. Gharib, Digital particle image thermometry and its application to a heated vortex ring, in: Fluid Measurement and Instrumentation Forum, ASME FED-95, 1990, pp. 27–34.
[3] D. Dabiri, M. Gharib, Digital particle image thermometry: the method and implementation, Exp. Fluids 11 (1991) 77–86.
[4] C.D. Richards, R.F. Richards, Transient temperature measurements in a convectively cooled droplet, Exp. Fluids 25 (1998) 392–400.
[5] M. Pehl, F. Werner, F.A. Delgado, First visualization of temperature fields in liquids at high pressure using thermochromic liquid crystals, Exp. Fluids 29 (2000) 302–304.
[6] D.R. Sabatino, T.J. Praisner, C.R. Smith, A high-accuracy calibration technique for thermochromic liquid crystal temperature measurements, Exp. Fluids 28 (2000) 497–505.
[7] J. Sakakibara, K. Hishida, M. Maeda, Vortex structure and heat transfer in the stagnation region of an impinging plane jet (simultaneous measurements of velocity and temperature fields by digital particle image velocimetry and laser-induced fluorescence), Int. J. Heat Mass Transfer 40 (13) (1997) 3163–3176.
[8] S.S. Chu, C.P. Grigoropoulos, Determination of kinetic energy distribution in a laser-ablated titanium plume by emission and laser-induced fluorescence spectroscopy, J. Heat Transfer 122 (2000) 771–775.
[9] T. Nakajima, M. Utsunomiya, Y. Ikeda, R. Matsumoto, Simultaneous measurement of velocity and temperature of water using LDV and fluorescence technique, in: The 5th Int. Symp. on Application of Laser Techniques To Fluid Mechanics, Lisbon, 1990, pp. 2.6.1–2.6.6.
[10] K. Sato, N. Kasai, Combined velocity and scalar field measurement with the simultaneous use of scanning PIV and LIF, in: The 10th Int. Symposium on Transport

Phenomena in Thermal Science and Process Engineering (ISTP10), 1997.
[11] M.C.J. Coolen, R.N. Kieft, C.C.M. Rindt, A.A. van Steenhoven, Application of 2-D LIF temperature measurements in water using a Nd-Yag laser, Exp. Fluids 27 (1999) 420–426.
[12] D.L. Andrews, Lasers in Chemistry, Springer-Verlag, Berlin, 1986.
[13] J. Coppeta, C. Rogers, Dual emission laser induced fluorescence for direct planar scalar behavior measurements, Exp. Fluids 25 (1998) 1–15.
[14] J. Sakakibara, R.J. Adrian, Measurement of whole field temperature using two-color LIF, J. Visual. Soc. Jpn. 17 (1997) 333–336.
[15] J. Sakakibara, R.J. Adrian, Whole field measurement of temperature in water using two-color laser induced fluorescence, Exp. Fluids 26 (1999) 7–15.
[16] S. Soloff, R.J. Adrian, Z. Liu, Distortion compensation for generalized stereoscopic particle image velocimetry, Meas. Sci. Technol. 8 (1997) 1441–1454.
[17] E. Hecht, Optics, fourth ed., Addison Wesley, Reading, 2002.
[18] J.R. Salor, Photobleaching of disodium fluorescein in water, Exp. Fluids 18 (1995) 445–447.
[19] American Association of Textile Chemists and Colorists, Color Index, 3rd ed., vol. 4, The Society of Dyers and Colorists, 1971.
[20] H.S. Choi, personal communications, Department of Chemical Engineering, Kyungil University, Kyungsan, Korea, 2003.
[21] A. Einstein, On the Movement of Small Particles Suspended in a Stationary Liquid Demanded by the Molecular-Kinetic Theory of Heat: Theory of the Brownian Movement, Dover Publications, New York, 1905, pp. 1–8.
[22] S.K. Friedlander, Smoke, Dust and Haze, Wiley, New York, 1977.
[23] A. Chuichi, Computational Fluid Dynamics for Engineering, University of Tokyo Press, Tokyo, 1994.
[24] S.V. Patankar, Numerical Heat Transfer and Fluid Flow, Taylor & Francis, New York, 1980.
[25] R.K. McGregor, A.P. Emery, Free convection through vertical plane layers: moderate and high Prandtl number fluids, J. Heat Transfer 91 (1969) 391–396.

8.2 Optical Sectioning in Microchannels via Confocal Microscopy

Three-Dimensional Microfluidic Measurements Using Optical Sectioning By Confocal Microscopy

- Flow Around a Bubble Trapped in a Micro-Channel -

J.S. Park and K.D. Kihm
Department of Mechanical Engineering
Texas A&M University, College Station, Texas 77843-3123

J.S. Allen
National Center for Microgravity Research
NASA Glenn Research Center, Cleveland, Ohio 44135

Proceedings of the IMECE2002
ASME International Mechanical Engineering Congress & Exposition
November 17-22, 2002, New Orleans, Louisiana
Paper No. IMECE2002-37290

Abstract

Microscopic visualization of the transport phenomena associated with an air bubble entrained in liquid flowing through a microchannel has revealed a transition in the bubble shape and proximity to the channel walls with increasing flow rates. Experiments have been conducted to investigate the effect of channel geometry (three different microchannels with square cross-sections, 1.0-mm, 500-μm and 100-μm), and flow conditions (Capillary numbers ranging from 0 to 0.23) on the transition in bubble shape. In addition, micro-Particle Image Velocimetry (μ-PIV) has been used to map the detailed flow field around the bubble and an innovative attempt has been made to provide optically-sectioned image recordings using a state-of-the-art high-speed Confocal Laser Scanning Microscope (CLSM) technique. The research presented herein is directed towards characterizing transport phenomena in two-phase (gas-liquid) flows in microchannels. Of particular interest to this research is the determination of entrance and exit length regions in two-phase microchannel flows. The experimental techniques being utilized towards the objective of characterizing two-phase flow transport phenomena in microchannels are the focus of the following discussion.

Proceedings of IMECE2002
ASME International Mechanical Engineering Congress & Exposition
November 17-22, 2002, New Orleans, Louisiana

IMECE 2002-32790

Three-Dimensional Microfluidic Measurements Using Optical Sectioning By Confocal Microscopy

- Flow Around a Bubble Trapped in a Micro-Channel -

J.S. Park and K.D. Kihm
Department of Mechanical Engineering
Texas A&M University, College Station, Texas 77843-3123

J.S. Allen
National Center for Microgravity Research
NASA Glenn Research Center, Cleveland, Ohio 44135

ABSTRACT

Microscopic visualization of the transport phenomena associated with an air bubble entrained in liquid flowing through a microchannel has revealed a transition in the bubble shape and proximity to the channel walls with increasing flow rates. Experiments have been conducted to investigate the effect of channel geometry (three different microchannels with square cross-sections, 1.0-mm, 500-μm and 100-μm), and flow conditions (Capillary numbers ranging from 0 to 0.23) on the transition in bubble shape. In addition, micro-Particle Image Velocimetry (μ-PIV) has been used to map the detailed flow field around the bubble and an innovative attempt has been made to provide optically-sectioned image recordings using a state-of-the-art high-speed Confocal Laser Scanning Microscope (CLSM) technique. The research presented herein is directed towards characterizing transport phenomena in two-phase (gas-liquid) flows in microchannels. Of particular interest to this research is the determination of entrance and exit length regions in two-phase microchannel flows. The experimental techniques being utilized towards the objective of characterizing two-phase flow transport phenomena in microchannels are the focus of the following discussion.

INTRODUCTION

Two-phase flow phenomena in capillary-dominated systems is common to numerous engineering systems; particularly heat transfer systems such as heat pipes, Capillary-Pumped Loops (CPL), and heat exchangers. Optimization of these technologies requires a more thorough understanding of the relationship between gas-phase transport and liquid-phase transport in capillary structures. Proton-Exchange Membrane (PEM) fuel cells are also capillary flow devices the performance of which is directly affected by two-phase flow phenomena [1]. The hydraulic diameter of the gas flow channels in a PEM fuel cell are typically on the order of 1 mm which is less than the capillary length. As the product water accumulates in the form of a liquid film on the walls in the gas flow channels of the cathode, perturbations can disturb the liquid film such that the channel becomes completely blocked by liquid, a phenomena known as "liquid holdup". This disrupts the flow of oxygen through the channel and, subsequently, to the membrane electrode assembly and the fuel cell performance is degraded. The factors which affect the stability of such a liquid film in a microchannel, such as entrance/exit regions and channel bifurcations, are not fully understood. The purpose of this research is to characterize microchannel two-phase flow transport phenomena.

NOMENCLATURE

Bo	Bond number, $\rho g d^2/\sigma$
Ca	Capillary number, $\mu U_b/\sigma$
D	Channel diameter, m
D_c	Characteristic length, m
d	Bubble diameter, m
f	Focal length of lens, m
g	Gravitation acceleration, m/s^2
n	Refractive index of objective immersion medium
NA	Numerical aperture of objective
Re	Reynolds number, $\rho D_c U/\mu$
U	Velocity, m/s
U_b	Bubble velocity, m/s
WD	Working distance of objective, m
We	Weber number, $\rho D_c U^2/\sigma$
Greek	
λ	Wavelength of light
μ	Dynamic viscosity of working fluid, Pa·s
ν	Kinematic viscosity of working fluid, cSt
ρ	Density of working fluid, kg/m^3
σ	Gas-liquid interfacial tension, N/m

An important dimensionless group to this study is the capillary number (Ca) which is the velocity scaled by the capillary flow potential. The capillary number is equivalent to *We*/*Re* and is normally defined in the following form:

$$Ca = \frac{mU_b}{s} \qquad (1)$$

In order to insure that the systems under study were in the capillary-dominated flow regime, the channels were scaled so that the Bond number remained small ($10^{-4} < Bo < 10^{-2}$). The Bond number scales the effect of gravity to that of capillarity on the shape of a static liquid surface and is defined as:

$$Bo = \frac{rgd^2}{s} \qquad (2)$$

When the Bond number is less than 1, then capillary forces prevail on the shape of a liquid surface.

BACKGROUND

Several researchers have studied bubble behavior trapped in a circular tube including the bubble profiles and adjacent flow streamlines for a wide range of capillary numbers. The first experiments to determine the fraction of liquid deposited on the walls of the tube were performed by Fairbrother and Stubbs [4]. They derived an equation of relation between capillary number and fractional coverage, and Taylor [13] experimentally verified their results with a number of Newtonian fluids, extending $Ca = 1.9$. Taylor's experimental works were extended by Cox [3] to $Ca > 10$. The fractional coverage was found to reach an asymptotic value at a high capillary number. Goldsmith and Mason [7] studied the movements of single long bubbles in circular cross sectional tubes experimentally and theoretically. They published the experimental determination of streamlines in the viscous fluid and the shape of air-liquid interface. The bubble contours and film thickness were examined by visual observation through a microscope.

The velocity fields in the liquid phase surrounding a bubble in a channel have been measured using Particle Tracking Velocimetry (PTV) and Particle Image Velocimetry (PIV) techniques. Generally, PIV measurements have been conducted in macro-scale circular channels with diameters greater than 19-mm [2,11]. As the channel diameters are reduced to the 1-mm range, the traditional PIV technique becomes impractical and PTV techniques are substituted for PIV. A successful PTV measurement by Gauri and Koelling [5,6] determined the velocity fields around the tip of a bubble for a wide range of capillary numbers ($0.01 < Ca < 100$) in a circular channel.

In the case of a non-circular tube, namely a square channel, published results have been far less extensive due the limited use in engineering systems and the difficulty in fabrication. The advent of micro-fabrication techniques, primarily based on the photolithographic etching, provides for relatively easy manufacturing of systems utilizing complex distributions of microchannels of triangular, trapezoidal, rectangular, or square cross-section. Thus, micro-fabrication techniques are providing the impetus for numerous new technologies dependent upon fluid and thermal transport in non-circular geometries. These non-circular cross-sections produce asymmetric profiles of bubble shape and flow field, and this requires extra care and effort in obtaining experimental measurements; particularly for small Bond number systems. Kolb and Cerro [8] observed the bubble profile and determined stream lines for high capillary number flows ($0.01 < Ca < 10$) in a 2-mm square cross-sectional channel. They studied a shape transition of bubble cross section by capturing, separately, both images of side and diagonal planes, and determined the capillary number to be a very good measure of the profile transition from asymmetry to symmetry (i.e., to a detached cylindrical bubble) in the square channel.

Table 1 Synthesis of experimental two-phase channel flow studies.

Authors	Shape	Diameter	Technique
Kolb and Cerro (1991) [8]	Square	2.0-mm	Visualization
Polonsky et al. (1999) [11]	Circular	25-mm	PIV
Gauri and Koelling (1999) [6]	Circular	6.0-mm	PTV
Bugg and Saad (2002) [2]	Circular	19-mm	PIV

EXPERIMENTS

In this discussion, a back-lighting visualization technique for determining the shape transition of a translating bubble and a μ-PIV system to quantitatively measure flow field surrounding the bubble in a square cross-section microchannel are presented. The μ-PIV technique is based upon conventional PIV techniques, but utilizes high performance microscopes and fluorescence particles. This μ-PIV adaptation has been successfully used to probe the velocity fields of single-phase microscale flows [9,12]. Herein, we demonstrate the use of μ-PIV in two-phase microscale flows and considers the further adaptation of PIV measurements by optically sectioning the image data using high-speed Confocal Laser Scanning Microscopy (CLSM).

The microscale two-phase flow experiment facility (Fig. 1) consists of an advanced microscope, a high-speed CCD camera, an illuminating light source, and a precise capillary flow module. The inverted optical microscope (Olympus IX 50) was used for the visualization of bubble shape transformation and μ-PIV recordings. A high-speed CCD camera was an indispensable piece of equipment in this microscale experiment. The applied bubble speed was below 20-mm/s, but the bubbles in images captured by a 30-frame speed regular camera moved through the frame too quickly for determination of the bubble profile. An imaging detector capable of a high frame rate and a micron shutter speed is required to to effectively freeze the image of a translating bubble.

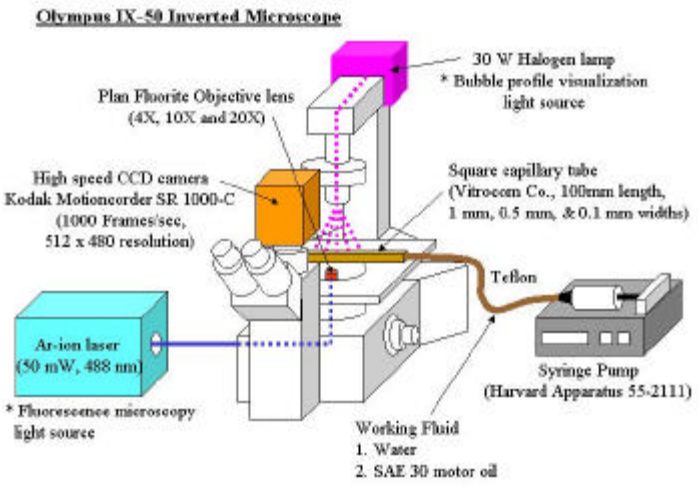

Fig. 1 Experimental setup

Initially, water was used as the working fluid (r = 997 kg/m^3, σ = 72 mN/m, and μ = 0.9 mPa·s at 23°C), but the desired capillary number required excessively fast bubble velocities due to the low value of water viscosity. Therefore, SAE-30 motor oil (r = 897 kg/m^3, σ = 30 mN/m, and μ = 350 mPa·s at 23°C) was chosen as the working fluid. Due to the temperature sensitivity of the viscosity of this fluid, both the working fluid and environmental temperatures were maintained at a constant 23°C.

The microchannels for the experiments were constructed using a commercially available square capillary tube (VitroCom, Inc.) that was precision made from Borosilicate glass with a length of 100-mm and flat, thin parallel walls, for optical access. The square capillary tube distorted the images due to ray refraction through the glass wall curvatures, particularly near the corners of the capillary. This distortion was overcome by attaching 200-μm thick microscope cover slips to the top and bottom surfaces of the channel using a cyanoacrylate adhesive which has approximately the same refractive index value as glass (Fig. 2). One end of the capillary tube was bonded with a Teflon tube and connected with a syringe pump (Harvard Apparatus Model 55-2111), and the other end was used for an inlet or drain. The working fluid and air bubbles were successively drawn into the open end of the capillary by the syringe pump. The syringe pump was used to accurately control the constant volumetric flow of the working fluid up to a maximum of 10 ml/hr. The square capillary tube assembly was placed horizontally on the precision microscope XYZ stage. A 30-watt halogen lamp is back illuminated to visualize the bubble profiles, and a 50-mW argon–ion laser is used to illuminate through the microscope objective for fluorescence μ-PIV and confocal microscopy.

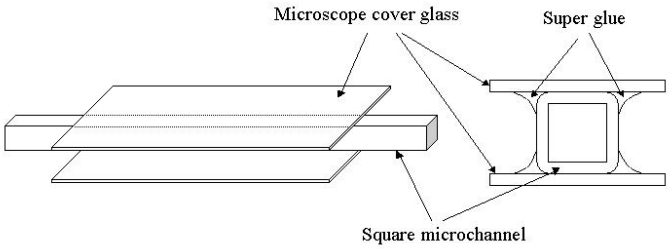

Fig. 2 Microchannel test cell

Bubble profile visualization. The bubble profile was be obtained by backlit illumination of the test section. The mismatch in the refractive index between the air and the SAE-30 oil resulted in a sharp image. The SAE-30 oil transmitted a high percentage of illuminating light although it was not a fully transparent fluid. Thus, the background was imaged bright while the bubble image appeared dark. A Kodak high-speed digital camera (Motioncorder, SR1000-C) was used to record images with the regular pixel resolution of 512 x 480. A frame rate of up to 1000 fps could be used with a reduced pixel resolution of 512 x 240. The higher frame rate implies a shorter shutter speed which requires a higher power illumination.

A single bubble translating at a range of capillary numbers ($0 < Ca > 0.23$) in capillary tubes of three sizes (1-mm, 0.5-mm, and 0.1-mm) were observed in order ascertain the bubble shape transition in sub-millimeter channel flow. The captured images were saved as an individual bitmap files then digitized and processed to get the bubble profiles using image-processing software (Adobe Photoshop).

m-Particle Image Velocimetry (m-PIV). Figure 3 shows a schematic of the present μ-PIV system where a 200-μm thick laser sheet illumination is produced by a 50-mW Argon-ion laser (Omnichrome, Inc.) in conjunction with cylindrical concave (Newport, f = 25-mm) and bi-convex lenses (f = 100-mm). 5-μm seeding particles are used for visualization. The bi-convex lens collimated the 1.0-mm diameter Argon-ion laser beam to a focused thinner laser sheet aligned perpendicular to the optical axis of the microscope. The thin laser sheet passed through the middle point of the capillary tube parallel with the top glass wall. The optical components had to be carefully aligned for microscopic visualization experiments since the use of a high magnification lens associated with multiple reflection/refraction test cell surfaces can result in severe distortion and unbalanced focusing of images.

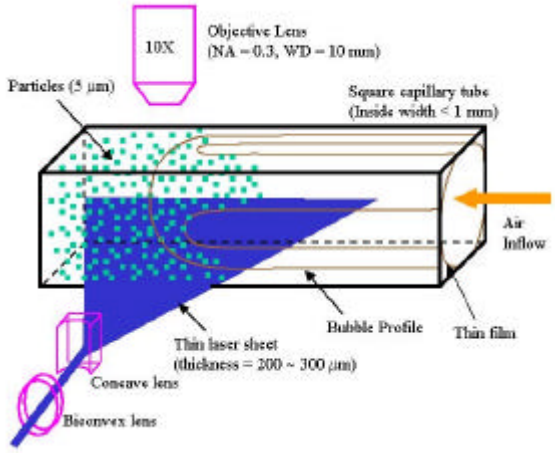

Fig. 3 Micro-PIV experiment system using Mie-scattering

The seeding particle size must be small enough to tolerably follow the flow without significantly disrupting the flow field and without producing unnecessarily large and/or bright images. In addition, the particles must be sufficiently large so as to produce visible and detectable images without being dominated by Brownian diffusion. The 5-μm particle is of proper scale to operate the typical PIV technique in 1-mm channel. The laser sheet is another consideration of PIV technique. As the sheet is thin and highly collimated, the captured images show sharp scattering effects. Also, the intensity of light has to be uniform in the whole field of the capturing section to the extent possible. The present PIV experiment used plan fluorite objective lenses (Olympus, Inc.) involving 4X (NA = 0.13), 10X (NA = 0.30), and 20X (NA = 0.50). The focus depth of the typical objective is defined as $n\lambda/NA^2$. This results in a depth of focus of approximately 7.2-μm with 488-nm laser light for n = 1.33. The depth-of-field defines the probe volume to be recorded and as such is crucial for micro PIV imaging.

The Kodak high-speed camera captured a sequence of particle images as bitmap files in proper frame rate and shutter speed, which were optimally selected by the capillary number, the illuminating power, and the sensitivity of CCD camera. The frame rate was set so that two consecutive images were closely interposed for a successive PIV analysis. The shutter speed was set such that particle images did not appear as streaks, but sufficient light was collected to accurately determine particle trajectories. The camera captured about 100 images for a specified capillary number at the appropriate frame rate.

The original pixel resolution captured by the Kodak SR 1000-C was a 512 x 480 pixels and the cropped images had a 360 x 230 (width x height) pixels. LaVision PIV software, Davis, was used to generate averaged vector fields from multiple raw particle images. The PIV software, using cross-correlation between two successive image, performed vector processing using two interrogation cell sizes of 8 x 8 pixels and 16 x 16 pixels. The post-processing for validation deleted vectors of correlation peak ratio $Q < 1.1$. A local median filter removed bad vectors if they were bigger than 1.5 RMS of its neighboring vectors and the average vector of the four neighboring vectors substituted for the bad vector. Techplot software was used to generate the contour plots.

RESULTS AND DISCUSSION

Visualization of bubble shapes and transition. Figure 4 shows a series of long bubble translating in three different sizes of square capillaries (1-mm, 500-µm, and 100-µm), and shows the bubble transitions with an increasing capillary number. In order to obtain sharp image contrast, the shutter speed of the camera was varied; 1/250-sec for the 100-µm channel, 1/500-sec for the 500-µm channel, and 1/1000-sec for the 1-mm channel. For the 100-µm capillary, a shutter speed of 1/250-second is slightly too long of an exposure time; as evidenced by the blurred bubble tip images shown in Fig. 4. But the limited light intensity of the present illumination source did not allow for a shorter shutter speed.

These preliminary results show that the transition in bubble shape is nearly identical to the previous findings of Kolb and Cerro [8] for larger capillaries. The critical capillary number is shown to be $Ca \sim 0.1$ and is not a function of the characteristic length for viscous flow.

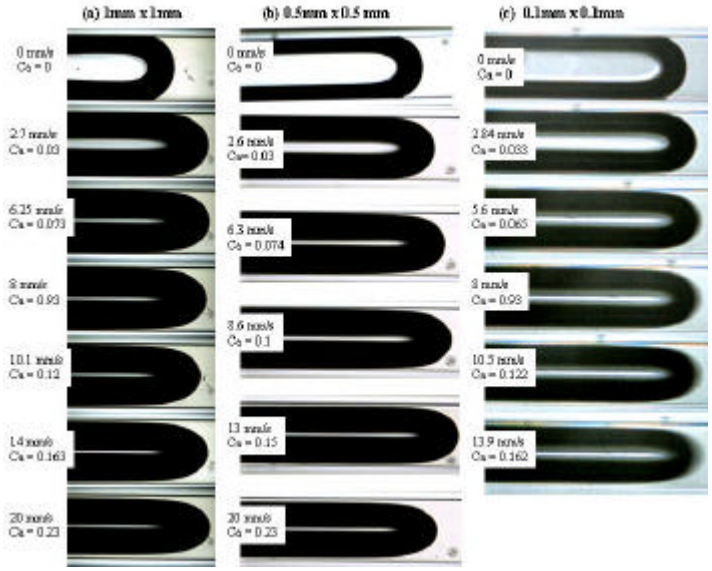

Fig. 4 Bubble shapes and transitions of three different channel dimensions for the range of capillary numbers up to 0.23. Effects of capillary number and micro-channel dimension on the air interface with SAE-30 motor oil (μ = 0.35-Ns/m^2, σ = 0.03-N/m).

Flow velocity field generation using µ-PIV. Figure 5 shows one raw PIV image and corresponding vector fields as measured near the tip of a bubble which is moving at 1.0-mm/s. Twenty (20) successive images were used to generate an averaged vector field and the PIV images were recorded at 30-frames/sec with 1/30-sec shutter speed. When the images were processed with an interrogation cell of 8 x 8 (Fig. 5-b), the vector field had a resolution of 43 x 29 vectors, and a vector-to-vector distance was about 34-µm. The 16 x 16 interrogation (Fig. 5-c) resulted in a vector resolution of 22 x 15 and a vector-to-vector distance of 69-µm. The particle image concentration, shown in the raw particle image (Fig. 5-a), suggests that the number of particle images for the 8 x 8 interrogation may be too low and the resulting vector fields contain a number of suspicious vectors, as a result of the statistical deficiency of the PIV data processing.

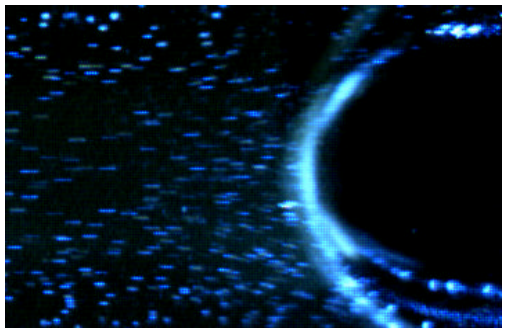

(a)

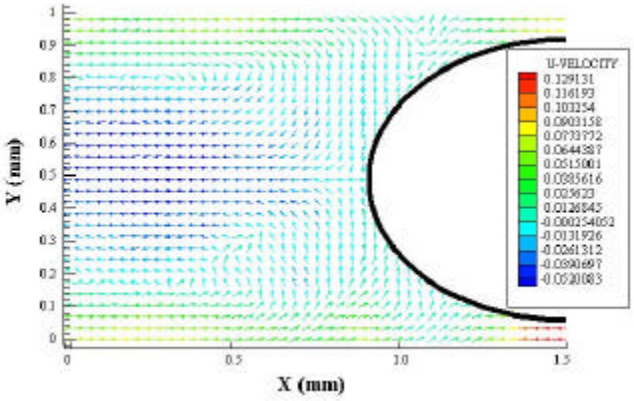

(b)

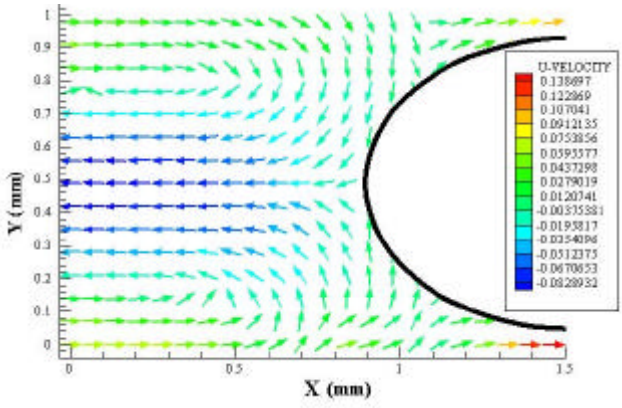

(c)

Fig. 5 A raw PIV image and flow velocity vector fields of 8 x 8 and 16 x 16 interrogations for the moving bubble at 1.0-mm/s.

Figure 6 illustrates the axial development of *U*-velocity profiles with increasing *x*-location approaching the bubble tip. The syringe pump pushes the air bubble into the quiescent liquid. Far from the tip of the translating bubble (at $x = 0$), a bi-directional flow is observed. The central negative maximum velocity is relaxed as the bubble tip is approached. The axial velocity profile eventually disappears in the region just ahead of the bubble (at $x = 0.98$) where the transverse velocity component dominates the flow.

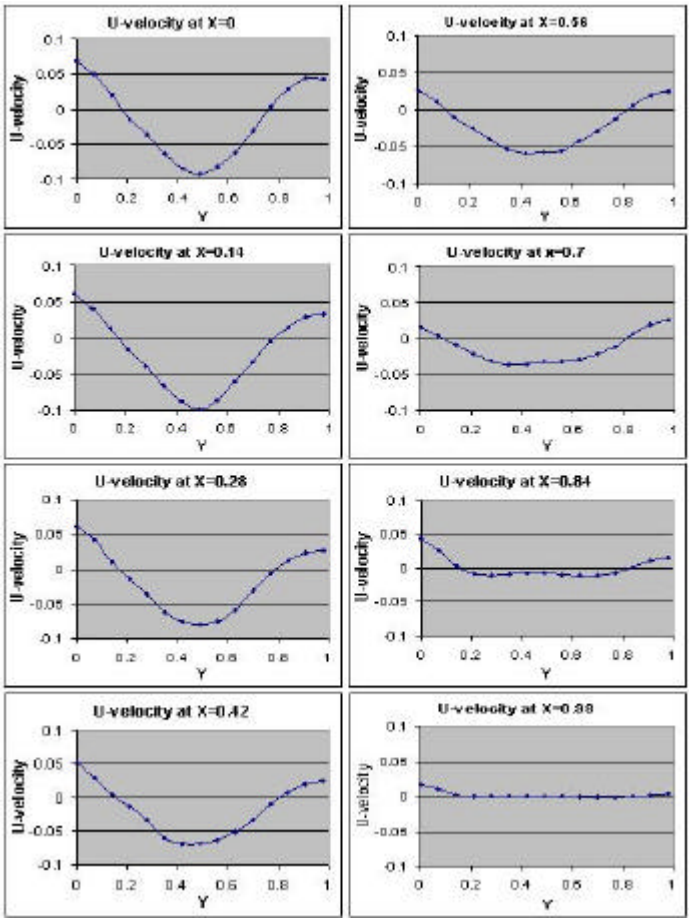

Fig. 6 Development of *U*-velocity profiles with increasing axial location, (*x*) measured approaching the bubble tip when the bubble is moving at 1.0-mm/s in the negative *x*-direction.

3-Dimensional confocal microscopy. A Confocal Laser Scanning Microscope (CLSM) System, patented by Dr. Marvin Minsky [10] at Harvard University in 1957, dramatically improves optical resolutions in microscopic imaging to an unprecedented level of 180-nm lateral resolution and 500-nm depth resolution. The most important feature of the CLSM is its ability to deliver thin, in-focus images by means of "Depth-wise Optical Sectioning" which allows the gathering of 3-D reconstructed information without the tedious, if not impossible, task of physically sectioning and manually reconstructing the 3-D field-of-view. The CLSM has been widely used in biology, material, and medical research to allow microstructures to be visible where they would be otherwise invisible because of the depth-wise obscurity. To date, no work using the CLSM in micro-fluidics has been published.

The conventional CLSM uses a point scanning of the laser excitation (Fig.7). The laser moves rapidly from point to point to produce the scanned image by the fluorescent light emitted from the focal point to the confocal point on the image plane of the detector. The pinhole aperture of about 50-μm diameter, located at the confocal point, allows emitted light, exclusively from the focal point, to pass through the detector (solid lines). Light emitted from outside the focal point is rejected by the aperture (dashed lines) and this is the key principle, to enhance the optical resolutions sufficiently to devise the depth-wise optical sectioning.

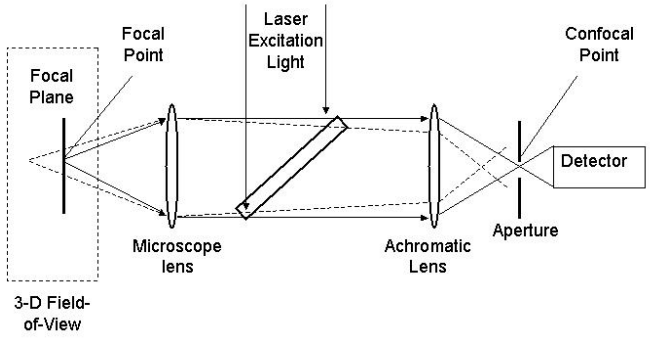

Fig. 7 Confocal Laser Scanning Microscope (CLSM) System.

The scanning rate of the above point-scanning CLSM is limited to approximately one (1) image per second (ips) because of the electronic/mechanical steering frequency constraint of the focal point (Fig. 7). Such a slow IPS of the point-scanning CLSM is a major drawback for micro-fluidic applications that need one or two order-of-magnitudes higher ips. The innovative Nipkow Disk Design [14] offers confocal full-field imaging at real-time 120-ips and this will allow optical sectioning to reconstruct three-dimensional imaging for micro-fluidic flows.

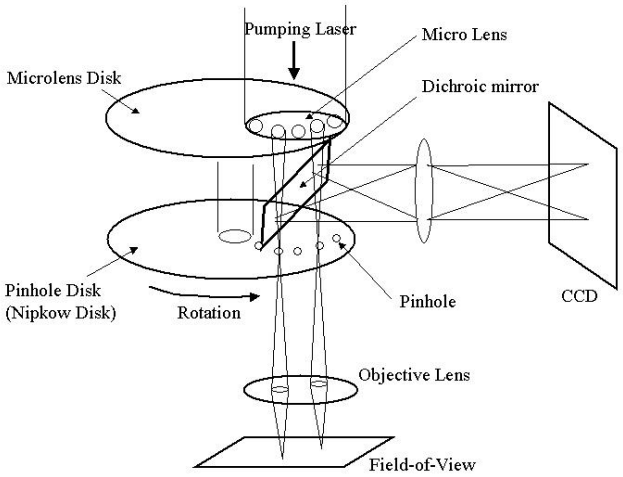

Fig. 8 Principle of dual Nipkow disk design CLSM (H. Ishida et al., Dept. of Physiol., TOKAI Univ.)

The essential innovation is the use of a high-speed spinning disk (360-rps) scanner, so called a Nipkow disk (Fig. 8), that consists of thousands of pinholes to allow significantly faster and simultaneous scanning (1,000 points) in contrast to the single-point-scanning technique. Both of the illumination and image light paths are defined by a similar optical path. The pumping light is focused by the micro-lens of the 1st Nipkow disk through the 50-μm pinholes on the 2nd disk. A dichroic mirror, located between the two disks, reflects the returning confocal image to the CCD for real-time, true color recording. As the disk rotates a high is achieved by averaging three sweeps per single field at up to 120-ips. The dual Nipkow disk CLSM head unit will be attached to the ocular speed

(360-rps) and the multiple pinholes sweep the view, a full field imaging port of the Olympus BX-61 microscope system.

CONCLUSIVE REMARKS

Bubble profile visualization was performed with SAE-30 motor oil in square capillary tubes of three different sizes of 1.0-mm, 0.5-mm, and 0.1-mm. The important dimensionless number, *Ca* was applied up to 0.23, and a critical value of *Ca* ~ 0.1 for transition from asymmetry to symmetry was verified for all capillary sizes. A μ-PIV technique has been developed and demonstrated that is capable of providing measurements of velocity fields with 34-μm vector-to-vector distance in two-phase flows of square capillary tubes.

This research will continue using the techniques describe; examining the bubble shape and μ-PIV measurements at higher *Ca* in order to identify instabilities of the liquid film between the bubble and the channel walls. Use of a confocal laser scanning microscope system will be used to reconstruct three-dimensional liquid film shapes and velocity fields. The use of smaller fluorescent seeding particles (200 ~ 500-nm in diameter) may be necessary to make effective visualization, particularly for the smallest 100-μm square channel.

ACKNOWLEDGMENT

The authors would like to gratefully acknowledge the financial and technical support for the presented work as a subcontracted project granted from the National Center for Microgravity Research/NASA-Glenn.

REFERENCES

[1] Allen, J., Kassemi, M., and McQuillen, J., 2000, "Characterization and Control of Two-Phase Flow in Microchannels," R4D Proposal, NCMR/NASA-Glenn.

[2] Bugg, J.D. and Saad, G.A., 2002, "The Velocity Field Around a Taylor Bubble Rising in a Stagnant Fluid: Numerical and Experimental Results," Int. J. Multiphase Flow, **28**, pp. 791-803.

[3] Cox, B.G., 1964, "An Experimental Investigation of the Streamlines in Viscous Fluid Expelled from a Tube," J. Fluid Mech., **20**, 193-200.

[4] Fairbrother, F. and Stubbs, A.E., 1935, "Studies in Electro-Endosmosis. Part VI. The "Bubble Tube" Method of Measurement," J. Chem. Soc., **1**, pp. 527-529.

[5] Gauri, V. and Koelling, K.W., 1999, "Gas-Assisted Displacement of Viscoelastic Fluids: Flow Dynamics at the Bubble Front," J. Non-Newtonian Fluid Mech., **83**, pp. 183-203.

[6] Gauri, V. and Koelling, K.W., 1999, "The Motion of Long Bubbles Through Viscoelastic Fluids in Capillary Tubes," Rheologica Acta, **38**, pp. 458-470.

[7] Goldsmith, H.L. and Mason, S.G., 1962, "The Movement of Single Large Bubbles in Closed Vertical Tubes," J. Fluid Mech., **14**, pp. 42-58.

[8] Kolb, W.B. and Cerro, R.L., 1991, "Coating the Inside of a Capillary of Square Cross Section," Chemical Engineering Science, **46**, No.9, pp. 2181-2195.

[9] Meinhart, C.D., Wereley, S.T. and Santiago, J.G., 1999, "PIV Measurements of a Microchannel Flow," Experiments in Fluids, **27**, pp. 414-419.

[10] Minsky, M., 1998, "Memoir on Inventing the Confocal Scanning Microscope," Scanning, **10**, pp. 128-138.

[11] Polonsky, S., Shemer, L. and Barnea, D., 1999, "The Relation Between the Taylor Bubble Motion and the Velocity Field Ahead of It," Int. J. Multiphase Flow, **25**, pp. 957-975.

[12] Santiago, J.G., Wereley, S.T., Meinhart, D.J., Beebe, D.J. and Adrian, R.J., 1998, "A Particle Image Velocimetry System for Microfluidics," Experiments in Fluids, **25**, pp. 316-319.

[13] Taylor, G.I., 1961, "Deposition of a Viscous Fluid on the Wall of a Tube," J. Fluid Mech., **10**, pp. 161-165.

[14] http://www.solameretech.com

8.3 μ-PIV using Confocal Laser Scanning Microscopy (CLSM)

Bi-Annual Report

(January 1, 2003 June 30, 2003)

Professor K.D. Kihm, Director

[TAMU Graduate Research Assistants]
Mr. J.S. Park
Mr. C.K. Choi
Mr. S.K.

Abstract

The primary achievement for the period from January 1, 2003 to June 30, 2003 was a systematic comparison of μ-PIV using Confocal Laser Scanning Microscopy (CLSM) with a regular epi-fluorescent μ-PIV, under identical flow conditions and identical supplementary optical conditions, such as image magnification, field illumination, and fluorescence filtering. Detailed flow measurements were conducted for two basic flows: (1) micro-Poiseuille flows in capillary pores of 100-μm and 500-μm diameters, and (2) rotating micro-Couette flows confined in a 180-μm layer.

BI-ANNUAL REPORT
(January 1, 2003 – June 30, 2003)

[Project Title]

Characterization and Control of Two-Phase Flow in a Microchannel

[Technical Project Monitor]

Dr. J.S. Allen
The National Center for Microgravity Research
NASA-Glenn Research Center
21000 Brookpark Road, MS-110-3
Cleveland, Ohio 44135
Tel: 216.433.3087, E-mail: jeff.allen@grc.nasa.gov

[Principal Investigator]

Professor K.D. Kihm, Director
Microscale Fluidics and Heat Transport Laboratory
Department of Mechanical Engineering
Texas A&M University
College Station, Texas 77843-3123
Tel: 979.845.2143, E-mail: ken-kihm@tamu.edu

[TAMU Graduate Research Assistants]

Mr. J.S. Park
Mr. C.K. Choi
Mr. S.K. Wee

July 3, 2003

Abstract

The primary achievement for the period from January 1, 2003 to June 30, 2003 was a systematic comparison of μ-PIV using Confocal Laser Scanning Microscopy (CLSM) with a regular epi-fluorescent μ-PIV, under identical flow conditions and identical supplementary optical conditions, such as image magnification, field illumination, and fluorescence filtering. Detailed flow measurements were conducted for two basic flows: (1) micro-Poiseuille flows in capillary pores of 100-μm and 500-μm diameters, and (2) rotating micro-Couette flows confined in a 180-μm layer.

Dual-Nipkow Disk High-Speed Confocal Laser Scanning Microscope (CLSM)

The innovative adoption of multi-pinhole Nipkow spinning disks for use for confocal microscopy (Fig. 1) allows for overcoming limitation due to the slow scanning speed (about 1-fps or slower) of conventional confocal microscopy. The Nipkow disk, named after its inventor Paul Nipkow, contains multiple sets of spirally arranged pinholes placed in the image plane of the objective lens. When spinning at a rapid rate, the pinhole coverage of the sample is completed several hundred times per second, effectively creating a full image scanning speed of up to 120-fps.

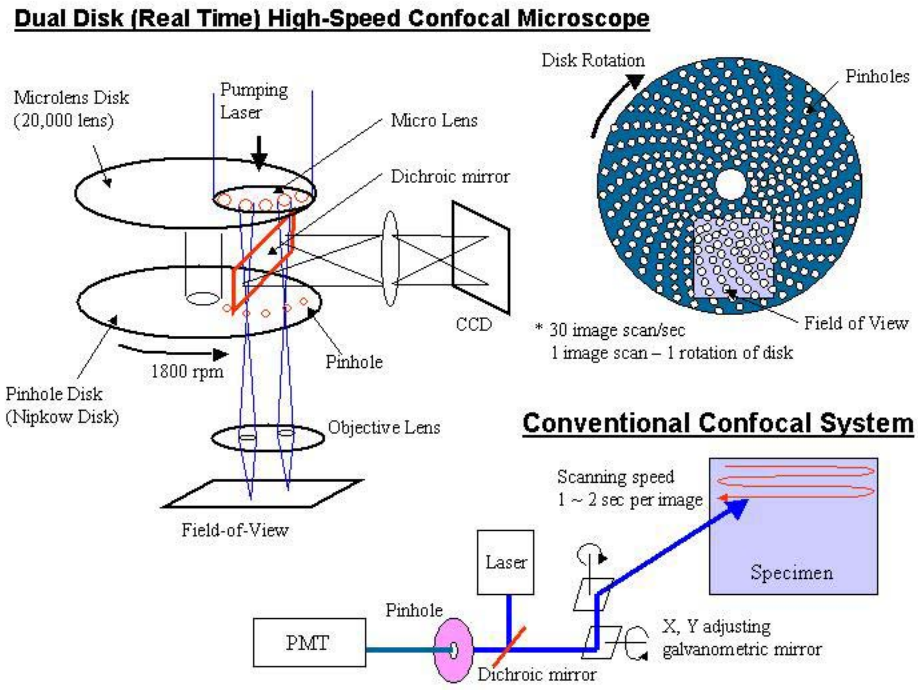

Figure 1. A Dual-Nipkow Disk High-Speed Confocal Laser Scanning Microscope (CLSM)

The dual-Nipkow disk Confocal Laser Scanning Microscopy (CLSM) allows the "confocal" concept to be used by μ-PIV, which can show a significant advantage in comparison with a regular epi-fluorescence μ-PIV. By having a confocal pinhole, the microscope is highly efficient at rejecting out-of-focus fluorescent light. The practical effect of this is that the image comes from an extremely thin section of test flow field providing a small depth-of-field, i.e., optically-sectioned PIV images by an order of one-micron thickness. By scanning many thin sections through your sample, you can buildup a very clean three-dimensional image of the sample. Also, a similar effect happens with points of light in the focal plane, but not at the focal point, the pinhole screen blocks emitted light from these areas. So a confocal microscope has slightly better resolution horizontally. In practice, the best horizontal resolution of a confocal microscope is about 0.2 microns, and the best vertical resolution is about 0.5 microns. As far as we know, the *Microscale Fluidics and Heat Transport Laboratory* of Texas A&M University is regarded as the first successful innovator of the confocal concept applied for μ-PIV.

μ-PIV Experimental Setup Using CLSM

The experimental setup (Fig. 2) consists of a CCD camera (UP-1830, UNIQ), confocal module (CSU-10, Yokogawa), inverted microscope (IX-50, Olympus), argon-ion laser (488-nm-50-mW, Laser Physics), frame grabber software (QED Imaging), computer, and a test section. The identical setup was used for both the micropore Poisselle flow and the rotating micro-Couette flow experiments.

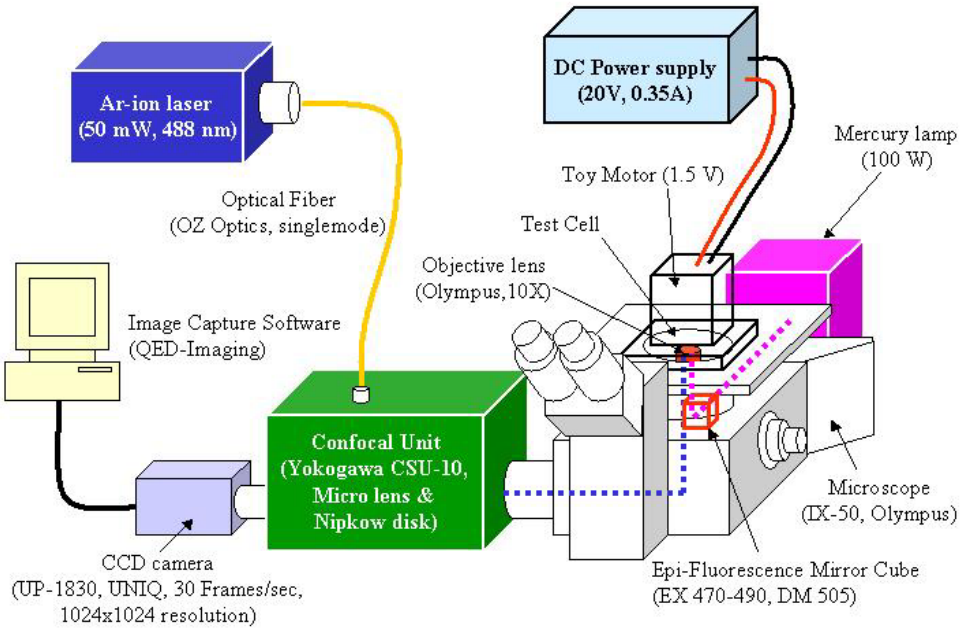

Figure 2. μ-PIV Experimental Setup Using CLSM

Micro-Poisselle Flows in 100-μm and 500-μm Diameter Micropores

Though the nominal pore diameter is given as 100-μm or 500-μm, the actual diameters had to be measured because any individual pore may have a variation in size. The cross-section of a pore was imaged by a microscope and its true diameter was measured using a calibrated reference scale. Figure 3 shows a demonstration of two different pore diameters that are supposed to be a nominal 100-μm in diameter.

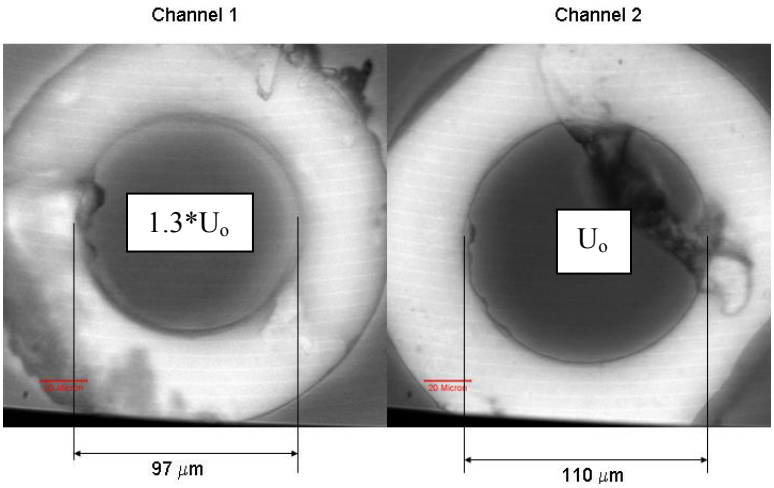

Figure 3. Variations of Capillary Pore Diameters and Flow Velocities

The center plane of the pore needs to be accurately located by first identifying the very top end of the inside pore and then lowering the focal plane by the distance corresponding to the precisely measured pore radius multiplied by the reciprocal of the refractive index of the test fluid of water (Fig. 4).

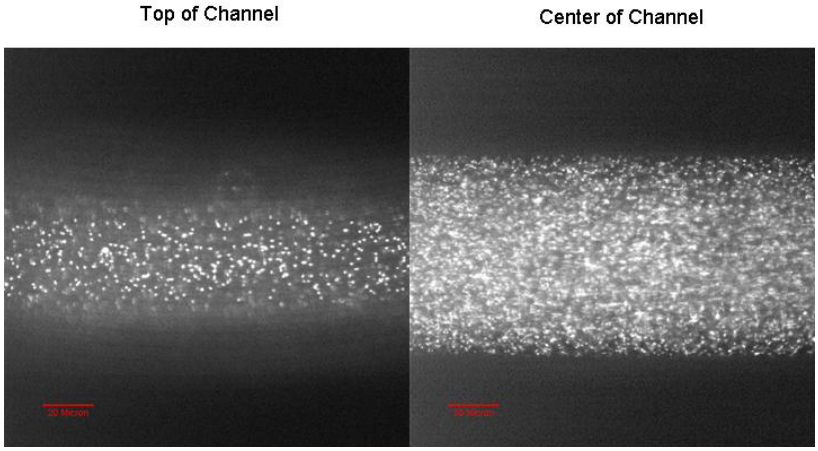

Figure 4. Confocal Images of the Top-End and the Center-Plane of the 100-μm Pore.

Summary of Experimental Parameters:

1. Pore diameter: 516-μm
2. Flow rate of syringe pump: 10-μl/hr (or 26.5-μm/s maximum velocity)
3. Number of image pairs: 29
4. Interrogation window: 32 x 32 pixels
5. Seeding particles: 200-nm fluorescent spheres at 0.001% in volume

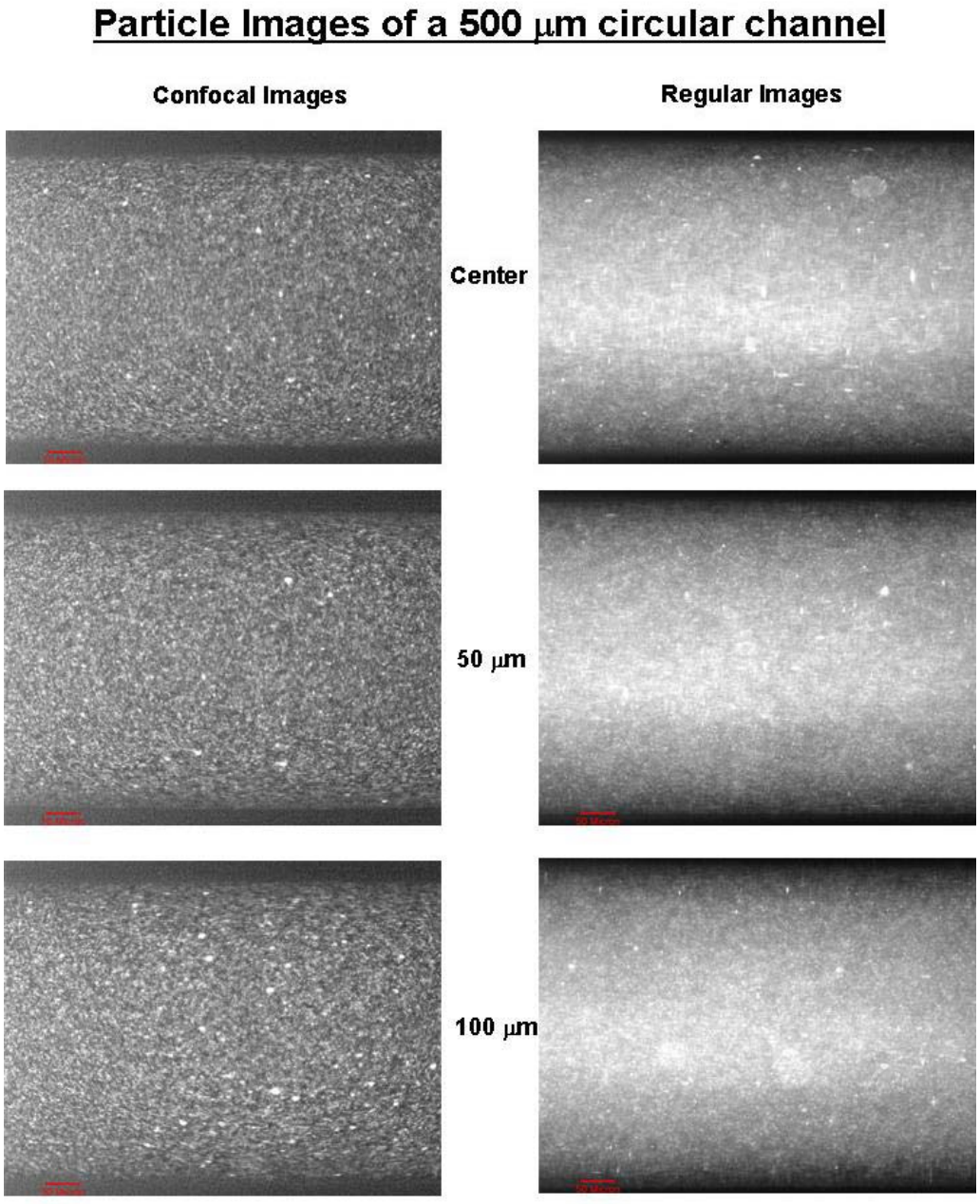

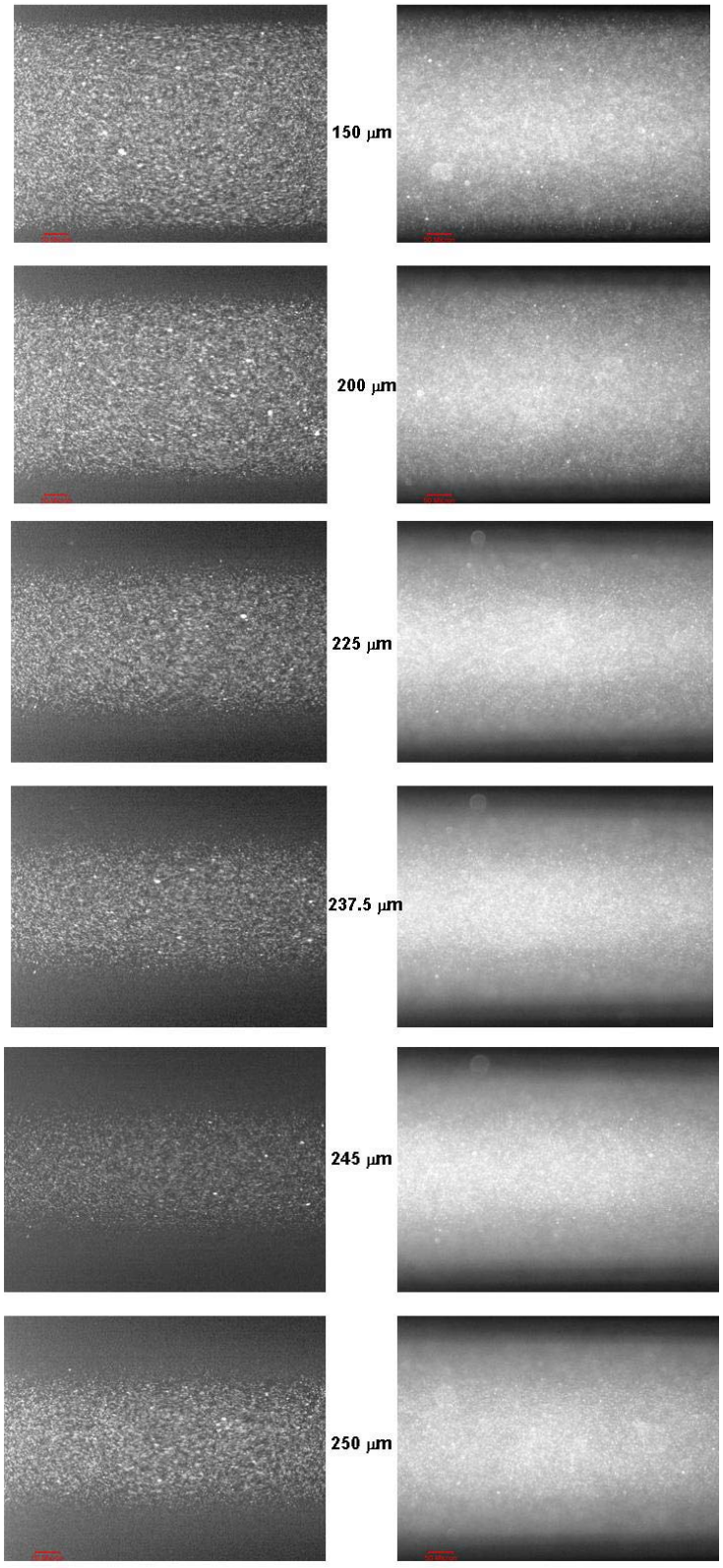
150 μm
200 μm
225 μm
237.5 μm
245 μm
250 μm

Summary of Experimental Parameters:

1. Pore diameter: 99-μm
2. Flow rate of syringe pump: 0.75-μl/hr (or 54.0-μm/s maximum velocity)
3. Number of image pairs: 29
4. Interrogation window: 32 x 32 pixels
5. Seeding particles: 200-nm fluorescent spheres at 0.01% in volume

Particle images of a 100 μm Circular Channel

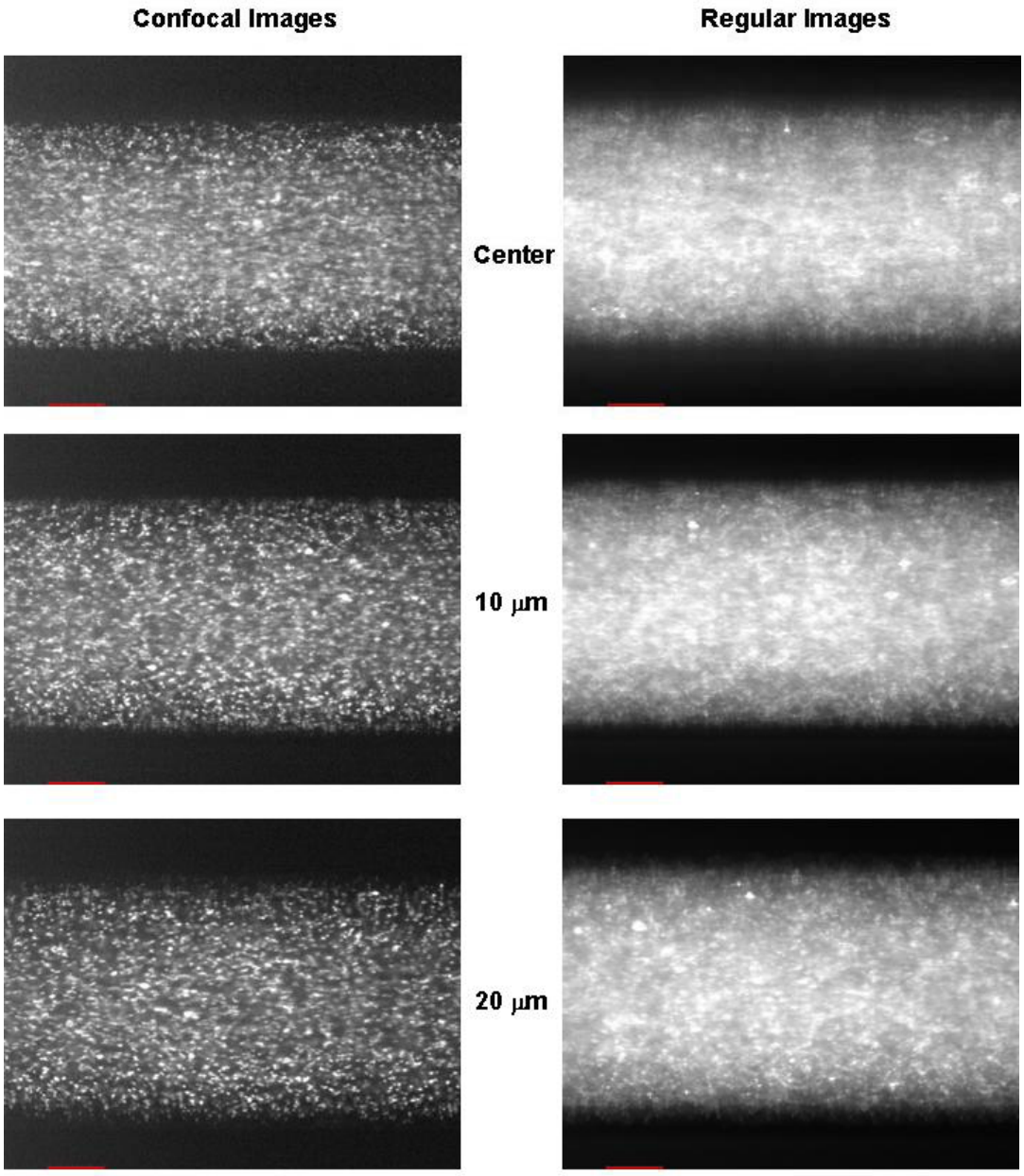

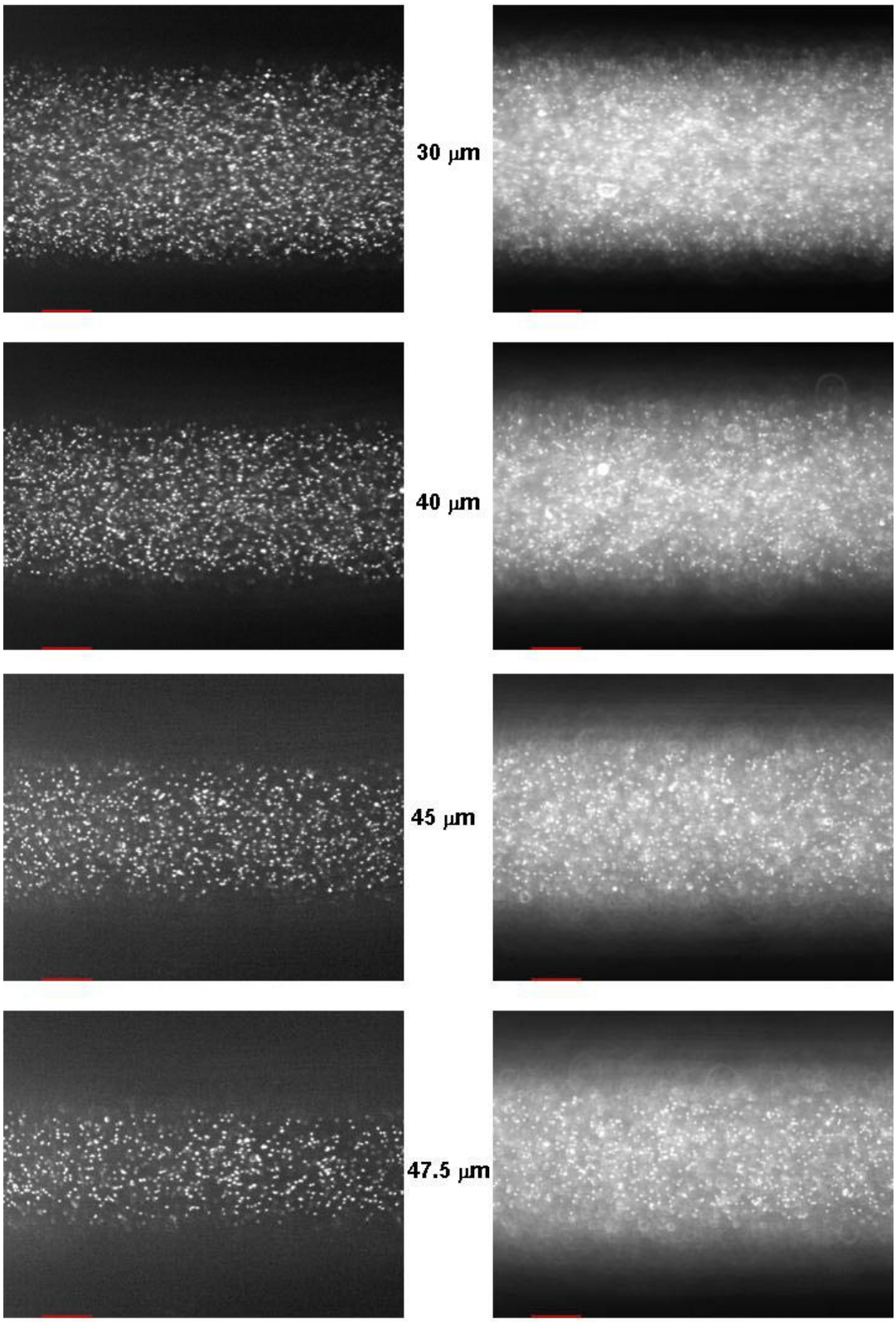
30 μm
40 μm
45 μm
47.5 μm

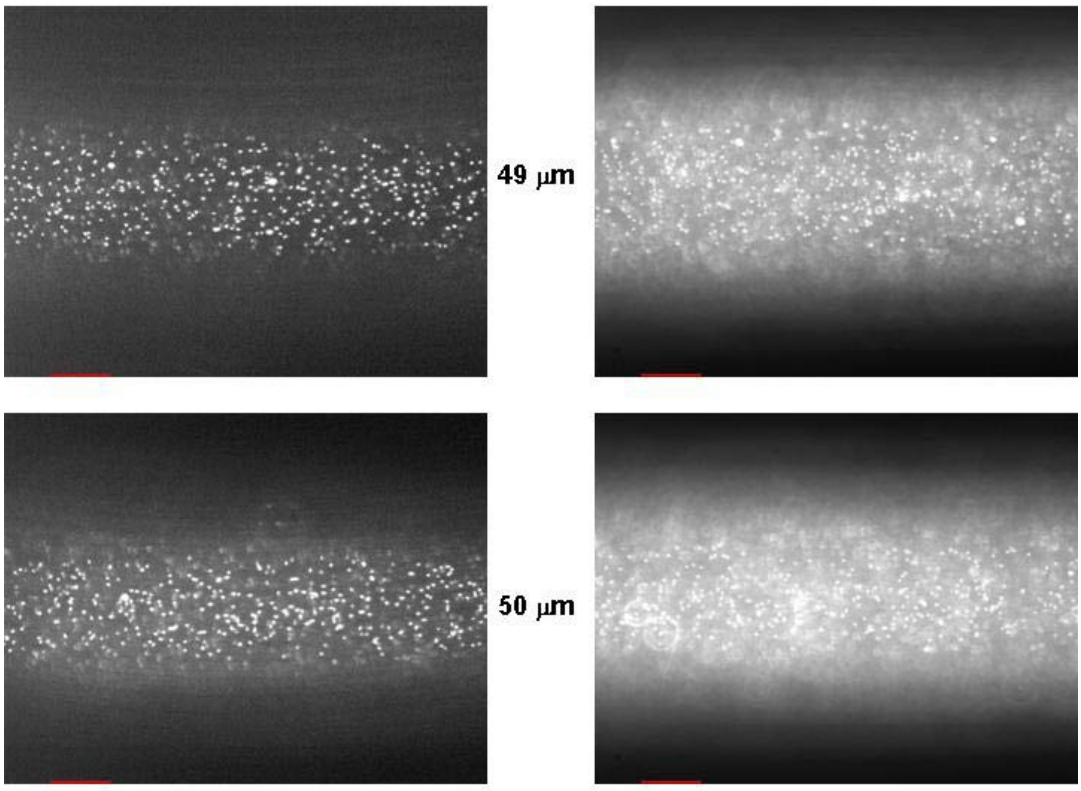

The PIV analysis has been done only for the center plane images and the results are shown for both capillary pores in Fig. 5. The error bars represent 95% standard deviations of the averaged data samples of all 29 PIV image pairs. A very good agreement is shown between the analytical solution for the Poiseuille flow (the parabolic curve line) and the measured velocity profiles using CLSM (the solid symbols), whereas the epi-fluorescent results show substantially underestimated velocity profiles (the regular symbols). The lowered flow measurements for the latter case are believed to be predominantly due to the thicker and loosely defined depth-of-field region, which inevitably biases the in-plane flow image with the forward- as well as the background out-of-focused particle images. In addition, the epi-fluorescent results, in contrast to the CLSM data, show larger deviations from the mean and this discrepancy is more pronounced for the larger 500-μm pore.

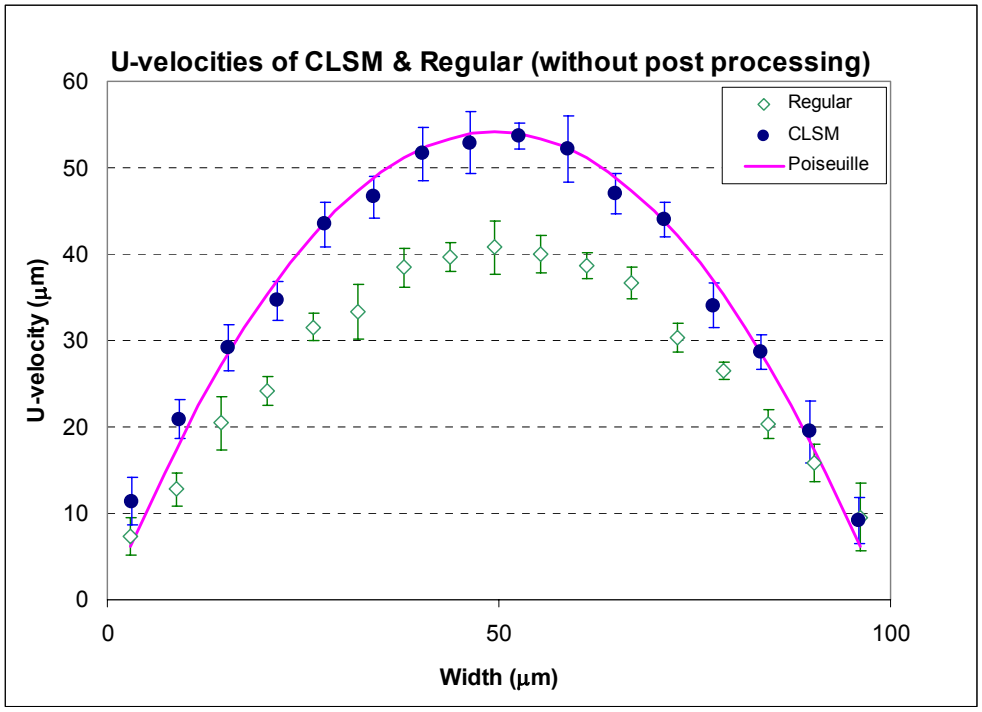

(a)

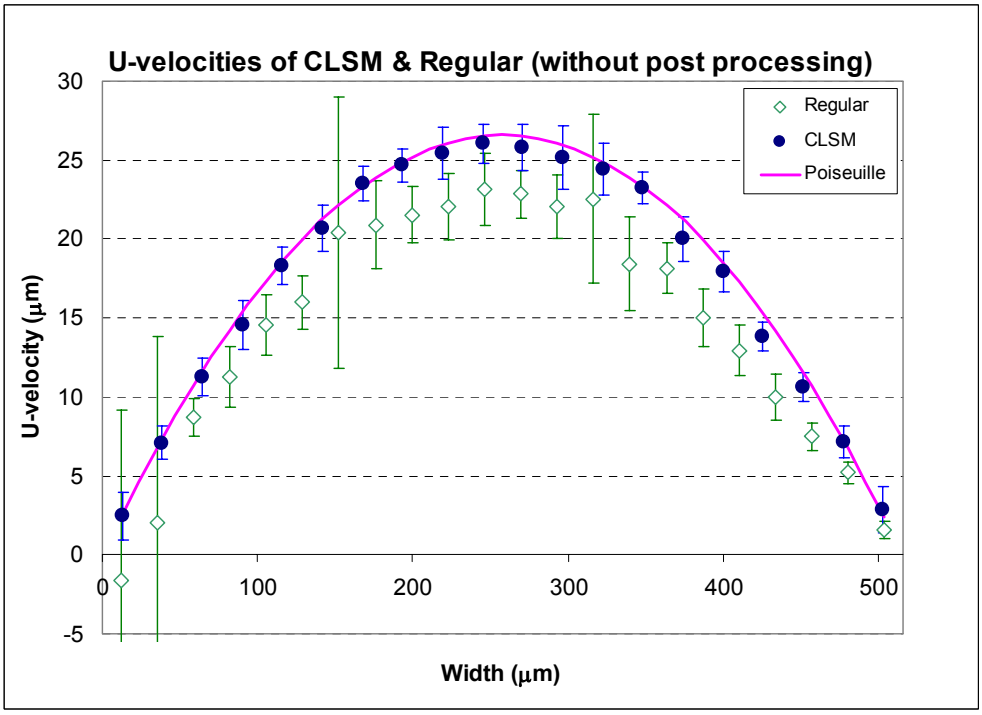

(b)

Figure 5. Comparison of the Velocity Profiles Measured by the CLSM-PIV and the Epi-Fluorescent PIV at the Pore Center Plane: (a) D = 99 μm and (b) D = 516 μm.

Rotating Micro-Couette Flow Under a Rotating Disk

The experimental setup (Fig. 6) consists of a 1.5-V DC motor set to rotate at a constant 17-rpm and the test fluid of deionized water seeded by 200-nm fluorescent microspheres at 0.002% in volume, with an excitation peak at 505-nm and an emission peak at 515-nm. The test section of micro-Couette flow is established between a rotating glass disk surface glued to the motor shaft end and the bottom of a small glass container, constituting a 180-μm clearance. A series of PIV measurements were performed at several different heights measured from the bottom surface using both the CLSM-PIV and the epi-fluorescent PIV techniques. All PIV images were taken at 30-fps and the images were processed by using the cross-correlation software developed by DAVIS of LaVision, Inc.

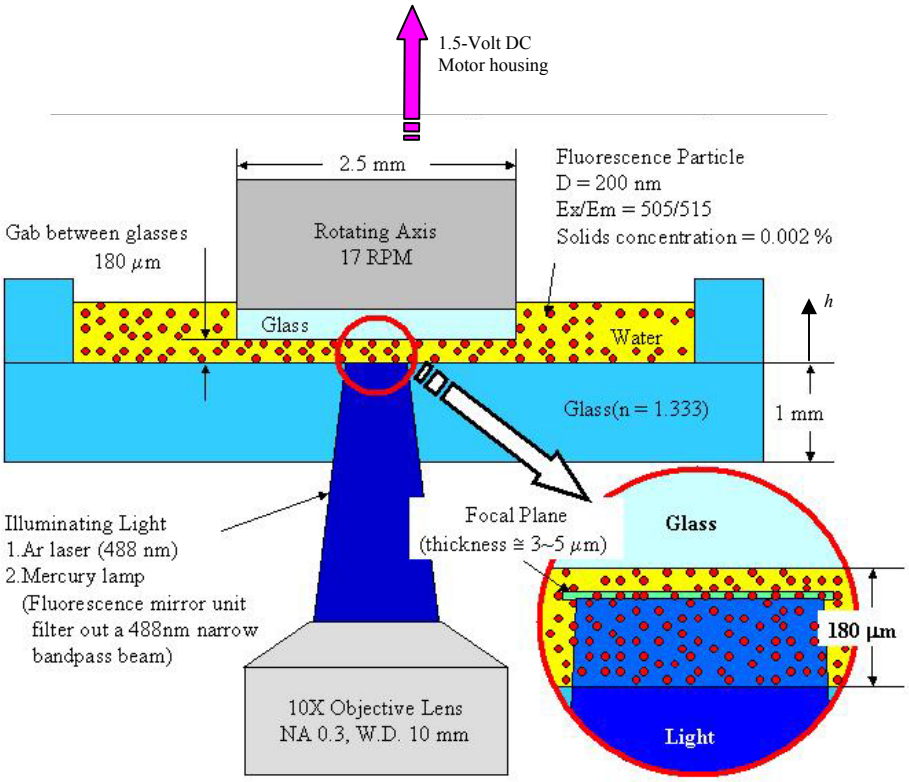

Figure 6. Test Section of a Rotating Micro Couette Flow Experiment

Figure 7 shows raw images (field-of-view: 661-μm x 661-μm) captured at different heights measured from the bottom, *h*. The images taken by the CLSM are clearly defined because of its distinctive depth-wise resolution while the images by the epi-fluorescent microscope are blurred by the foreground and background out-of-focus particle images that are expected to bias the velocity vector magnitudes, directions, and increase uncertainties. The CLSM, however, admits the CCD camera captures clear images by sharply filtering out-of-focus images.

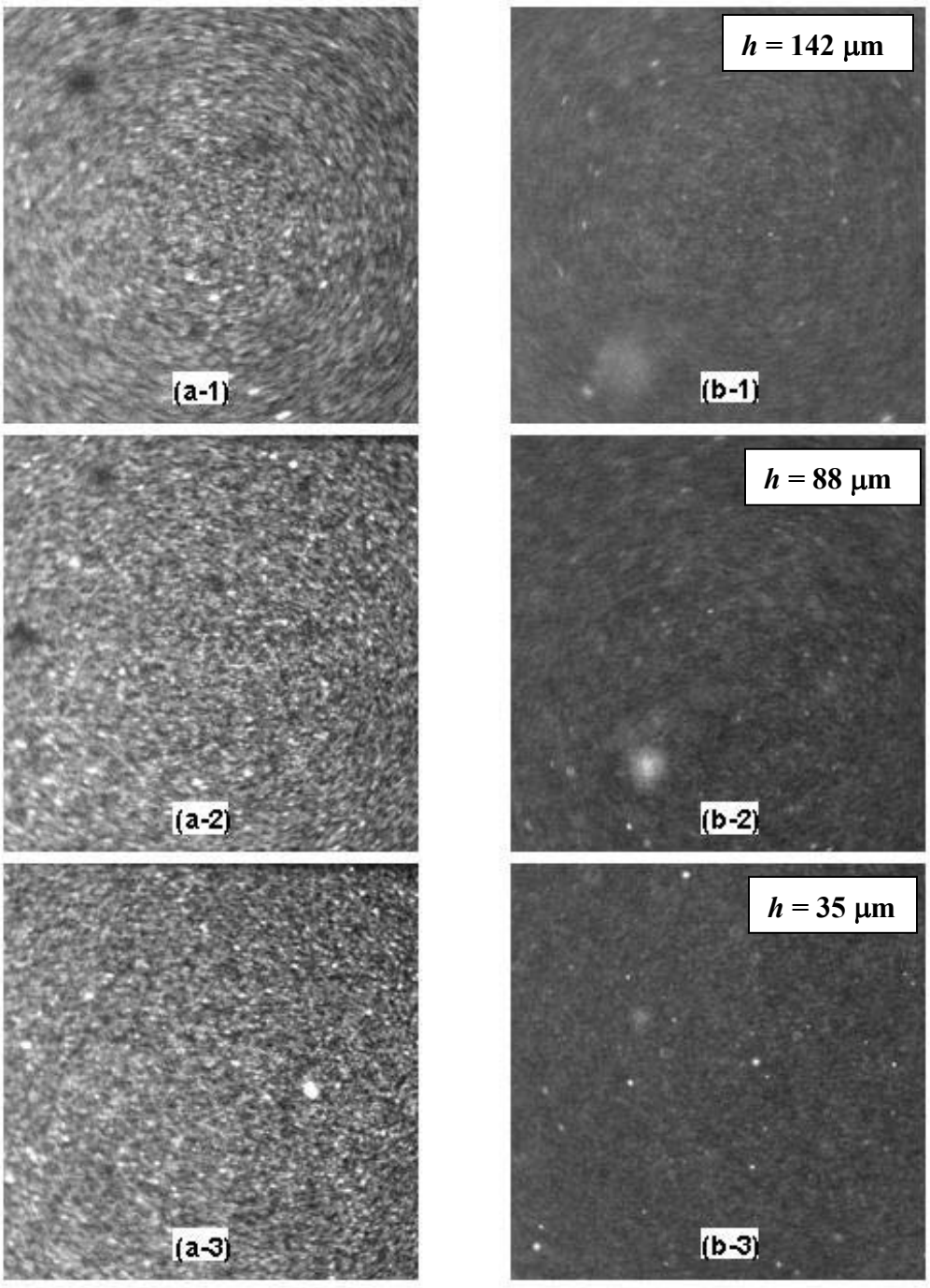

Figure 7. Raw Images Captured by the CLSM (a-1, 2 & 3), and by the Epi-Fluorescent Microscope (b-1, 2 & 3)

Figure 8 shows a comparison for the velocity vectors and streamline contours measured at different height locations (h) by both the CLSM and epi-fluorescent microscopes. The field-of-view size of all individual images is 413-μm by 413-μm. The CLSM results in the left column show relatively well-defined rotating Couette flow characteristics, i.e., concentric flows, while the epi-fluorescent results in the right column suffer excessive biasing and uncertainties, primarily because of its poor depth-wise resolution capability.

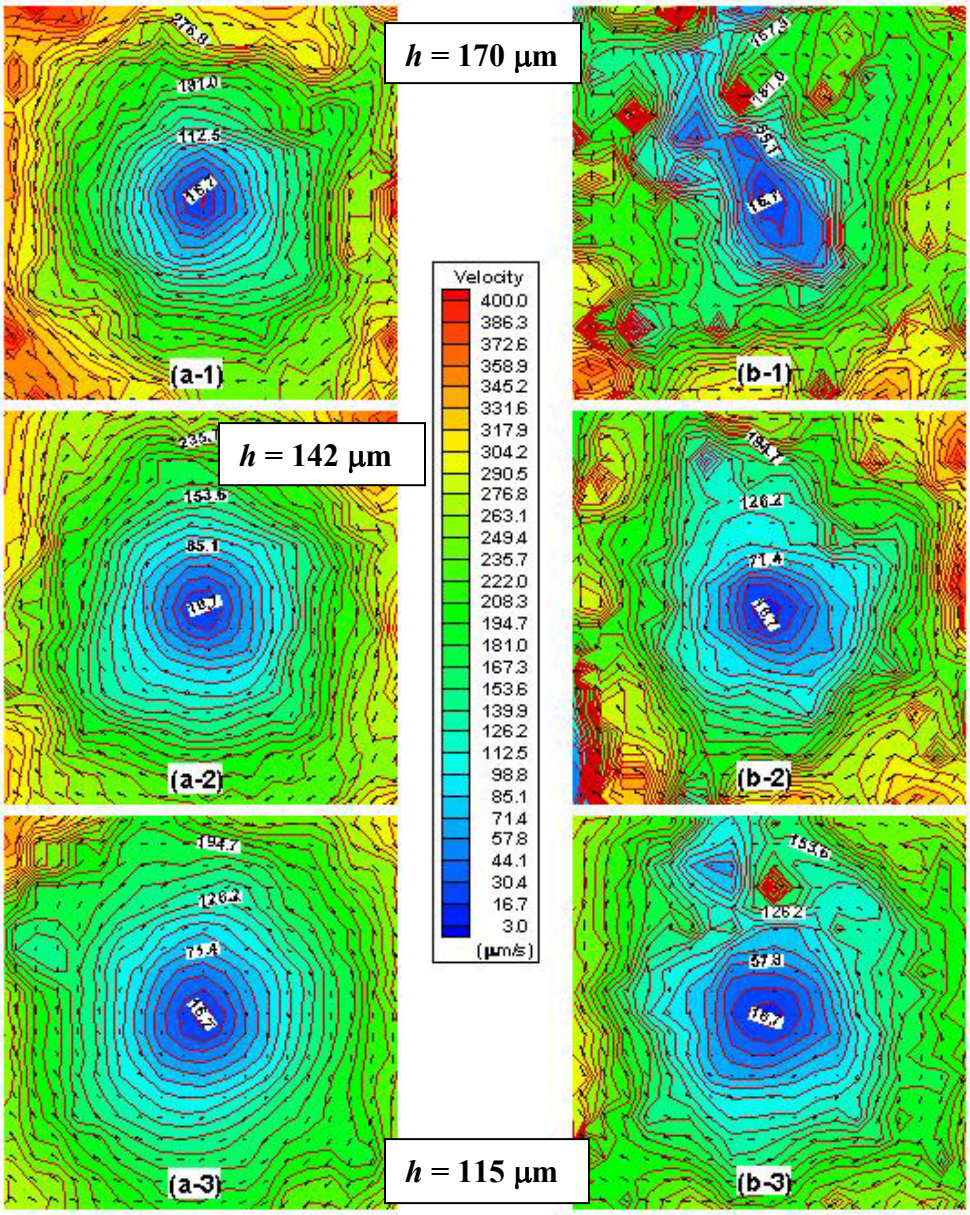

Figure 8. Velocity Vectors and Streamline Contours by the CLSM (a-1, 2 & 3) and by the Epi-Fluorescent Microscope (b-1, 2 & 3).

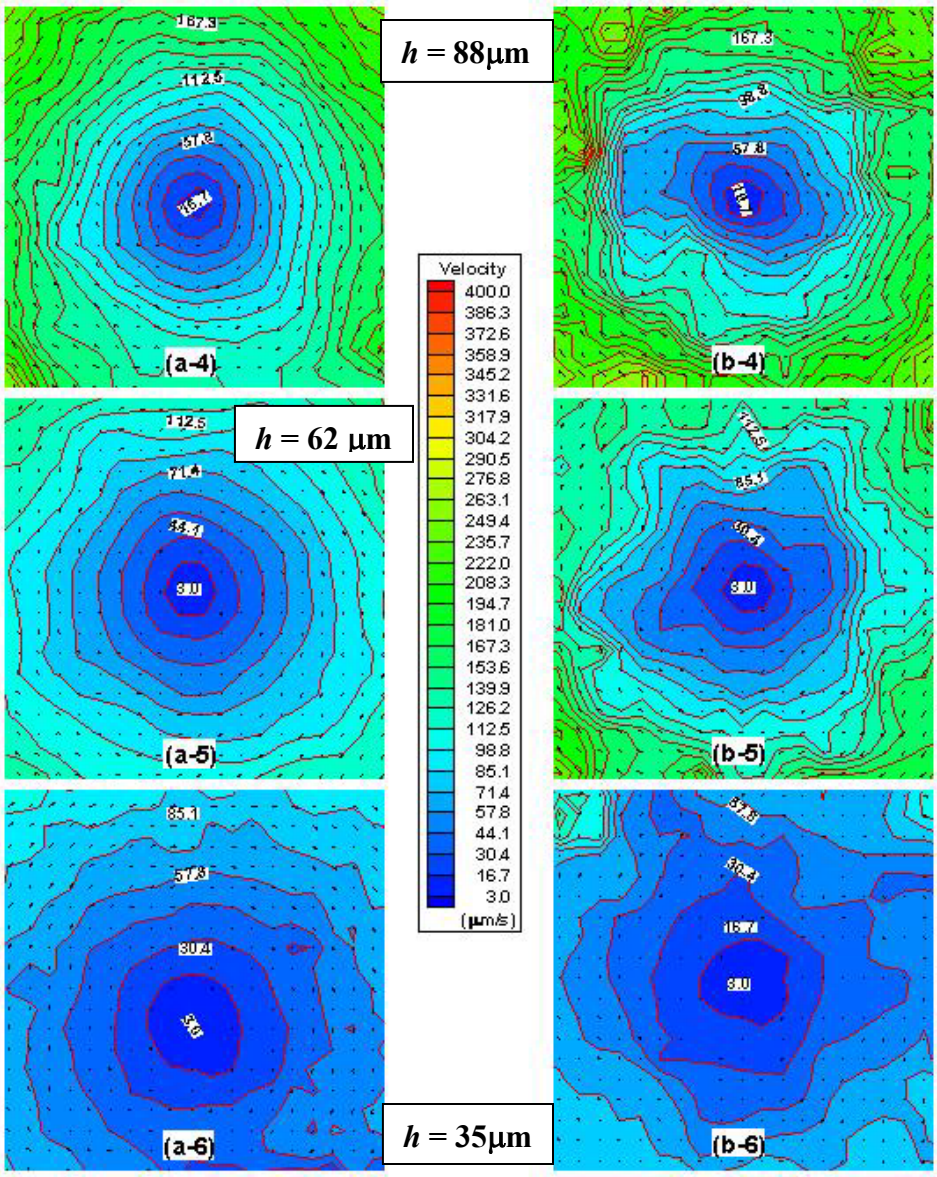

Figure 8. (Continued): Velocity Vectors and Streamline Contours by the CLSM (a-4, 5 & 6) and by the Epi-Fluorescent Microscope (b-4, 5 & 6).

Figure 9 shows azimuthally averaged rotational velocity magnitudes with their error bars representing the 95% standard deviations. Each plot, corresponding to a fixed radial location (r), shows the results measured at different heights, spanning from the stationary bottom (h = 0) to the rotating top (h = 180-μm). Thus, the Couette solutions predict a linear variation of the average flow speed from zero at h = 0 to r x ω (angular speed at h = 180-μm), as shown by the straight dashed lines. The average velocity magnitudes fairly well agree with the predictions for both the CLSM and the epi-fluorescent microscopic results, except the discrepancies shown near the rotating top-

surface. The discrepancy is more pronounced for the epi-fluorescence results, and this is believed to be attributed to its lower depth-wise resolution that tends to underestimate the flow vectors. More noticeably, the data fluctuations, measured by the standard deviation and shown by the error bars, are substantially larger for the epi-fluorescent microscopic results while they are significantly lower for the CLSM results. Again, we believe that this is mainly attributed to the depth-wise resolution in PIV imaging.

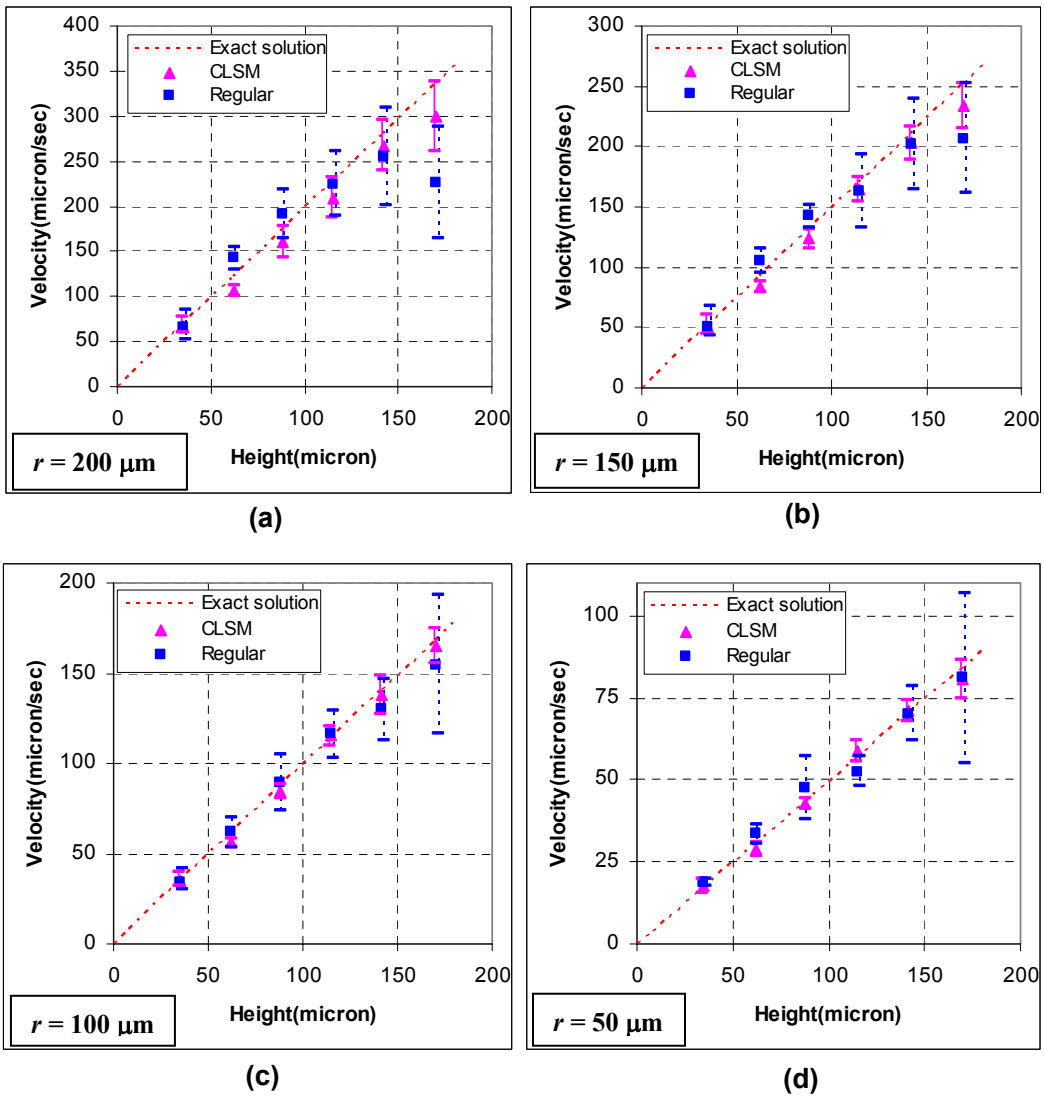

Figure 9. Comparison of Azimuthal Averages and 95% Deviations of the Rotational Velocity Magnitudes Measured Along the Height (*h*) at Different Radial Locations (*r*).